Integrated Zero-Index Metamaterials

Integrated Zero-Index Metamaterials

A thesis presented
by

Philip Camayd-Muñoz

to
The School of Engineering and Applied Sciences
in partial fulfillment of the requirements
for the degree of
Doctor of Philosophy
in the subject of

Applied Physics

Harvard University
Cambridge, Massachusetts
August 2016

Thesis advisor

Eric Mazur

Author

Philip Camayd-Muñoz

Integrated Zero-Index Metamaterials

Abstract

Nanotechnology has enabled the development of nanostructured composite materials (metamaterials) with exotic optical properties not found in nature. In the most extreme case, we can create materials that support light waves that propagate with infinite phase velocity, corresponding to a refractive index of zero. Zero-index phenomena can only be achieved by simultaneously controlling the electric and magnetic resonances of the nanostructure. We present an in-plane metamaterial design consisting of silicon pillar arrays, embedded within a polymer matrix. Using an integrated nano-scale prism constructed of the proposed material, we demonstrate a refractive index of zero in the optical regime. This design serves as a novel on-chip platform to explore the exotic physics of zero-index metamaterials, with applications to super-coupling, integrated quantum optics, and phase matching.

Contents

List of Figures

Citations to previously published work

Parts of this dissertation cover research reported in the following articles:

1. Y. Li*, S. Kita*, P. Muñoz, O. Reshef, D. I. Vulis, M. Lončar, and E. Mazur, "On-chip zero-index metamaterials," *Nature Photonics*, **9**, 738-742, 2015.

2. P. Muñoz, S. Kita, O. Mello, O. Reshef, D. I. Vulis, Y. Li, M. Lončar,and E. Mazur, "Lossless 2D Dirac-Cone Metamaterials," *Conference on Lasers and Electro-Optics, OSA Technical Digest* **JW2A.24**, San Jose, California, 2016.

3. S. Kita, Y. Li, P. Camayd-Muñoz, O. Reshef, D. I. Vulis, R. W. Day, E. Mazur, and M. Lončar, "On-chip all-dielectric fabrication-tolerant zero index metamaterials," *Submitted*.

Acknowledgments

First and foremost, I would like to thank my advisor Eric Mazur, for encouraging me to pursue new ideas even in familiar places. None of my achievement would have been possible without his trust and support, and for that I will always be grateful.

I've been fortunate to work with an incredible team, whose tireless efforts are reflected in the results presented here. Yang Li has been a driving force, providing both vision and theoretical insights. These designs are realized by Shota Kita's beautiful fabrication work, which is featured throughout this thesis. Daryl Vulis contributed to both the experimental and theoretical effort. Along with Olivia Mello, she represents the bright future of this work. Finally, I owe special recognition to Orad Reshef, who has been like a brother to me the past years. I've learned more from him than anyone else, and enjoyed every minute.

I would also like to thank the entire Mazur Group, which has been my home for the past seven years. I could not have asked for a more talented or welcoming environment. I am especially grateful to Paul Peng and Renee Sher, whose patient mentorship was invaluable in my first years, and who I've tried to emulate since.

In addition to my work on photonics, for the past few years I have participated in teaching AP50, Eric's project-based physics course. In particular, it has been my great pleasure to work with Kelly Miller. This experience has shaped my approach to physics education, and taught me surprising amount of fundamental optics.

Finally I would like to thank my parents, Alex and Nancy, and my wife, Cristina, for their patience, encouragement, and support through all my endeavors.

Acknowledgements of Financial Support

This thesis is based on work funded by the National Science Foundation under contracts ECCS-0901469, ECCS-1201976, PHY-1415236 and DMR-1360889, the Fonds de recherche du Québec – Nature et technologies, the Natural Sciences and Engineering Research Council

of Canada, the Harvard Quantum Optics Center, the Air Force Office of Scientific Research under contracts FA8721-05-C-0002, FA9550-12-1-0499 and FA9550-14-1- 0389, the Harvard Graduate Prize Fellowship, the Kavli Institute at Cornell for Nanoscale Science Postdoctoral Fellowship, the National Defense Science and Engineering Graduate Fellowship under contract 32 CFR 168a and the National Science Foundation Graduate Research Fellowship Program under contract DGE1144152. This work could not be accomplished without the use of the facilities in the Center for Nanoscale Systems, which was supported by the National Science Foundation's National Nanotechnology Infrastructure Network and which is now a member of the National Nanotechnology Coordinated Infrustructure Network (NNCI), which is supported by the National Science Foundation under NSF award no. 1541959. CNS is part of Harvard University.

To Cristina,

my amazing wife,

who will always be my greatest discovery

Chapter 1

Extreme Optics in Zero Index Media

1.1 Introduction

The electromagnetic wave equation (1.1) describes the full richness of optics—how light bounces and bends while propagating through space—yet the interaction of light and matter is parameterized by just two quantities: one is the electric permittivity ϵ, which describes the way that materials respond to electric fields. The other is its dual, the magnetic permeability μ, which describes the response to magnetic fields. Together these constitutive parameters describe phenomena ranging from refraction to plasmonics. Even the refractive index $n = \sqrt{\epsilon\mu}$, which measures the wave speed in a material, relies on the complex interplay of electric and magnetic effects.

$$\nabla^2 E - \frac{\mu\epsilon}{c^2}\frac{\partial^2 E}{\partial t^2} = 0 \tag{1.1}$$

In this sense, one can map the entire landscape of optical materials and phenomena along two dimensions, and perhaps uncover new physics in unexplored regions of this parameter space. Suppose the horizontal axis represents the electric response, measured by the

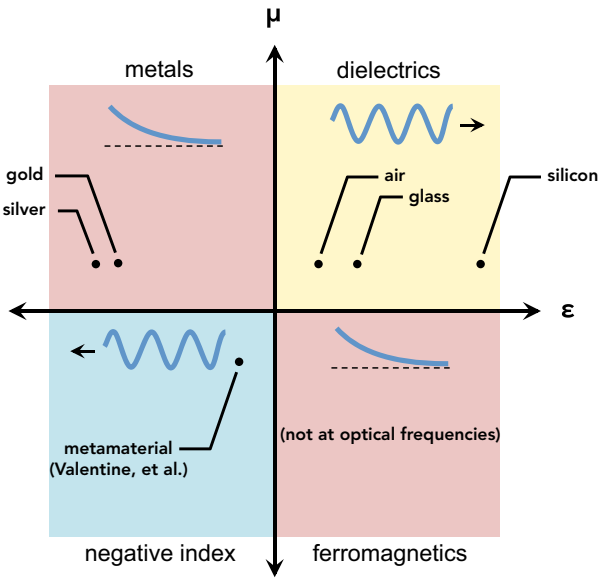

Figure 1.1: Optical materials can be categorized by the sign of the permittivity (ϵ) and permeability (μ). Each quadrant is associated with a different type of electromagnetic wave.

permittivity, while the vertical axis is the magnetic response, via the permeability (Figure 1.1). Most transparent materials lie within the first quadrant, supporting sinusoidal waves that propagate through space. The second quadrant contains materials with negative permittivity, and therefore an imaginary index of refraction. Physically, this corresponds to exponential decay of the electromagnetic fields within the material. Rather than propagating through these materials, light would be strongly absorbed and reflected. This behavior is common in metals, which make efficient mirrors but poor windows. The fourth quadrant shares these same properties, but is populated by ferromagnetic materials. Finally, the third quadrant contains materials with both negative permittivity and permeability. This corresponds to a negative real index of refraction, so these materials once again support propagating waves; however, these waves propagate with negative phase velocity[1]. In prin-

[1]This phenomenon does not occur in natural materials, but advances in nanotechnology have enabled the design and fabrication of artificial materials with negative phase advance and negative refraction [1,2].

ciple, any material can be categorized into one of these four quadrants, each with its own distinct propagation characteristics. Given these sharp differences, what behavior should we expect from materials that lie along the axes, on the boundary between the quadrants?

The materials in this regime have a refractive index near zero, which leads to unusual properties that are distinct from either of the neighboring quadrants. For example, the wavelength of propagating light is determined by the refractive index: when light enters a material with a high index of refraction, the wavelength shrinks. Conversely, the wavelength is elongated when passing into a lower index. In the limit where the refractive index approaches zero, the wavelength becomes infinitely long (Figure 1.2). Within such a material, the electric and magnetic fields are uniform. Although they continue to oscillate in time, they do so in unison throughout the crystal. This same behavior arises in plasmonic materials (quadrant II), even though the underlying physics is characteristically different. In plasmonic media, the waves decay exponentially with distance after entering the material. Wavelength is no longer a meaningful descriptor of the fields, but the characteristic decay length of the evanescent wave is proportional to the refractive index. As the index approaches zero the evanescent tail extends further, ultimately extending to infinity. Once again, a zero-index material is characterized by uniform fields throughout the material.

The origin of this unusual behavior is a structural change in the underlying physics. Optical materials are generally governed by a wave equation, which relates temporal and spatial gradients of the electric and magnetic fields by a proportionality constant equal to the refractive index. When the index approaches zero, the spatial and temporal behavior become decoupled. The spatial field distribution is no longer described by a wave equation, but by Laplace's equation, $\nabla^2 E = 0$. This is the physics that governs electrostatics, but crucially, it becomes accessible at optical frequencies. The result is a material that behaves like an electronic conductor, but which channels light instead of current.

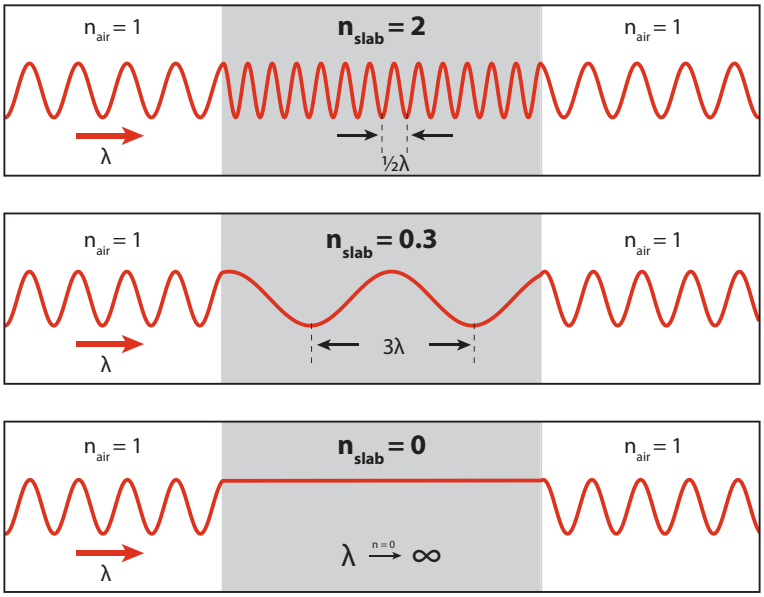

Figure 1.2: As light propagates through dielectric media the wavelength grows or shrinks in proportion to the refractive index.

1.2 Propagation in Zero-Index Media

Somewhat counter-intuitively, there are naturally occurring materials with an index of zero: metals. The permittivity of metals depends strongly on the frequency of light, taking on negative values at visible frequencies and approaching zero in the ultraviolet regime. At the plasma frequency, where the permittivity reaches zero, the index of refraction is equal to zero. However, the metal surface reflects all incident light, rendering the zero-index phenomena inaccessible. Applications in optical devices require a material with zero index that also allows efficient power transfer from free space.

Coupling efficiency into a material is determined by the impedance mismatch across the interface [3]. The reflection vanishes if the impedance is the same for both materials, and it gets worse as the mismatch grows. In general, the impedance $\eta = \sqrt{\frac{\mu}{\epsilon}}$ depends on the ratio of the permittivity and permeability. As metals have an imaginary impedance,

the match with the surrounding air will be poor, resulting in strong reflection. Even at the plasma frequency, where $\epsilon = 0$, the impedance becomes enormous and the reflectivity of the surface approaches 100%. This problem is inherent to any zero-index material where either the permittivity or permeability approaches zero. By contrast, there is no such singularity when the permittivity and permeability approach zero simultaneously, $\epsilon = \mu = 0$. In this case, the impedance maintains a finite value regardless of how small the refractive index becomes, resulting in efficient power transmission across the interface even with a refractive index of zero.

Impedance matched zero-index media can efficiently couple to propagating waves in free space, allowing direct access to "electrostatic" fields at optical frequencies. For example, light propagates as an electromagnetic wave with a finite wavelength, represented by a series of crests/troughs. When this wave reaches the boundary of a zero-index slab, the electric and magnetic fields within the slab oscillate in time with the incident wave, and energy is communicated to the slab mode due to the matched impedance. The wavelength is effectively infinite within the zero-index region, resulting in uniform fields across the entire domain. Therefore, the continuity of the fields at each boundary will communicate the incident wave through the slab instantaneously[2], recreating it at the far end of the slab.

We can expand this analysis to include refraction through arbitrarily shaped regions of zero refractive index. More generally the fields within this region are governed by a modified form of Maxwell's equations, as well as the electromagnetic boundary conditions. In particular, when $\epsilon = \mu = 0$:

[2]This should not be confused with superluminal communication, which would require zero-index propagation across a broad range of frequencies [4]. Instead, infinite phase velocity is more closely associated with coordinated oscillation of fields across the slab.

$$\vec{\mathbf{D}} = \epsilon\vec{\mathbf{E}} = 0 \tag{1.2}$$

$$\vec{\mathbf{B}} = \mu\vec{\mathbf{H}} = 0 \tag{1.3}$$

$$\nabla \times \vec{\mathbf{E}} = -\frac{\partial\vec{\mathbf{B}}}{\partial t} = 0 \tag{1.4}$$

$$\nabla \times \vec{\mathbf{H}} = \vec{\mathbf{J}}_f + \frac{\partial\vec{\mathbf{B}}}{\partial t} = 0 \tag{1.5}$$

$$\tag{1.6}$$

Therefore, both the electric and magnetic fields are irrotational. For propagation in the plane, field solutions can be categorized as TE or TM, depending on the out-of-plane field component. Without loss of generality[3], we will restrict the discussion to TM (i.e. the electric field is polarized out of the plane, E_z). In this case, the condition $\nabla \times E = 0$ implies that the electric field is constant throughout the zero-index region. By contrast, the magnetic field consists of two in-plane components $\vec{\mathbf{H}} = H_x\mathbf{i} + H_y\mathbf{j}$, which may vary spatially. Finally, the fields must be continuous across the boundary with free space. In the absence of free charges and currents,

$$\hat{\mathbf{n}}_{12} \times (\vec{\mathbf{E}}_1 - \vec{\mathbf{E}}_2) = 0$$

$$\hat{\mathbf{n}}_{12} \cdot (\vec{\mathbf{D}}_1 - \vec{\mathbf{D}}_2) = 0$$

$$\hat{\mathbf{n}}_{12} \times (\vec{\mathbf{H}}_1 - \vec{\mathbf{H}}_2) = 0$$

$$\hat{\mathbf{n}}_{12} \cdot (\vec{\mathbf{B}}_1 - \vec{\mathbf{B}}_2) = 0$$

where $\hat{\mathbf{n}}_{12}$ represents the normal vector at the interface between the zero-index medium and free space, and the field subscript denotes the fields on either side of the boundary. In free

[3]TE solutions can be recovered by interchanging the electric and magnetic fields.

space $\vec{\mathbf{D}} = \vec{\mathbf{E}}$ and $\vec{\mathbf{B}} = \vec{\mathbf{H}}$, so these continuity conditions require all fields in free space to be tangential and continuous across the interface regardless of the shape of the boundary or the orientation of the incident wave. Furthermore, both the electric and tangential magnetic fields are uniform along the boundary, resulting in plane-wave scattering from the interface.

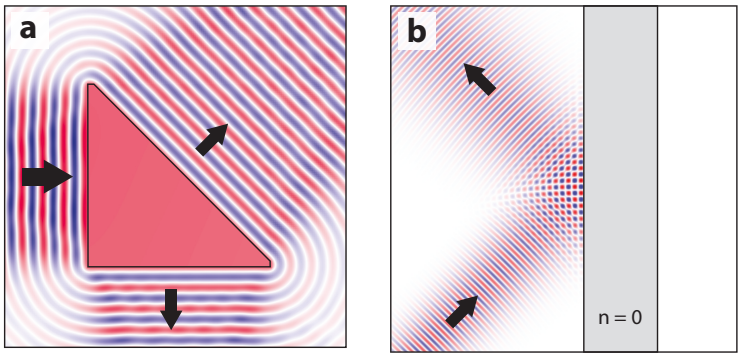

Figure 1.3: Refraction and total internal reflection in zero-index media. a) Normally incident light couples to a zero-index triangular prism. The electric field is uniform throughout the prism, which produces a refracted beam perpendicular to all of the edges. b) Light incident at an oblique angle is unable to couple to a zero-index slab due to total internal reflection.

We can observe this unusual refraction in the case of a triangular zero-index prism, which is illuminated from one side (Figure 1.3a). The incident wave couples to the prism without reflection, whereupon the electric fields uniformly fill the space. The magnetic fields are non-uniform within the prism, but the tangential component is constant along the boundary. As a result, the zero-index prism creates a refracted beam perpendicular to the interface as required by Snel's law:

$$\theta_{\text{out}} = \sin^{-1}\left(\frac{n_{\text{in}}}{n_{\text{out}}}\sin(\theta_{\text{in}})\right) = 0$$

The continuity conditions require that any refraction through a zero index medium emerges as a beam directed normal to the surface. By extension, *every* surface produces such

a beam. By a similar argument, we can show that any waves arriving at the boundary of a zero-index medium will be perfectly reflected unless they propagate normal to the interface (Figure 1.3b). The total tangential electric and magnetic fields at the boundary must be uniform, including both the incident and reflected waves. For a plane wave incident at some angle relative to the surface normal, this condition can only be satisfied if the reflected and incident waves have equal amplitude. This effect can also be described as total internal reflection (TIR) at the boundary of a zero index material. In this limit, the critical angle $\theta_t extrmcrit = \sin^{-1}(\frac{n_1}{n_2}) = 0$, so only waves at normal incidence are allowed to propagate through the interface. While TIR is typically employed for waveguiding in high-index media (e.g., optical fibers), it also provides confinement for light in free space with a zero-index "cladding".

1.3 Coordinate Transformation of Zero-Index Regions

Viewed from the perspective of Maxwell's equations, the extreme optical properties of zero-index media give rise to a constellation of unusual refractive effects. However, this description provides little intuition for fields that originate within the zero-index region. Alternatively, we can use coordinate transformations to describe zero-index phenomena geometrically, providing new insights and an intuitive model.

The key observation is that the form of Maxwell's equations is invariant under arbitrary coordinate transformations [5, 6]. The only effect of such a transformation is to change the effective material properties within the transformed space. For example, the distortion of waves traveling through the curved space around a black hole can be recreated by an inhomogeneous distribution of refractive index [7]. This equivalence between curvature and refractive index has been applied extensively to demonstrate effects such as invisibility

cloaking [8, 9], sub-wavelength imaging [10, 11], and energy collection [12], all of which can be described by some equivalent coordinate transformation. Conversely, we can describe a known distribution of refractive indices as a coordinate transformation in order to understand its effects on electromagnetic fields. For example consider a slab of low index material surrounded by air, which is illuminated by a plane wave (Figure 1.4). As light propagates through the slab, phase accumulates at a rate proportional to the refractive index. By framing the inhomogeneous index profile as a coordinate transformation [13], we can describe the same system as a region of stretched space with a homogeneous index $n = 1$. The "stretching ratio" is equal to the refractive index of the slab. Uncompressing the space provides intuition about wave propagation through this region, accounting for the phase accumulation geometrically. This same mechanism describes refractive effects in zero-index media. As the index of the slab approaches zero, the equivalent coordinate transformation is stretched to infinity. Equivalently, the edges of the slab become arbitrarily close together in the un-stretched space. Waves propagating through such a material will travel across an infinitesimal effective distance with apparently infinite speed.

This argument can also be extended to finite regions of zero index in order to understand the behavior of embedded emitters. Consider a sphere filled with an impedance matched zero-index medium. Using transformation optics, we seek to define an equivalent space filled with a homogeneous index $n = 1$ and stretched coordinates. In a system of spherical coordinates, transformations involving only the radial coordinate correspond to a spatially-dependent permittivity and permeability [14]:

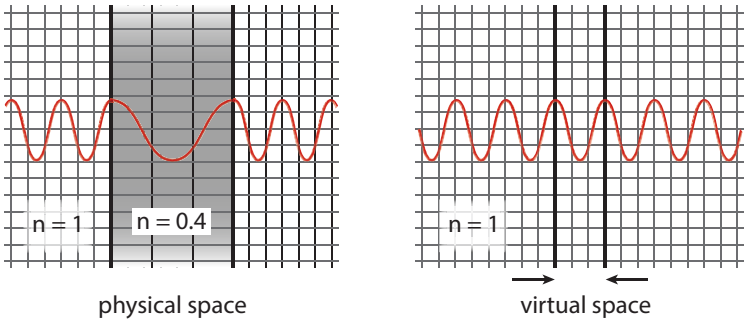

Figure 1.4: Refractive index as a coordinate transformation. As a wave propagates through a slab of low-index media, phase accumulates more slowly (i.e. the wavelength is longer). Equivalently, we may treat this as an effective coordinate transformation, indicated by the stretched grid in the low-index region. In a virtual space with an undistorted grid, the effective index is uniform everywhere ($n = 1$), but the boundaries of the slab move closer together.

$$\epsilon_r = \mu_r = \frac{r^2}{R^2}\frac{dR}{dr}$$
$$\epsilon_\theta = \mu_\theta = \frac{dr}{dR}$$
$$\epsilon_\phi = \mu_\phi = \frac{dr}{dR}$$

where R is the transformed radial coordinate and r is the original radial coordinate. These effective optical properties are generally inhomogeneous and anisotropic. However, the effective index is isotropic and uniform in the case of scaling transformations $R(r) = \alpha r$. This equivalence can be understood as an expression of scale invariance in Maxwell's equations. In order to remove the index discontinuity at the boundary of the sphere, the transformation must also include a discontinuity. Such finite embedded coordinate transformations have been shown to be reflectionless if the impedance is matched across the interface [15, 16]. We can therefore describe the zero-index sphere using a discontinuous scaling transformation:

$$R(r < b) = nr$$
$$R(r \geq b) = r \tag{1.7}$$

This transformation effectively shrinks the spherical region by a factor equal to the original index. The result is a space that is filled with a uniform index $n = 1$, but which is discontinuous across the boundary of the scaled sphere. Finally, we can connect the edges[4] of the two domains to produce a coordinate system similar to the one-dimensional case shown in Figure 1.4.

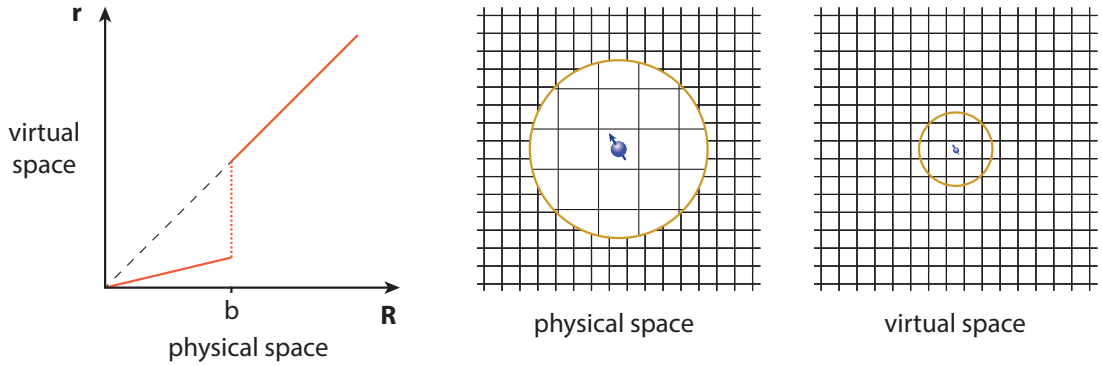

Figure 1.5: A spherical region of low refractive index is equivalent to a radial coordinate transformation (eq. 1.7). Within the low-index region ($R < b$) the transformed radial coordinate r is scaled by a factor equal to the index. Therefore, a point source in the virtual space appears magnified in physical space.

This scaled domain offers insight into the behavior of emitters placed within a zero-index region. Figure 1.6 shows the electric and magnetic fields radiating from a dipole at the center of a circular region with $n = 0.01$. Although the circle spans 16 free-space wavelengths, the electric field is uniform across the region. Meanwhile the magnetic field components decay radially, appearing as crossed dipoles. In the context of the stretched coordinates, we recognize these radiation patterns as the near-fields of the point source. In

[4]Generally the connection between these two domains is subject to shearing, as the scaling transformation affects radial but not tangential components. However, this operation simplifies to simple scaling in the case of radially symmetric fields. An equivalent continuous transformation is demonstrated in Appendix B.

particular, we recover the exact behavior of the embedded emitter by scaling the radiation pattern of an equivalent point source in free space by a factor $1/n$. The zero-index region effectively extends the near field to macroscopic space. Equivalently, any emitter placed within a zero-index region radiates as though it is positioned within an infinitesimal region of space. Therefore, we expect the radiation pattern outside of the circle to be insensitive to the position of the emitter in physical space—all physical positions are mapped to the same point in the distorted space. Figure 1.7a shows the fields generated by a dipole positioned near the edge of the zero-index region, which produces an isotropic radiation pattern identical to the centered dipole in Figure 1.6. In addition, multiple emitters within the zero-index region are effectively positioned within the near field of each other. Therefore, dipoles emitting in phase will interfere constructively regardless of their position or number (Figure 1.7d), while out-of-phase contributions will cancel exactly (Figure 1.7d). These long-range coherence effects in zero-index media may find applications in sensing and quantum optics [17, 18]. Finally, the mapping of the near field to macroscopic scales is independent of the shape of the zero-index domain, as all boundaries are mapped to an infinitesimal region. This effectively reshapes the radiation pattern, dependent only on the shape of the zero-index region [19]. For example, an isotropic dipole can inherit the angular selectivity of zero-index refraction when placed within a rectangular domain (Figure 1.7c).

1.4 Causality in Zero-Index Media

Thus far, the effects of zero refractive index have been described in terms of the spatial extent of waves: either the wavelength is infinitely long, or equivalently the waves travel through an infinitely distorted space. We may alternatively describe these same effects in terms of the waves' velocity. A wavefront propagating through a zero-index slab reaches the far side

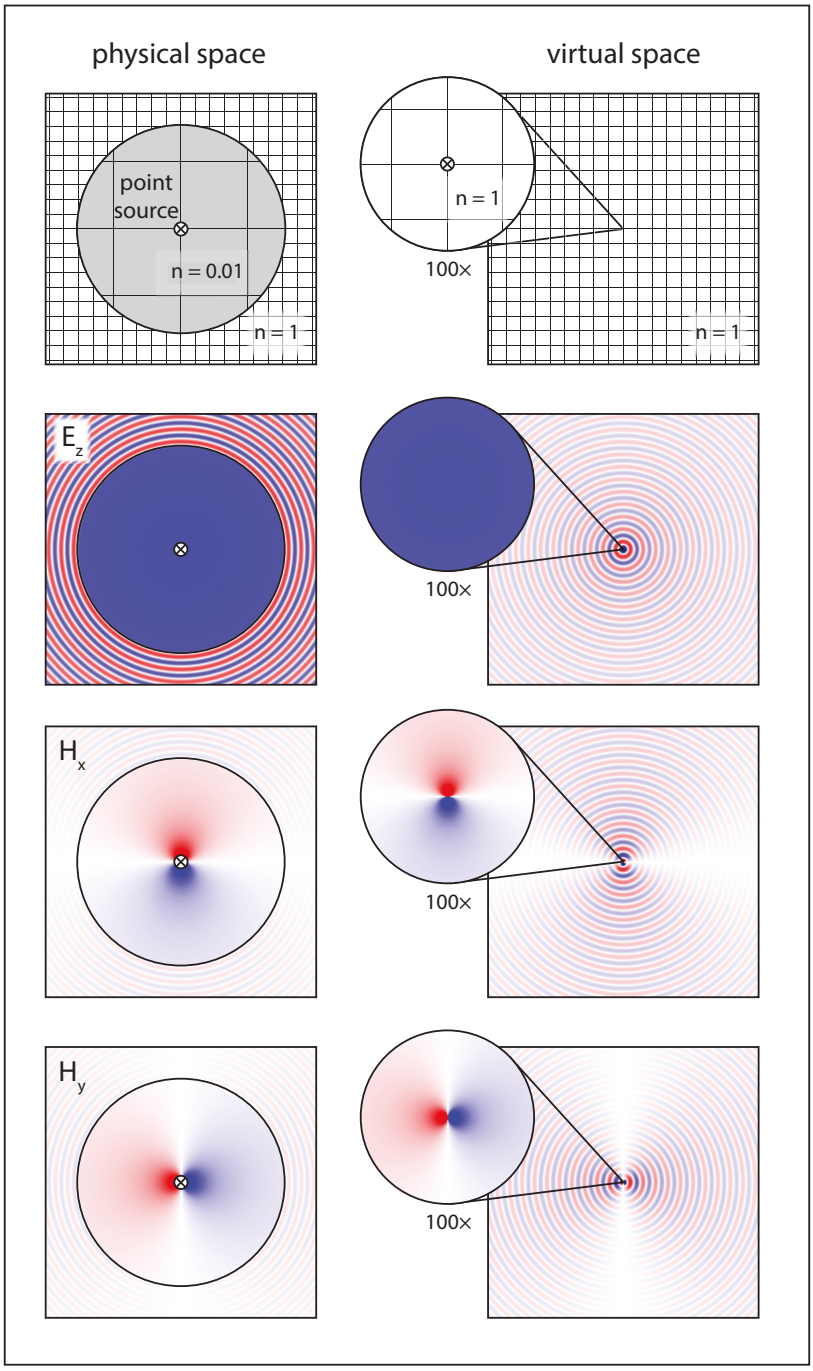

Figure 1.6: Radiation from point-like emitters in zero-index media. We simulate the fields of an out-of-plane line source at the center of a circular region with near-zero index, $n = 0.01$. This is equivalent to a distorted virtual space, where the boundary is shrunk by $100\times$ and the index is uniform everywhere, $n = 1$. The right-hand side shows the fields in physical space, while the left-hand side shows the fields of an equivalent source in a uniform space where $n = 1$. The inset shows the fields in the vicinity of the source in the virtual space.

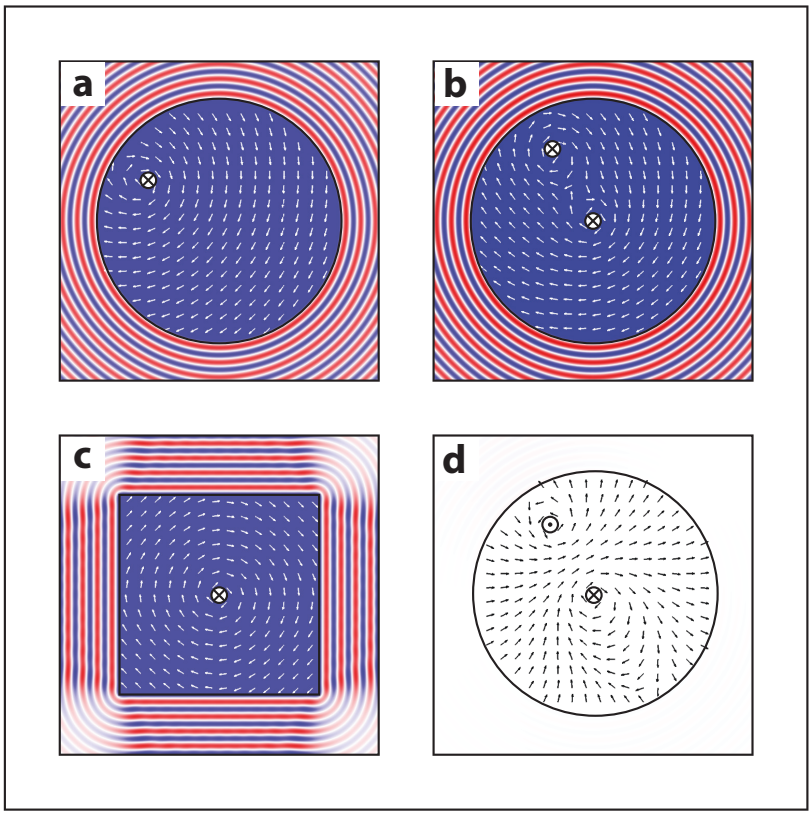

Figure 1.7: Radiation from different configurations of point-like emitters. a) Field distribution from an off-center point source. b) Fields due to two point sources, radiating in phase. c) Fields from a square region of zero-index media, showing a transformed radiation pattern normal to the faces. d) Fields due to two point sources radiating out-of-phase. The fields add destructively, producing no far field radiation. The color indicates the out-of-plane electric field distribution, and the arrows indicate the direction of the in-plane magnetic field.

instantaneously due to the continuity conditions laid out above. This phase velocity, which is inversely proportional to the refractive index, is superluminal for any index less than that of vacuum. In particular, it approaches infinity within zero-index media.

At first, this phenomenon may seem to allow superluminal communication between distant observers using zero-index conduits, in violation of the principle of causality. However, these examples of "instantaneous" transport are restricted to harmonic solutions to the wave equation, which cannot be used to transmit information [3]. Any information transfer, for example using an optical pulse, necessarily involves the superposition of multiple frequencies[5] such that instantaneous communication would require zero-index behavior across a finite bandwidth. In addition, the imaginary index (corresponding to energy dissipation) must also be dispersionless [4]. Superluminal pulse propagation has been demonstrated in bandgap materials where the refractive index is equal to zero across a broad bandwidth [20, 21], but this effect can be attributed to a distortion of the pulse by frequency-dependent absorption. These two conditions lead to an important restriction to zero-index phenomena, specifically with regards to dispersion. Unlike positive index media, there can be no materials with zero refractive index for a continuous range of frequencies, except those with highly dispersive absorption. The refractive index is connected to absorption through Kramers-Kronig relations, which apply to any complex analytic function in the frequency domain. For the complex refractive index $n = n + in''$,

$$\mathrm{Re}[n^2(\omega)] = 1 + \frac{2}{\pi}\int_0^\infty \frac{\mathrm{Im}[n^2(\omega')]\omega'}{\omega'^2 - \omega^2} d\omega$$

If the real refractive index is equal to zero for some finite continuous range of frequencies, then the imaginary part must be strongly dispersive (Appendix C). Similarly,

[5]The range of frequencies can be determined using a Fourier transform. A perfectly harmonic solution involves only one frequency component, but also carries no information. All other solutions have a finite width in the frequency domain.

low-loss zero-index propagation is only possible in materials with linear dispersion. This restriction applies to any causal material with zero refractive index, regardless of the specific constituent materials, limiting signal propagation to sub-luminal velocities. To observe this effect, we can use a magnetic-electric Lorentz model to represent a material with a refractive index equal to zero at a single frequency (Figure 1.8a). This is a causal model, satisfying Kramers-Kronig relations for the complex permittivity and permeability. The constituent properties emulate an electric and magnetic dipole resonance. For simplicity, we will assume that both oscillators have equal strength and low dissipation, such that the permittivity and permeability are given by

$$\epsilon = \mu = 1 + \frac{\omega_0^2}{\omega_0^2 - \omega^2 - 2i\delta\omega}$$

where the resonant frequency $\omega_0 = 8.6\times10^{14}$, and the resonance linewidth $\delta = 10^{13}$ Hz. Here, both oscillators are assigned the same parameters, resulting in a uniform impedance $Z = 1$ for all frequencies. Above the resonance frequency, the real permittivity and permeability fall below zero, crossing the axis again at an effective wavelength of 1550 nm. The imaginary index peaks in the vicinity of the resonant frequency, and maintains a small positive value near the zero-index wavelength. Using this model, we simulate a short optical pulse in the time-domain as it propagates through a slab with zero index (Figure 1.8b). The pulse has a central wavelength of 1550 nm, with bandwidth of 100 nm on either side. Although the index is only equal to zero at the center frequency, the value stays below unity for all frequencies that make up the pulse. Any one of these frequency components would therefore exhibit superluminal phase velocity. However, the pulse envelope propagates at the group velocity in the medium, which accounts for the effects of dispersion: $\nu_g = (n/c - \lambda dn/d\lambda)^{-1} \approx 1/4c$. The simulation shows the pulse propagating through free space at the speed of light before entering the slab. Once inside, the pulse is slowed to one quarter of its original speed. It

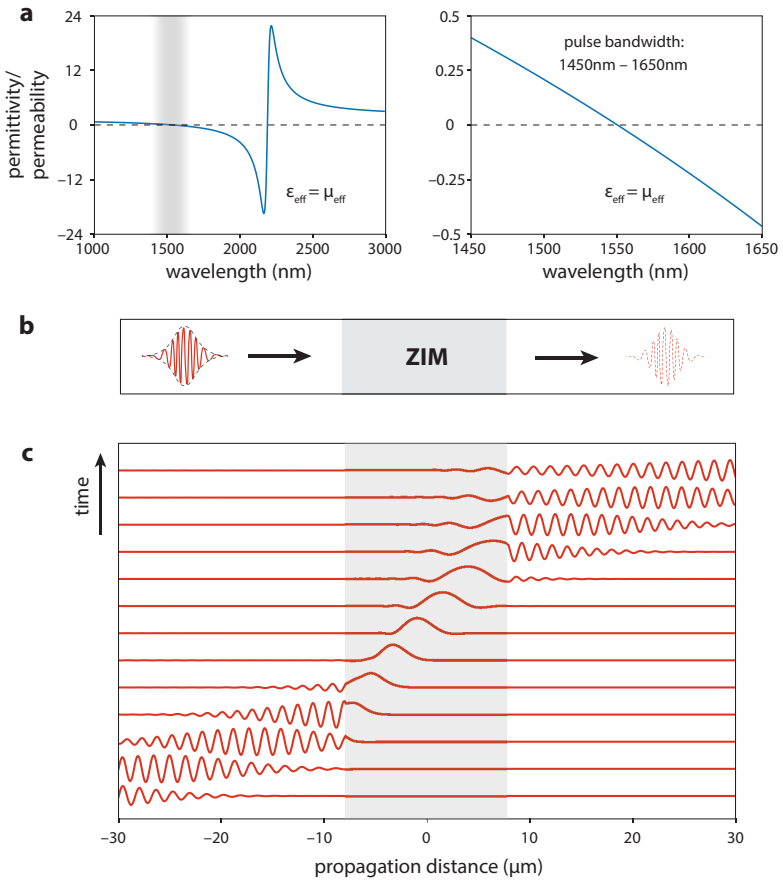

Figure 1.8: Pulse propagation in causal zero-index media. a) The zero-index medium is modeled as a matched pair of magnetic and electric Lorentzian oscillators. The spectrum of the permittivity/permeability shows a resonance near $\lambda = 2250$ nm, with a zero crossing at $\lambda = 1550$ nm. The grey bar indicates the spectrum of an incident pulse (1450 nm – 1650 nm). The figure on the right shows the permittivity and permeability within the spectrum of the pulse. b) We model the propagation of a transform-limited broadband pulse (1450 nm – 1650 nm) as it propagates through a 16-μm-thick zero-index slab. c) Electric field amplitude of the pulse during propagation. The grey band indicates the extent of the ZIM slab. Each field profile is separated by 31 fs, which is equivalent to 6 oscillation periods at the central frequency of the pulse.

propagates without distortion due to the linear dispersion of the material, exiting the slab at the far end and resuming its original speed. Figure 1.8c shows the distribution of fields within the slab through time. The velocity of the signal appears as the inverse of the slope, revealing the speed to be constant and subluminal throughout its propagation.

1.5 Outlook

Zero-index media represent an unexplored region of the material space, with unusual optical properties that are distinct from metals or dielectrics. Waves propagate with infinite wavelength and infinite phase velocity, filling the regions of zero index with uniform fields. While these phenomena promise a wealth of exciting technological applications and physical insights, any practical realization will require materials with extreme optical properties not commonly found nature. In particular, zero-index phenomena necessarily involve both an electric and magnetic material response (Appendix A). There is a wide range of optical materials with permittivity spanning positive and negative values, however there are no materials with non-trivial magnetic response at optical frequencies [22] (i.e. in natural materials, $\mu = 1$). The lack of optical magnetism is ultimately due to the absence of magnetic charges, which leaves only low-frequency magnetic interactions. As a result, there can be no naturally occurring materials with a refractive index equal to zero.

In this thesis, we will explore alternative approaches to realizing zero-index materials. Rather than relying on bulk optical properties, we can recreate the same effective material response by engineering the microscopic resonances within nanostructured metamaterials. Arrays of sub-wavelength dielectric cylinders can generate both electric and magnetic properties, functioning as a zero-index material (ZIM) at infrared wavelengths (Chapter 2). In Chapter 3, we demonstrate the potential of these metamaterials as super-couplers for optical

interconnects [23, 24]. Power transmission through optical waveguides is highly sensitive to bends or obstacles, especially for large multimode channels. By incorporating ZIM into the design of these waveguides, we demonstrate efficient coupling around arbitrary obstacles regardless of their size or shape due to the infinite wavelength associate with zero index.

Chapter 4 details an experimental demonstration zero-index metamaterials on an integrated photonics platform. The integrated design uses metal waveguides to emulate modes of infinite extent within a finite structure. We observe phase-free propagation through a ZIM prism, and experimentally extract the effective index. In order to fully exploit zero-index phenomena within integrated ZIM, the design must be scaled to macroscopic sizes comparable to the effective wavelength. However, the propagation length is limited by absorption and radiative loss in the material. Chapter 5 introduces an all-dielectric ZIM, which eliminates both ohmic and radiative loss using a bound state in the continuum (BiC).

Chapter 2

Zero-Index Metamaterials

Zero-index media represent a promising new class of optical materials, exhibiting a range of novel optical phenomena. However, the search for realistic materials in this regime is significantly hampered by strict requirements on the material impedance in order to ensure efficient transfer of energy through regions of zero index. Rather than considering the materials with near-zero permittivity (including many naturally occurring materials) efficient coupling is limited to cases where the permittivity and permeability are simultaneously zero. Unfortunately, there are no naturally occurring materials that satisfy these criteria due to a lack of magnetic response at optical frequencies (*i.e.* $\mu = 1$). Magnetic effects, including nuclear magnetic resonance and ferromagnetism, are restricted to low frequencies [22]. Without a magnetic response, there is no way to achieve efficient coupling into zero index materials.

Fortunately, there are has been significant interest in the development of artificial composite materials, including several examples of magnetic materials operating at optical frequencies [**?**, 25–28]. These metamaterials are designed in analogy with natural crystals, consisting of arrays of sub-wavelength resonant antennas or scatterers. When the constituent

elements are sufficiently small in comparison to the wavelength of light, the properties of the composite can be described by macroscopic quantities, including an effective permittivity and permeability. However, these properties are derived from optical response of the nanoscale antennas, as well as collective interaction throughout the crystal. This can give rise to a broad range of effective optical properties, including values not accessible by natural materials [29].

Despite their artificial origin, the optical properties of metamaterials can be understood in the same way as in natural materials. Recall that permittivity is the measure of how a material is polarized when subject to an applied electric field. We might imagine a block of some material between the plates of a capacitor. In the absence of free charges, the electric field within the capacitor causes the electrons in the material to become displaced from their respective atomic centers. Each atom forms a tiny electric dipole. The polarization density measures how many dipoles are excited per unit volume, and the associated permittivity is a measure of how much polarization density can be induced for a given applied field. In the case of a metamaterial, the polarizable atoms are replaced by nano-scale resonators, such as dielectric spheres. Much like atoms these particles also become polarized by the ambient electric field. This gives rise to an analogous polarization density and permittivity. However, now the packing density and the polarizability of the particles can be tuned as geometric properties of the composite, allowing control over the resulting effective permittivity.

The exact frequency dependence of the nanoparticle polarizability is described by Mie scattering theory, which systematically decomposes the polarization of a particle into an infinite series of resonant modes [27,30]. The relative strength of each resonance depends on the operating wavelength relative to the particle size, with lower multipoles arising before higher multipoles (e.g. dipoles are resonant at a lower frequency than quadrupoles). The scattering coefficient is typically small below the first resonance, so we may safely ignore all

but the first few terms in the expansion. For the purposes of zero-index metamaterials, we will focus on the Mie resonances of infinitely tall dielectric cylinders. Much like the spherical case, these are categorized using a multipole expansion, this time based on Bessel and Hankel functions. When a cylinder is excited perpendicular to its axis by TM polarized light (i.e. the electric field is polarized along the axis of the cylinder, shown in Figure 2.1a), the modes electric field in and around the cylinder can be separated into multipolar resonances:

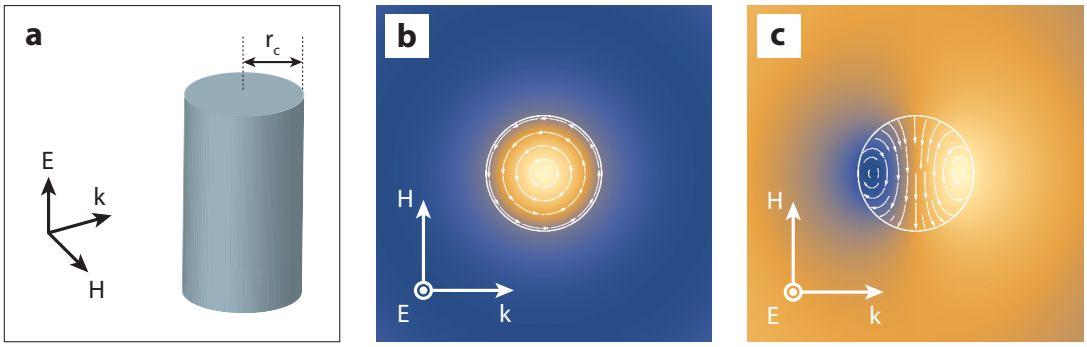

Figure 2.1: Light scattering from an infinite dielectric cylinder (a) can be decomposed as a series of Mie resonances. The lowest order terms are the monopole mode (b) and dipole mode (c). The colormap represents the out-of-plane electric field through a cross section of the cylinder. The magnetic field is indicated by the white arrows. The incident wave propagates perpendicular to the axis of the cylinder, and the electric field is polarized along the axis.

$$E_z(r) = \sum_m a_m J_m(kr) \exp im\theta + b_m H_m^{(1)}(kr) \exp im\theta \tag{2.1}$$

This expression applies to the interior and exterior of the cylinder, where coefficients a_m and b_m are determined according to the continuity of fields at the boundary, and are generally different inside and outside of the cylinder. J_m and $H_m^{(1)}$ are the Bessel and Hankel function of the first kind, respectively. If the wavelength is sufficiently long compared to the size of the cylinder, we can ignore all but the first two resonances: $m = 0$ (monopole) and $m = 1$ (dipole). The monopole mode is characterized by a strong dielectric response along

the axis of the cylinder, while the dipole mode is antisymmetric with differential polarization along the axis on either side of the cylinder (Figure 2.1b,c). This differential polarization can be thought of as a loop of displacement current, which generates a magnetic dipole moment that is mutually perpendicular to the electric field polarization and the propagation direction of the incident field. Notably, this is the same direction as the incident magnetic field, so the dipole mode can be considered to be a magnetic response despite the lack of intrinsic magnetism in the constituent materials (i.e. $\mu = 1$). Under these conditions, a metamaterial consisting of subwavelength arrays of dielectric cylinders can exhibit non-trivial effective permittivity and permeability at optical frequencies. Furthermore, we can adjust the magnitude of these effects via the geometry of the structure to ensure that both $\epsilon = \mu = 0$.

2.1 Effective Medium Theory

In order to design a zero-index metamaterial, we must establish a connection between the dimensions of the metamaterial and the effective optical response. Numerous mixing rules have been developed to describe the optical properties of composites, notably Maxwell-Garnett Theory [31] and Effective Medium Theory [32], but these methods typically operate in the dipole limit and ignore the contribution of higher multipolar terms. While this simplifies the analysis, it also decouples electric and magnetic effects, and is therefore inappropriate for descriptions of optical magnetism in resonant structures that may be comparable to the size of the wavelength in free space. Instead, we adopt an effective medium theory based on scattering cancellation in Mie resonant structures [33].

Briefly, the array of cylinders is treated as an effective medium with permittivity and permeability ϵ_{eff} and μ_{eff}, respectively. We consider a single dielectric cylinder surrounded

by an annulus of background dielectric (Figure 2.2a). We can solve for the Mie scattering coefficients corresponding to the monopole and dipole modes under the assumption that the operating wavelength in the effective medium is much larger than the size of the cylinder and the annular coating. The effective medium approximation is valid when both of these scattering coefficients vanish, in which case an infinite array of cylinders can support propagating Bloch waves. By enforcing this no-scattering condition, we arrive at the effective medium parameters [33]:

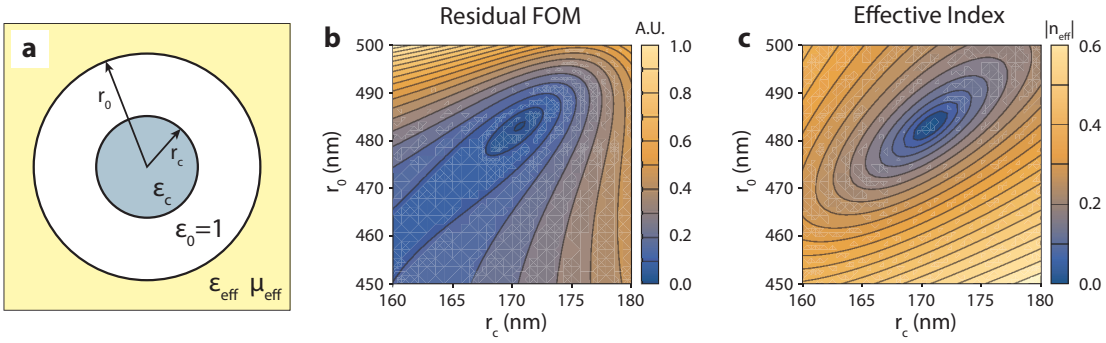

Figure 2.2: Effective medium theory. a) The composite is modeled as a dielectric cylinder of radius r_c surrounded by an annulus of radius $r0$ in an infinite background of homogeneous effective index. The annulus has index $n_0 = 1$, and the cylinder has index $n_c = 3.476$. b) Residual of the zero-index conditions (Eq. 2.5 and 2.6) calculated for a range of metamaterial dimensions. This quantity is minimized when effective permeability and permeability are simultaneously zero. c) Magnitude of the effective index calculated for the same range of metamaterial dimensions. The index is equal to zero when $r_c = 170$ nm and $r_0 = 483$ nm.

$$\frac{\epsilon_{\text{eff}} + 2\frac{J_0'(k_0 r_0)}{k_0 r_0 J_0(k_0 r_0)}}{\epsilon_{\text{eff}} + 2\frac{Y_0'(k_0 r_0)}{k_0 r_0 Y_0(k_0 r_0)}} = \frac{Y_0(k_0 r_0)}{iJ_0(k_0 r_0)}\left(\frac{D_0(\omega)}{1 + D_0(\omega)}\right) \tag{2.2}$$

$$\frac{\mu_{\text{eff}} - \frac{J_1(k_0 r_0)}{k_0 r_0 J_1'(k_0 r_0)}}{\mu_{\text{eff}} - \frac{Y_1(k_0 r_0)}{k_0 r_0 Y_1'(k_0 r_0)}} = \frac{Y_1'(k_0 r_0)}{iJ_1'(k_0 r_0)}\left(\frac{D_1(\omega)}{1 + D_1(\omega)}\right) \tag{2.3}$$

where $D_m(\omega)$ is the ratio of incident and scattered fields in the background medium for the m^{th} Mie resonance:

$$D_m(\omega) \equiv \frac{b_m}{a_m} = \frac{n_c J'_m(n_c k_0 r_c) J_m(k_0 r_c) - J_m(n_c k_0 r_c) J'_m(k_0 r_c)}{J_m(n_c k_0 r_c) H_m^{(1)}(k_0 r_c) - n_c J'_m(n_c k_0 r_c) H_m^{(1)}(k_0 r_c)} \tag{2.4}$$

k_0 is the wavevector in the background dielectric, r_0 is the radius of the background dielectric, and r_c is the radius of the cylinder. The refractive index within the cylinder and the background are n_c and n_0, respectively. Y_m is the Bessel function of the second kind. For a given array of dielectric cylinders, equations 2.2 and 2.2 give the frequency-dependent effective permittivity and permeability. Further, we may invert this process to determine the metamaterial structure that achieves an effective index equal to zero. Simplifying equations in the limit $\epsilon_{\text{eff}} \to 0$ and $\mu_{\text{eff}} \to 0$ results in a pair of conditions that must be satisfied in order to achieve $n = 0$,

$$\frac{iJ'_0(k_0 r_0)}{Y'_0(k_0 r_0)} = \frac{D_0(k_0 r_c)}{1 + D_0(k_0 r_c)} \tag{2.5}$$

$$\frac{iJ_1(k_0 r_0)}{Y_1(k_0 r_0)} = \frac{D_1(k_0 r_c)}{1 + D_1(k_0 r_c)} \tag{2.6}$$

We note that the left-hand side of each condition is a function of the size of the background region relative to the operating wavlength, $k_0 r0$. Similarly, the right-hand side depends only on the size of the cylinder relative to the operating wavelength, $k_0 r_c$, as well as the refractive index of the cylinder n_c. Therefore, these two relations determine a family of solutions for the two design parameters $k_0 r_0$ and $k_0 r_c$ that will generate an effective index equal to zero, which can be satisfied for cylinders with sufficiently high index n_c. High-index inclusions are necessary to ensure that the dipole resonance is excited at the operating wavelength, without which there can be no magnetic response. Figure 2.2b shows the residual of zero-index condition (Eq. 2.5 and 2.6), plotted as a figure of merit. In anticipation of an experimental demonstration using integrated optics, we will examine the case of silicon cylinders ($n_c = 3.476$) operating at a wavelength of 1550 nm, which requires

a cylinder radius $r_c = 170$ nm and pitch $a = \sqrt{\pi} r_0 = 856$ nm. The residual is minimized when the effective permittivity and permeability are simultaneously zero. In this case, the magnitude of the effective index is also zero (Figure 2.2c).

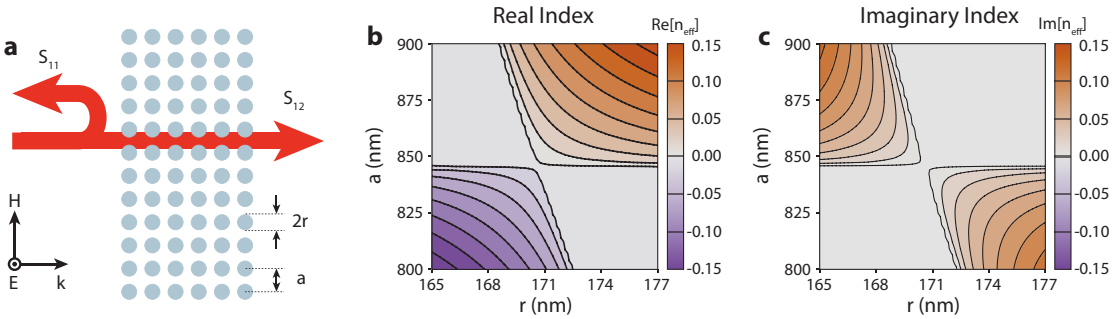

Figure 2.3: Parameter retrieval from scattering matrix elements. a) Effective optical properties are calculated from the complex reflection and transmission coefficients from a finite metamaterial slab, S_{11} and S_{21} respectively. b,c) Real and imaginary effective index at $\lambda = 1550$ nm calculated for a range of metamaterial dimensions. Both components equal zero when $r = 170$ nm and $a = 846$ nm.

We validate this design using full-wave electromagnetic modeling. The effective index can be extracted by simulating the complex reflection and transmission coefficients for a metamaterial slab under plane wave excitation (Figure 2.3) [34]. The slab is modeled as an effective medium with complex index and impedance, reflecting and transmitting some portion of the incident wave with a characteristic phase shift. By measuring both the amplitude and phase, we can unambiguously determine the real and imaginary components of the index and impedance[1]. Because this extraction method captures the response of the actual nanostructure, rather substituting it for an effective material, the extracted optical properties include any contributions from near-field coupling or spatial dispersion. In addition, the extraction can accommodate dispersive and absorptive materials, such that the results of this analysis are expected more closely represent a fabricated structure.

Starting from the preliminary optimum delivered by Effective Medium Theory, we

[1]The complex index and impedance are defined by four independent parameters, requiring four independent measurements. Similar retrieval methods use multiple-angle reflectometry [35].

extract the effective refractive index of a silicon pillar metamaterial at an incident wavelength of 1550 nm. In addition, we search the local parameter space to determine how the effective index varies with the radius and pitch of the array (Figure 2.3b,c). The optimum predicted by Mie Theory retains a small positive index at the design wavelength. The parameter search reveals an improved optimum at $r = 170$ nm and $a = 846$ nm, less than 2% deviation from the original prediction. The optimized structure has a real and imaginary index both equal to zero, which implies that the magnitudes of permittivity and permeability are also zero. Surrounding the optimum, the parameter space is divided into quadrants where the index is purely real or purely imaginary. This is reflective of different regimes of permittivity and permeability: the index is real when the permittivity and permeability are both positive or negative. If only one is negative, then the index becomes imaginary, corresponding to a photonic bandgap or plasma [30, 36]. These quadrants are therefore divided in the same fashion as the landscape of optical materials presented in Chapter 1 (Figure 1.1), including dielectrics, electric and magnetic plasmas, and negative-index materials.

Due to causality constraints, any metamaterial design (radius, pitch) may only exhibit a refractive index of zero at a single wavelength. The frequency-dependent index of the optimized design crosses zero at 1550 nm (Figure 2.4a) with negligible absorption, maintaining a constant impedance of $Z = 1.7$ across the measured spectrum. This will result in a small impedance mismatch with free space ($R \approx 6\%$) rather than the strong reflection associated with epsilon-near-zero media. Equivalently, the dispersion can be represented in terms of the effective permittivity and permeability, which are seen to cross zero simultaneously at the design wavelength (Figure 2.4b). The relative slope of these parameters at the zero-crossing determines the value of the impedance $Z = \sqrt{\mu/\epsilon}$. Since zero index at 1550nm is only available for a single set of geometric parameters, the effective impedance is a fixed parameter ultimately determined by the refractive index of the dielectric pillars.

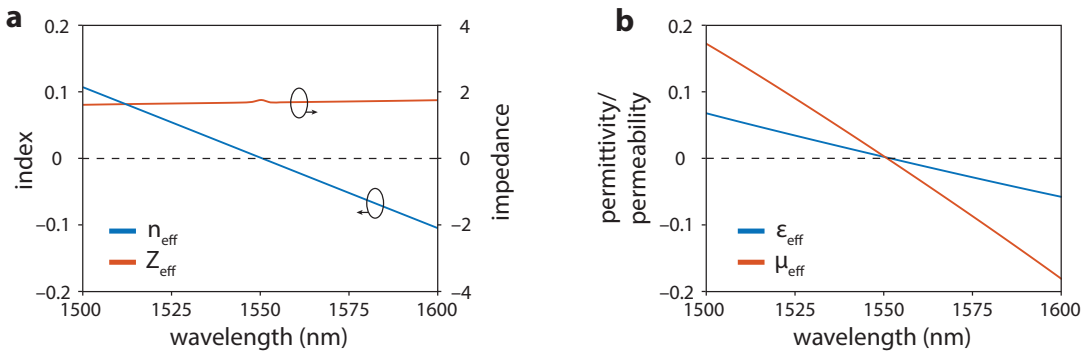

Figure 2.4: Effective optical properties of the optimized zero-index metamaterial. a) Effective index and impedance spectra, showing linear dispersion through $n = 0$ with constant impedance. Parameters are calculated from the scattering matrix of metamaterial slab with $r = 170$ nm and $a = 846$ nm. b) Effective permittivity and permeability spectra, showing simultaneous zero-crossing at $\lambda = 1550$ nm.

2.2 Bandstructure and Homogenization

We assign effective optical properties to a composite of subwavelength dielectric cylinders based on Mie theory and parameter retrieval. This amounts to a model of the behavior of the material under a range of illumination conditions, such that the flow of light can be described by a small number of parameters (n, Z, ϵ, μ). Generally the electromagnetic response of nanostructured materials can exhibit additional phenomena, such as diffraction, which are not captured by the effective medium model. In order to justify a macroscopic description, the metamaterial must satisfy additional homogenization criteria [37]: 1) passivity, 2) causality, 3) non-radiativity, and 4) isotropy.

The first criterion, passivity, is clearly satisfied for the zero-index metamaterial. The inclusions are composed of a low-loss dielectric, leading to a very low (but positive) imaginary index. The causality condition was addressed in Chapter 1. The permittivity and permeability both exhibit normal dispersion near the zero-index wavelength, such that the effective index is equal to zero at a single frequency. The third condition requires that

waves propagating through the metamaterial couple only to in-plane radiation, rather than scattering into other modes. This is equivalent to the requirement that there exists only a single propagating mode within the metamaterial at a given frequency, such that the effective index is single-valued. In addition, any reflections from the surface of the metamaterial must be free from diffraction (i.e. light couples to a single mode in free space). For a square array of cylinders this represents the classic diffraction limit, $a < \min(\lambda_0, \lambda_{eff})$, which is satisfied by the pitch $a = 846$ nm $\approx \lambda_0/2$. The final homogenization criterion concerns spatial dispersion of the effective index. Homogeneous materials exhibit an isotropic[2] refractive index, which is independent of the direction of propagation. In the context of Bloch modes, these materials follow circular isofrequency contours [38]. Inhomogeneous materials, such as photonic crystals, may support isofrequency contours of arbitrary shapes, leading to anomalous refractive effects [39]. This anisotropic index is characteristic of non-local interactions between constituent elements within the structure, and cannot generally be assigned to an effective medium. By extension, the equivalence of the zero-index metamaterial with bulk phenomena depends on isotropy of the effective index.

We examine the spatial dispersion of the zero-index metamaterial by calculating the propagating modes supported by the structure. The Bloch modes are periodic solutions to the wave equation within the microscopically inhomogeneous unit cell. Each mode is identified by its eigenfrequency and wavevector, which defines the direction of propagation. By computing the Bloch modes at each point in the reduced Brillouin zone we can fully characterize the behavior of electromagnetic waves within the metamaterial. Figure 2.5a shows the photonic bandstructure along the high-symmetry directions $\Gamma - \mathrm{M}$ and $\Gamma - \mathrm{X}$, plotted in terms of normalized eigenfrequency and normalized wavevector. The effective index of the propagating modes can be approximated by $n_{eff} \approx \frac{kc}{\omega}$, where k is the Bloch wavevector

[2]This criterion can be relaxed to allow for anisotropic homogeneous materials. However, even biaxial materials follow an index ellipsoid that is defined by at most three parameters.

representing the phase advance due to propagation. Therefore, zero index propagation is associated with modes at the Γ-point.

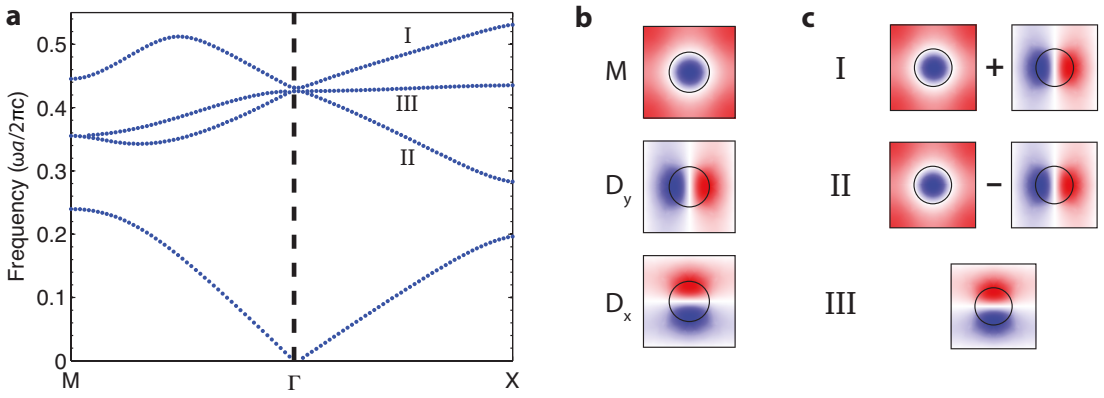

Figure 2.5: Bloch modes of the zero-index metamaterial. a) Band structure showing the in-plane Bloch modes within the reduced Brillouin zone along high-symmetry directions Γ−X and Γ−M. Zero index behavior arises due to the intersection of two bands with linear dispersion (I and II) and a dispersionless band (III). Frequency is normalized to the unit cell size a. b) Mode profiles of the three zero-index modes at the Γ-point, corresponding to a monopole ($\mathbf{M}$) and two perpendicular dipoles ($\mathbf{D_x}$ and $\mathbf{D_y}$). The colormap shows the out-of-plane electric field on a cross-section through the unit cell. The pillar boundary is indicated by the solid black line. c) Mode profiles of the three zero-index modes along Γ−X, corresponding to two hybrid modes (I: $\mathbf{M} + i\mathbf{D_y}$, II: $\mathbf{M} - i\mathbf{D_y}$) and a longitudinal dipole (III: $\mathbf{D_x}$).

At the design frequency ($\frac{\omega a}{2\pi c} = 0.43$) three bands intersect at the Γ-point ($k = 0$) creating a photonic Dirac cone. The bands can be separated according to dispersion: two modes maintain linear dispersion at the Γ-point, providing evidence of finite impedance and group velocity[3]. In addition, we observe a dispersionless "flat" band that corresponds to a non-propagating standing wave. The field distributions of these triply degenerate modes match the monopolar ($\mathbf{M}$) and dipolar ($\mathbf{D}$) Mie resonances of an isolated cylindrical inclusion. Due to the symmetry of the lattice, we are guaranteed to find two degenerate dipoles oriented along orthogonal directions. The linear bands near Γ can both be are constructed

[3]The group velocity is related to the curvature of the band [40], approaching $\nu_g = 0$ when the band is parallel to the horizotal axis. In the context of the effective index, this corresponds to a rapid change in index with increasing frequency.

from a linear combination of the monopole and dipole modes ($\mathbf{M} \pm i\mathbf{D}$) where the dipole is oriented perpendicular to the propagation direction. This combination of electric and magnetic resonances facilitates the simultaneous cancellation of the effective permittivity and permeability. The remaining longitudinal dipole forms the flat band, and is not excited by plane waves due to symmetry mismatch. Neglecting the presence of the flat band[4], the modes immediately above and below the zero-index frequency are interchangeable under mirror symmetry perpendicular to the propagation direction: $\sigma_x(\mathbf{M}+i\mathbf{D}) = \mathbf{M}-i\mathbf{D}$. Equivalently, the two bands can be represented as a single mode where the effective wavevector changes from positive to negative with linear dispersion at Γ. As this behavior is independent of the propagation direction, the photonic Dirac cone represents isotropic zero-index propagation in a homogeneous medium.

2.3 Comparison with bulk ZIM

Zero index phenomena, including phase-free propagation and omnidirectional radiation, are restricted to materials with simultaneously zero permittivity and permeability. Here, any applied electric or magnetic field induces an equal and opposite polarization field. Despite its non-magnetic constituents, the zero-index metamaterial can be represented as an array of electric and magnetic resonators, producing an analogous polarization in response to applied fields. We may therefore expect the metamaterial to exhibit the same electromagnetic phenomena as its bulk counterpart. For example, plane waves at normal incidence can excite fields with an infinite wavelength in a slab of zero-index metamaterial (Figure 2.6a). The incident light couples to Bloch modes that operate at the Γ-point, such that there is no phase accumulation between adjacent unit cells. Unlike bulk ZIM the field is non-uniform,

[4]This assumption is valid for excitation at normal incidence in the vicinity of the Dirac point due to symmetry mismatch. However, we may couple to the longitudinal dipole mode through near-field interactions (such as quantum emitters) or at frequencies below the zero-index frequency and oblique incidence.

with opposite polarity within the silicon cylinders. This behavior analogous to the fields near to the centers of atoms in natural materials–in both cases an induced dipole gives rise to a polarization field that opposes the incident field. Outside of the cylinders the electric field is relatively uniform, oscillating in unison throughout the slab. This field is communicated to the output facet of the metamaterial where it returns to free space. We observe efficient transmission through the slab due to the finite effective impedance.

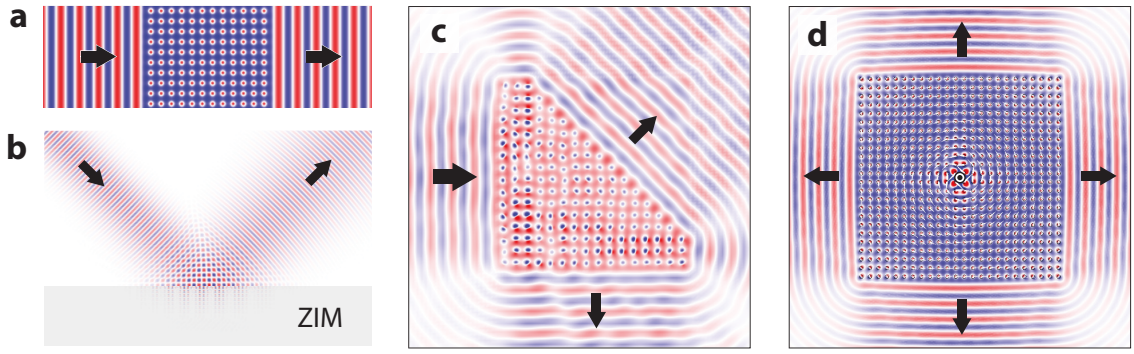

Figure 2.6: Waves in zero-index metamaterials. a) Plane waves propagate through a zero-index slab with uniform phase. b) Light incident at oblique angles is perfectly reflected from a finite zero-index slab due to TIR. c) Plane waves couple into zero-index modes of a triangular metamaterial prism. The quasi-uniform fields produce refracted beams that propagate normal to each interface. d) A point source radiates at the center of a square region of zero-index. The light couples to the long-wavelength modes in the metamaterial, which produce plane waves at the edges of the square. The colormap indicates the out-of-plane electric field.

In addition to phase-free propagation, the zero-index metamaterial exhibits the same refractive phenomena present in bulk ZIM. For example, refraction at the interface of a metamaterial "prism" is governed by Snell's law (Figure 2.6b), such that the refracted beam radiates normal to the interface. This surface-normal refraction is independent of the shape of the prism, and is caused by the uniform phase across interface. By extension, all facets of the zero-index prism generate a refracted beam normal to the surface. Conversely, exciting the prism at non-normal incidence creates a non-uniform phase along the interface, which

is incompatible with zero-index modes. Instead, the incident beam is perfectly reflected (Figure 2.6c). This is a manifestation of the critical angle for total internal reflection, which is 90° in ZIM. Such angularly-selective emission/reflection may improve the efficiency of photovoltaic devices [41, 42].

Finally, zero index metamaterials can function as transformation optics, allowing the extension of near-field effects to macroscopic spaces. This effect is especially important for quantum optics, where many-body phenomena are sensitive to the separation between emitters [17, 18]. By embedding an emitter within a region of zero index, the entire space is effectively within the near field due to the infinite wavelength. To demonstrate this effect in metamaterials, we simulate the fields excited by a point source at the center of a square array of cylinders (Figure 2.6d). In contrast to bulk ZIM, the emitter couples to an inhomogeneous field distribution within the metamaterial at the zero-index frequency (not shown) caused by the flat band at the center of the Brillouin zone. The flat band is a "dark" mode, not accessible through plane wave excitation, which is excited by the near field of the emitter. In order to avoid this effect, we simply shift the excitation to a shorter wavelength, $\lambda_0 = 1530$ nm, which corresponds to a small positive index, $n_{eff} = 0.04$. At this wavelength the metamaterial supports a single propagating mode, satisfying the homogenization criteria. Thus, the point source couples efficiently to long-wavelength modes in the metamaterial, in close agreement with bulk ZIM. These modes couple to plane waves at the boundary, where the omnidirectional radiation pattern is transmuted to match the shape of the zero-index region.

2.4 Conclusion

Maxwell's equations predict unusual optical phenomena in materials with extreme optical properties, but these materials may be difficult or fundamentally impossible to realize. In the case of zero-index waves, the permittivity and permeability must simultaneously vanish – an unlikely combination due to the lack of optical magnetism in nature. Optical metamaterials represent an alternative avenue for light matter interaction, in which the material response is derived from the engineered resonances of subwavelength antennas rather than atoms. From this perspective we can extend the range of optical properties beyond the limits of natural materials, including optical magnetism from an all-dielectric structure. Through degeneracy of electric and magnetic resonances in silicon cylinders, we have designed a metamaterial with simultaneously zero permittivity and permeability, which behaves as a zero-index material at optical frequencies. Such realistic zero-index metamaterials will allow access to previously unexplored optical phenomena.

Chapter 3

Waveguiding in Zero-Index Media

Advances in modern computing architecture point toward a future at the confluence of electronics and photonics, where processors incorporate optical interconnects designed to speed communication and augment the capabilities of their electronic counterparts [43]. Despite the diversity of on-chip optical components, the majority of integrated photonic circuits are based on a single material platform–silicon. This dictates the scope of optical effects that can be performed on a chip, as well as the length scales involved. For example, the density of integration is limited by the physical size of optical waveguides used to shuttle signals between components. Silicon waveguides are unable to maintain confinement around tight corners (roughly 5μm bend radius), so interconnects are forced to trace gradual curves over large areas.

Recent advances in nanofabrication promise to expand the range of available optical properties that can be achieved within the framework of silicon photonics, including properties not seen in nature [29]. In Chapter 2 we demonstrated a silicon-based metamaterial with a refractive index equal to zero, which allows access to a range of novel optical phenomena [23, 44–48]. When the index approaches zero, the spatial and temporal dependence

of the optical fields become decoupled, allowing access to "static optics" at infrared frequencies [49]. This results in characteristically different flow of electromagnetic energy through zero-index media, formally equivalent to the flow of current through metallic wires.

In this chapter, we explore the dynamics of optical waveguiding in zero-index media. Such "supercouplers" achieve anomalously high transmission through narrow channels due to the extremely long effective wavelength in ZIM, which allows efficient power transfer around sharp bends or bottlenecks [23, 24, 44]. Similarly, signals can easily be split among many output ports, or combined together. We develop an analytical model to describe the propagation of waves though zero-index channels, and use it to design efficient optical interconnects of arbitrary size and shape. The unique properties of zero-index metamaterials allow compact manipulation of light at the nanoscale, with immediate and far-reaching implications for integrated optics.

3.1 Zero-Index Waveguide Modes

Optical waveguides control the flow of light by confining the energy to a finite region, such as the core of an optical fiber. The electromagnetic fields are modified by their interaction with the boundaries of the waveguide, resulting in a field distribution that depends on the geometry of the waveguide as well as its constituent materials. This interaction can be viewed as an eigenvalue problem, which models the evolution of guided waves as they propagate along the waveguide. The associated eigenmodes represent field distributions that are unchanged during propagation. We may therefore understand the behavior of guided waves in terms of the modes of the waveguide, in the same way that plane waves are a convenient basis for geometric optics.

In order to understand the propagation of light through zero-index waveguides, we

study the modes that propagate in the space between two parallel conductors[1] (Figure 3.1). This structure supports a discrete set of eigenmodes, which are categorized by their dominant polarization: TE, where the electric field is polarized out-of-plane, and TM where the magnetic field is polarized out-of-plane. For each polarization, there is an infinite series of modes, which are characterized by sinusoidal field variation in the transverse direction [50]. The modes propagate with an effective wavevector β_m, which depends on separation between the conductors, a, as well as the refractive index within the waveguide, n.

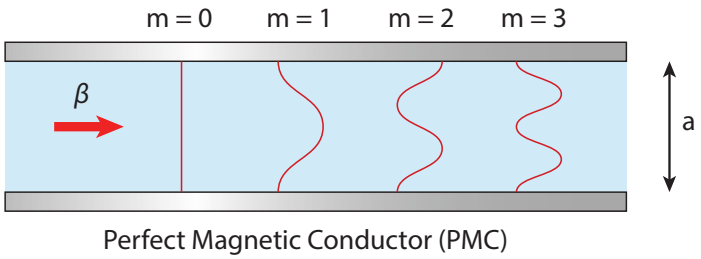

Figure 3.1: Guided modes in a parallel plate waveguide. Waves propagate in a dielectric slab in between two conductive planes deparated by a distance a. The boundaries are perfect magnetic conductors, which eliminate the tangential component of the magnetic field at the boundary. The waveguide supports a series of transverse electric (TE_m) and transverse magnetic (TE_m) modes, identified by the mode index $m = 1, 2, 3, \ldots$. Each mode has a sinusoidally varying field in the space between the conductors, and propagates with a wavevector β_m. The waveguide also supports a transverse electromagnetic mode (TEM), where the electric field is polarized in the plane of the conductive boundaries.

$$\beta_m = \sqrt{\omega^2 n^2 - \left(\frac{m\pi}{a}\right)^2} \qquad m = 1, 2, 3, \ldots \tag{3.1}$$

where m is the mode index, representing the number of nodes in the transverse mode profile. Thus, the effective wavevector depends on the mode index, and higher-order modes propagate with a lower wavevector. For sufficiently high mode index, the wavevector is imaginary and the mode becomes evanescent. Equivalently, there exists a cutoff frequency f_m, below

[1]There are many other waveguide configurations that support guided modes, such as dielectric and photonic crystal waveguides [50, 51]. The phenomenon of zero-index waveguiding is not specific to parallel conductors, which simply provide a convenient test case.

which a given mode will not propagate within the waveguide,

$$f_m = \frac{m}{2an} \tag{3.2}$$

The cutoff frequency occurs when spatial frequency of the mode profile exceeds the wavevector in the background dielectric. These modes can no longer be decomposed in the basis of plane waves, and therefore represent bound states [30]. Thus, a given waveguide geometry only supports a finite set of propagating modes.

In addition to TE and TM modes, the waveguide supports a plane-wave mode (TEM) where the electric and magnetic fields are mutually perpendicular to the propagation direction with uniform field amplitude between the conductors. This mode propagates with the wavevector of the background medium, $\beta_0 = \omega n$, and persists at all operating frequencies. The polarization of the mode is defined by the nature of the conductor – here, we assume the boundaries are perfect magnetic conductors[2] (PMC), such that the electric field of the TEM mode is oriented parallel to the conductor, out-of-plane.

The set of guided modes (TE_m, TM_m and TEM) is fully determined by the waveguide geometry, background index, and operating frequency. In particular, the cutoff frequency scales inversely with the background index, such that a lower-index waveguide supports fewer modes. As the background index approaches zero, the cutoff frequency grows without bound until all guided modes are eliminated, except for the TEM mode, which is always present. This effect is independent of the waveguide size, provided the index is sufficiently small. A zero-index waveguide *always* supports a single propagating mode.

[2]Unlike perfect electric conductors, there is no naturally occurring analog of PMCs due to the lack of optical magnetism [22]. However, many artificial magnetic conductors have been demonstrated for free-space optics [52, 53] and integrated photonics [54]

3.2 Transmission Through Tapered Waveguides

Single-mode operation dramatically simplifies the analysis of guided waves in zero-index media, which can be fully described by the amplitude and phase of the TEM mode. Moreover, it provides an intuitive model of propagation through waveguides of arbitrary shapes. For example, we may consider a zero-index waveguide with an abrupt taper (Figure 3.2a). Despite its changing cross-section, the waveguide only permits the propagation of the TEM mode at any point along the propagation direction. The only effect of the changing geometry is to reflect a portion of this mode. Therefore, we may understand the propagation through this structure simply by calculating the proportion of forward and backward propagating waves in each segment.

We calculate the reflectance at the tapered interface via numerical simulations (Figure 3.2b,c), comparing a range of different waveguide tapers. As the severity of the taper increases, a greater fraction of the incident wave is reflected. The reflection is also stronger when the background index is larger, especially when the effective wavelength in the material approaches the size of the waveguide. Beyond this point the waveguide supports multiple modes, and the incident wave is strongly reflected. However, even when the index is zero the transmission is less than 100%, and we cannot ignore the effect of the taper.

We can estimate the reflection from the taper in the zero-index limit based on the modified wave equation in ZIM. From equations 1.4 and 1.5, electric and magnetic fields are irrotational. Thus, the out-of-plane electric field must be uniform throughout the waveguide. However, the in-plane electric field may vary along the propagation direction. Due to conservation of energy, the powerflow through a cross section of the waveguide must be constant at every point along the propagation direction, so the fields on either side of the taper can be related by the Poynting vector, $\vec{S} = \vec{E} \times \vec{H}^*$,

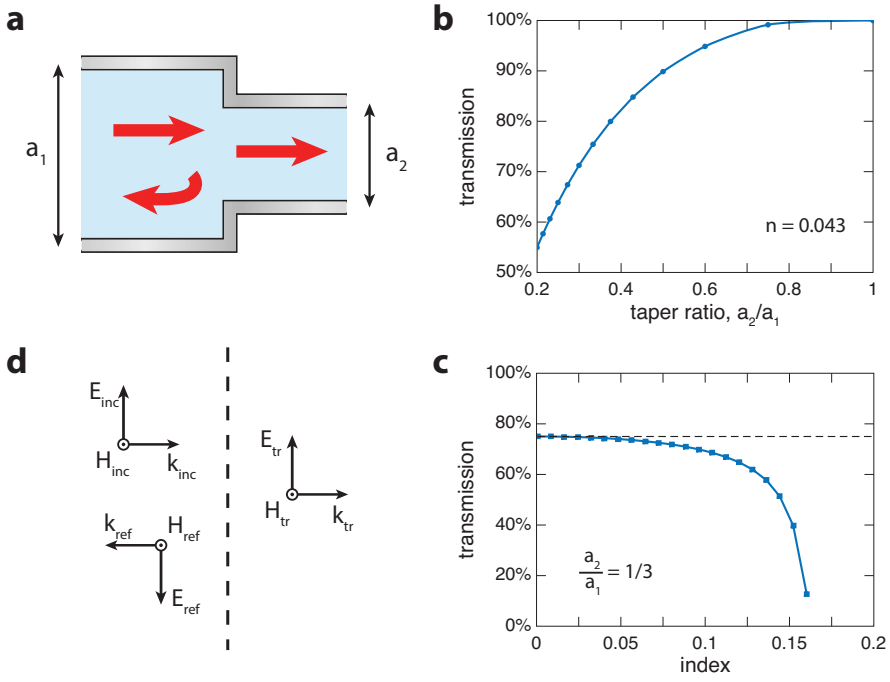

Figure 3.2: Reflection from an abruptly tapered waveguide. a) The guided mode is reflected at a junction between two waveguides with the same background index, but different widths a_1 and a_2. The reflected power increases for more extreme taper ratios (b) and for larger background index (c). In figure (b), the background index is fixed at $n = 0.043$. In figure (c), the taper ratio is fixed at $a_2/a_1 = 1/3$. d) The reflection can be modeled as the superposition of incident and reflected plane waves. This model predicts the reflectance in zero-index waveguides, and is indicated by a dashed line in figure (c).

$$\int S \cdot d\hat{n} = a_1 \vec{E} \times \vec{H}_1^* = a_2 \vec{E} \times \vec{H}_2^* \tag{3.3}$$

$$\Rightarrow \frac{H_1}{H_2} = \frac{a_2}{a_1} \tag{3.4}$$

Thus, the taper is associated with a decrease in the magnetic field relative to the electric field. In the context of TEM modes in a zero-index waveguide, this is equivalent to a superposition of incident and reflected waves (Figure 3.2d). By matching the fields on either side of the taper, we recover the reflected and tranmitted amplitudes,

$$E_{\text{inc}} + E_{\text{ref}} = E_{\text{tr}} \quad \rightarrow \quad 1 + r = t \tag{3.5}$$

$$H_{\text{inc}} - H_{\text{ref}} = H_{\text{tr}} \frac{a_2}{a_1} \quad \rightarrow \quad 1 - r = t \frac{a_2}{a_1} \tag{3.6}$$

Combining equations 3.5 and 3.6, we arrive at the coefficients for power transmission and reflection,

$$T = t_{1\rightarrow 2} t_{2\rightarrow 1} = \frac{4 a_1 a_2}{\left(a_1 + a_2\right)^2} \tag{3.7}$$

$$R = r_{1\rightarrow 2}^2 = \left(\frac{a_1 - a_2}{a_1 + a_2} \right)^2 \tag{3.8}$$

This calculated transmission is shown as a dashed line in Figure 3.2c, and matches closely with the numerical simulation near zero index.

The reflection from the taper is a consequence of the enhanced magnetic field in the narrow region, where the electric field is unchanged. It is convenient to describe this phenomenon in terms of the wave impedance $Z = \frac{E}{H}$ [50]. This is related to the intrinsic impedance of the background material $Z_{\text{int}} = \sqrt{\frac{\mu}{\epsilon}}$, which represents the wave impedance of unbounded plane waves in a homogeneous medium, except that the wave impedance

includes the effect of the waveguide geometry. In the case of a zero-index waveguide, the taper causes the wave impedance to be scaled by a factor equal to the ratio of the input and output widths.

In this context, the zero-index waveguide can serve as a compact impedance matching structure between two dissimilar materials, allowing efficient power transmission. For example, we model the transmission through a tapered zero index waveguide (Figure 3.3a), which connects an air-filled waveguide ($n_{\text{in}} = 1$) to a waveguide filled with a homogeneous dielectric[3] ($n_{\text{out}} = 1.57$). Since the input and output waveguides are filled with non-magnetic materials, the wave impedance in each is given by the inverse of the refractive index. This impedance mismatch typically causes a reflection at the interface between two materials that is proportional to the difference in the impedance,

$$R = \left(\frac{Z_{\text{in}} - Z_{\text{out}}}{Z_{\text{in}} + Z_{\text{out}}} \right)^2 \tag{3.9}$$

However, the waveguide taper effectively rescales the wave impedance during propagation in proportion to the taper ratio. Thus, we may eliminate the reflection due to impedance mismatch for a particular taper ratio,

$$\frac{a_{\text{in}}}{a_{\text{out}}} = \frac{Z_{\text{in}}}{Z_{\text{out}}} \tag{3.10}$$

Figure 3.3b shows the simulated transmission through the impedance-matching tapered waveguide with for a range of taper ratios. We calculate the transmission for a waveguide filled with a homogeneous zero-index medium, as well as the silicon-based ZIM. Both simulations agree closely with the analytical model based on the wave impedance, with

[3]Impedance matching in zero-index waveguides can be achieved for arbitrary input and output materials, provided the metamaterial can be homogenized at the interface (Section 3.6). This choice of dielectric index happens to correspond to SU-8, a polymer used in the experimental demonstration of integrated ZIM (Chapter 4).

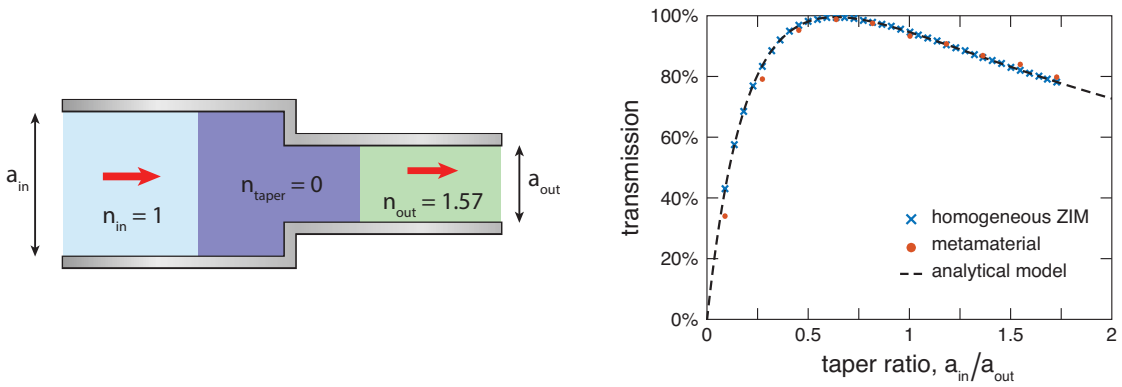

Figure 3.3: Impedance matching with tapered zero-index waveguides. a) Two waveguides filled with different materials ($n_{in} = 1$ and $n_{out} = 1.57$) are connected by a tapered zero-index waveguide. b) The power transmission from the input to the output waveguide is dependent on the relative widths of the two waveguides, a_{out}/a_{in}. When the taper ratio is equal to the inverse of the index ratio, $a_{out}/a_{in} = n_{in}/n_{out} = 0.64$, the two waveguides are impedance matched and the coupling efficiency reaches 100%. This analytical model is corroborated by finite element simulations with a homogeneous zero-index medium, as well as a silicon-based zero-index metamaterial.

perfect transmission through a taper ratio of 1.57. This approach to impedance matching depends solely on the transverse cross section of the zero-index waveguide, unlike traditional methods based on adiabatic tapers [55] or gradient index [56]. In addition to a simplified design process, this method allows efficient power coupling over a dramatically shorter propagation distance (>10 μm), which is relevant for high-density integrated photonics [43].

3.3 Resonant Tunneling Through Arbitrary Waveguides

The model of propagation through a zero-index waveguide is easily extended to waveguides of arbitrary cross section, including multiple tapers or bends (Figure 3.4a), provided the index is low enough to ensure single-mode operation. In general each taper will produce a finite reflection due to an impedance mismatch, as detailed in the previous section. Waveguides with multiple dislocations will therefore accumulate multiple reflected waves, which

may interfere with each other. However, each segment within the waveguide can be fully characterized by the phase and amplitude of the reflected and transmitted TEM mode. The overall transmission through this structure will depend on the relative phase and amplitude of these reflections, as well as the phase accumulated during propagation between interfaces.

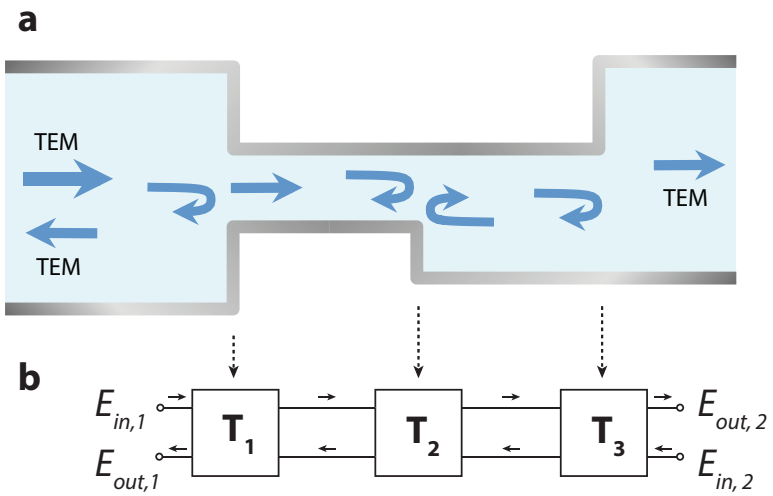

Figure 3.4: Modeling arbitrarily shaped zero-index waveguides. a) As waves propagate through a multi-junction waveguide, each taper or material interface produces a reflected wave. b) Since the waveguide supports a single propagating mode, the interference from multiple reflections can be modeled using a transfer matrix method. Each interface is represented by a 2×2 transfer matrix, which relates the forward and backward propagating TEM mode amplitudes on either side of the interface. The product of the individual transfer matrices is used to characterize the transmission through the waveguide.

This behavior is formally equivalent to the transmission through a multilayer dielectric stack. Each interface is characterized by a reflection and transmission coefficient, which connects the fields on either side of the interface. In the case of the waveguide, these reflections are due to a changing cross section rather than a change in the material properties between layers. Based on this correspondence, we model the transmission through a tapered waveguide using the transfer matrix method [57].

The waveguide is treated as a series of discrete elements, each defined by a transfer matrix $\mathbf{T}$ that relates the incoming and outgoing waves on either side of the interface (Figure 3.4b). For example, a waveguide taper is represented as

$$\mathbf{T} = \frac{1}{t}\begin{bmatrix} 1 & r \\ r & 1 \end{bmatrix} \tag{3.11}$$

$$\begin{bmatrix} E_{\text{in},2} \\ E_{\text{out},2} \end{bmatrix} = \mathbf{T}\begin{bmatrix} E_{\text{in},1} \\ E_{\text{out},1} \end{bmatrix} \tag{3.12}$$

where r and t represent the transmission and reflection coefficients of the electric field, respectively. These coefficients may be complex, accounting for a phase shift upon reflection or transmission. Similarly, we define a transfer matrix to represent the phase accumulated during propagation along a straight waveguide of length d,

$$\mathbf{T} = \begin{bmatrix} \mathrm{e}^{ink_0 d} & 0 \\ 0 & \mathrm{e}^{-ink_0 d} \end{bmatrix} \tag{3.13}$$

Finally, the overall transfer matrix for an arbitrarily complicated structure constructed as the matrix product of the individual elements.

$$\mathbf{T}_{\text{total}} = \begin{bmatrix} T_{11} & T_{12} \\ T_{21} & T_{22} \end{bmatrix} = \mathbf{T}_1 \times \mathbf{T}_2 \times \mathbf{T}_3 \times \dots \tag{3.14}$$

and the transmission coefficient is equal to $|T_{22}|^{-}2$

To evaluate this model, we simulate the transmission through a zero-index waveguide consisting of three interfaces: a taper and two impedance mismatched facets. The waveguide is filled with a zero-index metamaterial, with an intrinsic impedance $Z_{\text{int}} = 1.7$, and

is connected to two air-filled waveguides of different widths (Figure 3.5a). We measure the transmission through the waveguide at an operating wavelength $\lambda = 1530$ nm, where the metamaterial has a small positive index $n_{\mathrm{ZIM}} = 0.043$. Due to the finite index, the transmission is sensitive to the length of the waveguide, which affects the relative phase of the multiple reflected waves. Figure 3.5b shows the power transmission for a range of waveguide lengths L_1, while the second segment maintains a constant length $L_2 = 12.6\mu$m. The transfer matrix model agrees closely with the simulated transmission, which oscillates as the waveguide length increases. The oscillation period is equal to one-half effective wavelength, indicative of a Fabry-Perot resonance. The higher order oscillation in the transmission spectrum reflects the interference between multiple such resonances, although the interference is not perfectly constructive for any individual waveguide length L_1.

The analytical transfer matrix model allows efficient evaluation of the power transmission through arbitrary waveguide configurations. For example we can vary the lengths of both segments simultaneously in order to achieve efficient power transfer through the tapered waveguide. Figure 3.5c shows the power transmission for a range of lengths L_1 and L_2, which reaches 100% for specific combinations. The simulations corresponding to Figure 3.5b are shown as a dashed line. Figure 3.5d shows the electric field of waves propagating through the optimized design without reflection. This effect is distinct from the impedance matched taper presented in Section 3.2, and does not require a waveguide index equal to zero. Instead, the efficient transmission is due to resonant tunneling [58, 59], which can be used to couple between waveguides of arbitrarily different sizes and intrinsic impedances.

The resonant tunneling effect can be used to achieve efficient propagation through a variety of different waveguide geometries, which are summarized in Figure 3.6. The sharp bends are modeled in the same manner as the waveguide taper, producing a reflected TEM wave which contributes to the multiple Fabry-Perot resonances of the structure. By adjusting

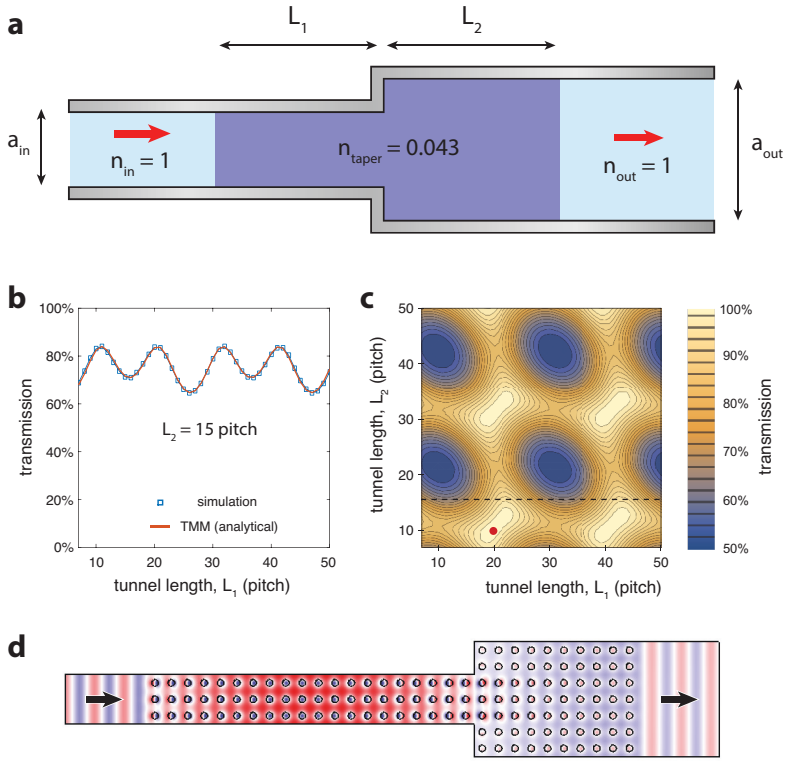

Figure 3.5: Resonant tunneling through multiple waveguide interfaces. a) We model the transmission through a tapered waveguide, filled with a small positive index $n_{\text{taper}} = 0.043$ at a wavelength of $\lambda = 1530$ nm. The input and output waveguides are filled with air ($n_{\text{in}} = n_{\text{out}} = 1$), with widths of 2.6 μm and 6 μm, respectively. The intrinsic impedance of the tapered region $Z_{\text{int}} = 1.6$ leading to reflection at the interface with the input and output waveguides. b) Power transmission through the tapered waveguide for a range of taper lengths L_1. The second waveguide segment maintains a fixed length $L_2 = 12.6\mu$m. The transfer matrix model (red) agrees closely with numerical simulations of metamaterial-filled waveguides (blue). c) Power transmission with simultaneous variation of both taper lengths, L_1 and L_2, based on the analytical model. The model predicts multiple designs that achieve perfect coupling, including an optimum with lengths $L_2 = 8.5\mu$m and $L_2 = 17\mu$m. The dashed line indicates the taper designs shown in figure (c). d) Electric field in the optimized taper design showing 99% power transmission through a metamaterial taper. The colormap indicates the out-of-plane electric field.

the lengths of the waveguide segments, we can ensure constrictive interference between these resonances. This process is eased by the long effective wavelength in the ZIM, allowing fine control of the effective propagation phase despite the discrete nature of the metamaterial. Thus, zero-index waveguides can achieve efficient transmission through narrow channels, 90° and 180° bends, and abrupt tapers. The transmitted wave emerges from the zero-index region with a uniform wavefront due to the symmetry of the TEM mode.

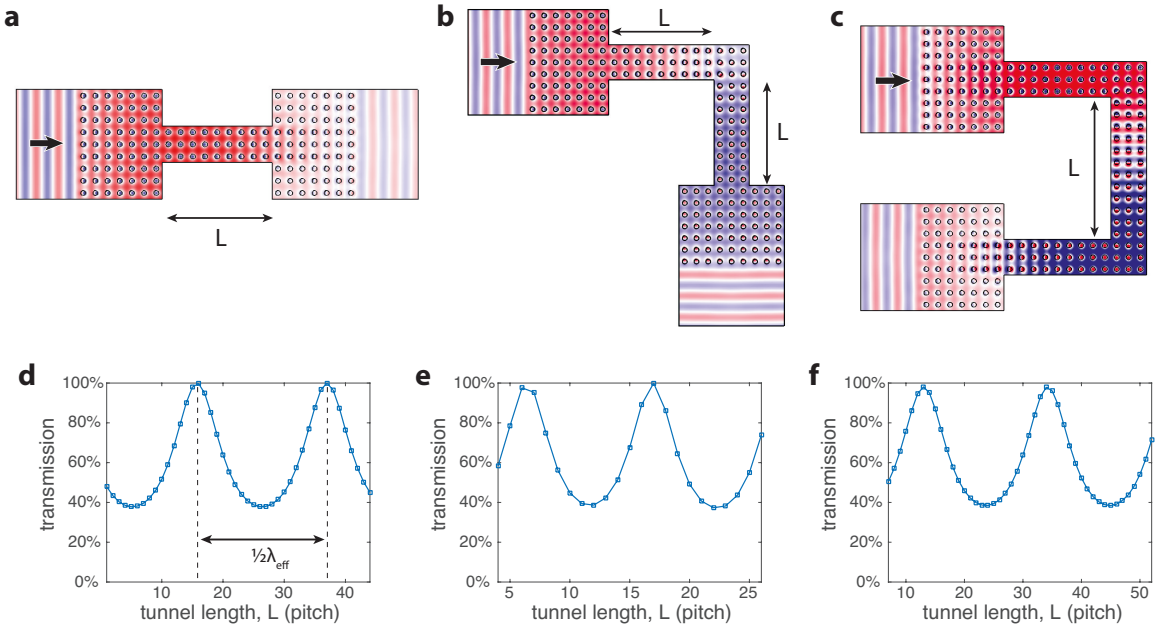

Figure 3.6: Resonant tunneling through 90° bends. a-c) Electric fields in different tapered waveguide configurations. Each waveguide achieves efficient tunneling through a metamaterial with effective index $n = 0.043$ at a wavelength $\lambda = 1530$ nm, despite multiple bends and tapers. d-f) The transmission efficiency through the waveguide depends on the length of the tapered channel, L. Each design achieves perfect transmission for an optimum length, which is repeated for designs where the tunnel length differing by one-half effective wavelength.

Zero-index waveguides can also be used as a kind of electromagnetic invisibility cloak, as incoming plane waves are perfectly transmitted through a zero-index slab, regarless of any inclusions (Figure 3.7). Here, the cloaked object is an square region surrounded by a perfect magnetic conductor. Without the presence of the zero-index metamaterial, this

object produces strong reflections (roughly 25%) and a distorted wavefront. Because the cloaking effect is due to resonant tunneling through the metamaterial, rather than a coordinate transformation [60], protection from scattering is restricted to plane waves at normal incidence[4]. However, this effect may be used to efficiently couple light around scattering objects in integrated photonic circuits, such as vias and or electronic components, allowing greater design flexibility.

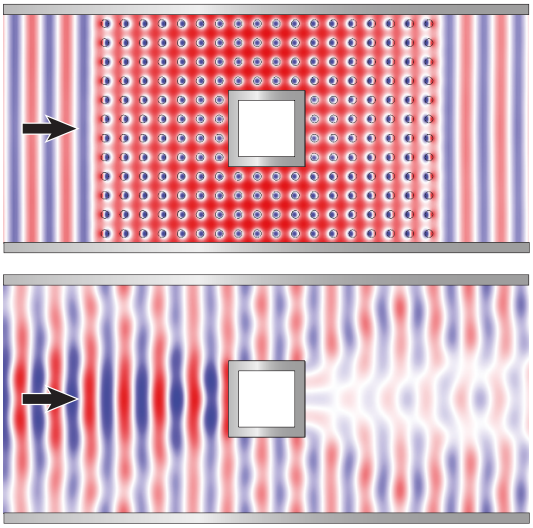

Figure 3.7: Invisibility cloaking in zero-index waveguides. (top) A square region with conductive boundaries is protected from scattering when placed within a low-index slab. Incident plane waves couple to the TEM mode, and propate past the obstruction without reflection. (bottom) If the low-index slab is removed, the same obstruction produces strong distortions in the transmitted wave, and reflects roughly 25% of the incident power.

3.4 Zero-Order Resonance

Resonant tunneling through zero-index waveguides can be achieved when the length of the waveguide is comparable to the effective wavelength of the guided mode. Therefore,

[4]In fact, obliquely incident waves are perfectly reflected from the surface of the zero-index metamaterial, due to total internal reflection. Only the TEM mode is allowed to propagate through the waveguide.

the minimum size of tunneling devices (as shown in Figure 3.6) scales with the effective wavelength, which can be reduced by operating at higher frequencies. Due to the scale invariance of Maxwell's equations [60], the same result is achieved by filling the waveguide with a higher-index material.

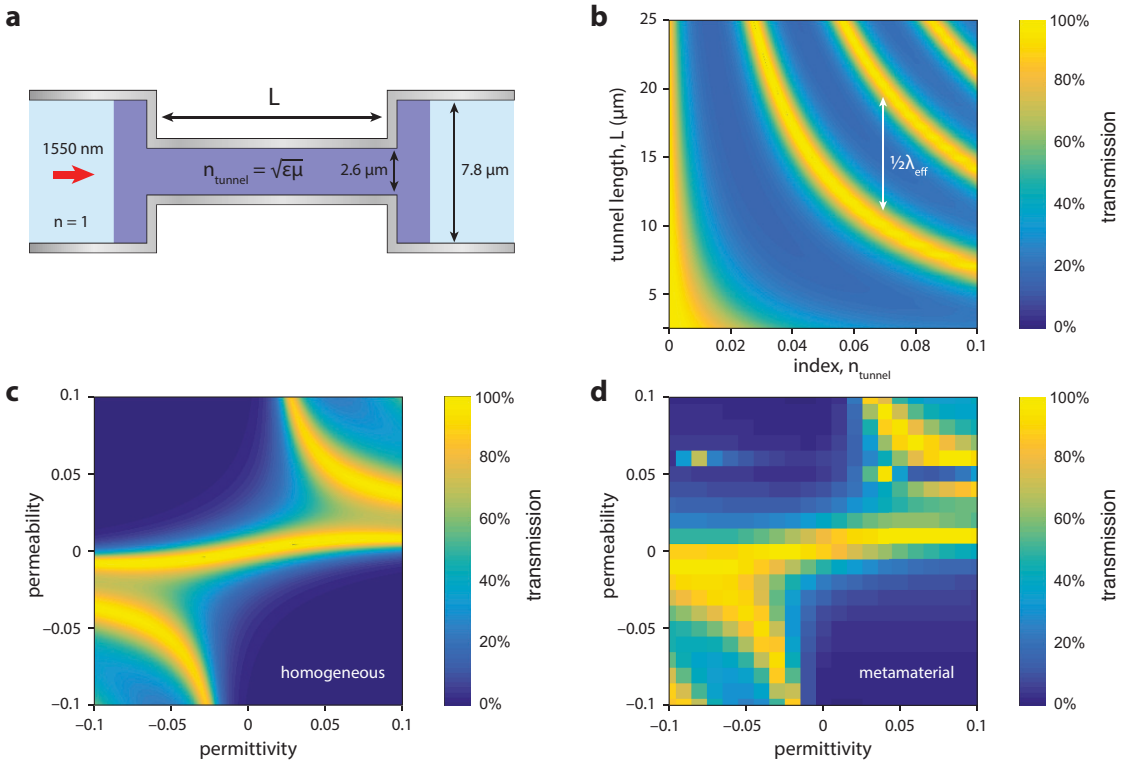

Figure 3.8: Zero-order resonance. a) Power transmission through a low-index tapered waveguide depends on the tunnel length L, as well as the index of the tunnel $n_{\text{tunnel}} = \sqrt{\epsilon\mu}$. b) Power transmission through low-index tunnels with various indices and tunnel lengths. The intrinsic impedance of the tunnel is fixed at $Z_{\text{int}} = 1.6$, and the material is modeled as a homogeneous dielectric. c) Power transmission through a tunnel of length $L = 13\mu\text{m}$, where the tunnel is filled with a homogeneous dielectric of varying permittivity and permeability. d) Power transmission through a metamaterial-filled tunnel with the same dimensions and range of material properties as in (c).

Figure 3.8 shows the simulated power transmission through a narrow channel for a range of refractive indices. As the length of the channel L increases, the transmission spikes periodically, indicating resonant tunneling through the waveguide [58]. The difference in

channel length between two resonances is equal to the effective wavelength of the guided mode, which becomes shorter as the index increases. Therefore, the minimum channel length is equal to one-half effective wavelength, $L_{\min} = \frac{\lambda_0}{2n}$.

As the index approaches zero, $L_{\min}$ diverges, and there is no Fabry-Perot resonance in a waveguide of finite size. However, the transmission is strongly peaked near zero index, corresponding to an infinite effective wavelength. In this limit, any finite waveguide is infinitesimal compared to the effective wavelength, resulting in a zero-order Fabry-Perot resonance [24]. As this condition applies to any waveguide length, we observe efficient power transfer through a zero-index waveguide regardless of its size. The waveguide achieves high transmission, despite the effective impedance mismatch due to the taper. Similarly, the zero-order resonance (ZOR) persists even if the intrinsic impedance of background medium is mismatched with the surrounding air. This scheme has been applied to achieve efficient transmission through materials with either $\epsilon = 0$ or $\mu = 0$, where the intrinsic impedance is singular.

In order to understand this insensitivity to impedance mismatch, we examine the transmission through the tapered waveguide filled with different combinations of permittivity and permeability. Figure 3.8a shows the power transmission through a 15.5-μm-long tapered waveguide filled with a homogeneous material, while Figure 3.8b shows the corresponding simulations for a silicon-based metamaterial. By manipulating both the permittivity and permeability, we simultaneously probe the effects of the index and the impedance on the tunneling efficiency. On these axes, curves of constant index are hyperbolas, while lines of constant impedance trace straight lines through the origin.

The parameter sweep reveals two loci that lead to efficient transmission: a pair of hyperbolas in the upper right and lower left quadrants, as well as a line through the origin. The hyperbolas correspond to a refractive index $n \approx \pm 0.05$, where the effective wavelength

is twice the length of the waveguide. These curves represent the first-order Fabry-Perot resonance. The straight line passing through the origin is the ZOR, which is characterized by a constant impedance $Z \approx 9$. This analysis shows that efficient transmission can be extended beyond zero index, including a continuous range of positive and negative values.

The slope of the ZOR line is determined by the waveguide geometry, and is the result of impedance matching through the taper. In section 3.2, it was established that a waveguide taper scales the wave impedance in proportion to the ratio of the waveguide widths on either side (Equation 3.10). Therefore, a tapered zero-index waveguide can induce a reflection due to impedance mismatch. Alternatively, the correct taper ratio can achieve efficient tunneling between two materials with mismatched intrinsic impedance (Figure 3.3). In the case of the ZOR, the tunneling through the channel is maximized when the impedance of the zero-index medium is matched to the taper ratio. As this effect is due to impedance matching rather than a Fabry-Perot resonance, there is no feedback within the waveguide, so the transmission is independent of the length of the channel.

Based on this impedance-matching mechanism, the ZOR provides high transmission efficiency through any tapered waveguide as long as the intrinsic impedance of the waveguide material is matched to the geometry. As this effect is insensitive to the refractive index, the resonance will always include zero index where $\epsilon = \mu = 0$. Similarly, zero-index materials can achieve efficient coupling regardless of the waveguide geometry. For example, the waveguide shown in Figure 3.8a consists of two tapers, each scaling the wave impedance in proportion to the taper ratio. As long as the taper ratio is equivalent for both tapers, the wave impedance on either side of the waveguide is unaffected, allowing efficient power transmission. The only requirement is that the index is zero, and that the waveguide has equal width at both facets [24].

Similar reasoning applies to waveguides with multiple cascaded tapers, as in Figure

3.4. Although the wave impedance is scaled after each taper, the overall change only depends on the width of the waveguide at the facets. Sharp bends that don't change the waveguide width can have no effect on the wave impedance, and therefore do not hinder the transmission in the zero-index limit. Thus, zero-index waveguides can provide high transmission which is independent of the waveguide geometry, provided the facets equally sized. We demonstrate this effect using numerical simulation of waves propagation through a contorted waveguide filled with a zero-index metamaterial (Figure 3.9a). The waveguide exhibits high transmission due to the ZOR, despite the multiple sharp bends and the metamaterial's intrinsic impedance $Z_{\text{int}} = 1.6$.

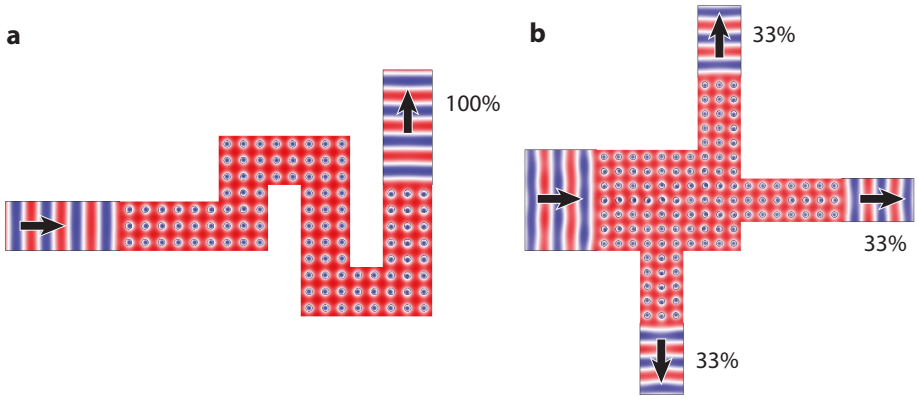

Figure 3.9: Supercoupling in arbitrary zero-index waveguides. a) Electric field in a metamaterial waveguide, operating at $\lambda = 1550$ nm and $n_{\text{eff}} = 0$. The waveguide achieves high transmission efficiency despite multiple 90° bends. b) Power splitting in zero-index waveguides. The input wave (left) is evenly split among three output ports when the total size of the input and output facets is equal.

The zero-index mode also provides a straightforward way to divide optical signals among multiple output ports, simply by controlling the width of each port. Figure 3.9b shows a three-way power splitter, where the energy couples equally to all three ports. In this example, the optimal design that minimizes the reflection is achieved when the total

area of the output facets is nearly equal to the area of the input facet[5]. The coupling to each port is independent of its placement or orientation within the waveguide, much like the flow of electrical current in a wire.

3.5 Broadband Tunneling

The zero-order resonance represents efficient power transfer through a range of optical materials in a tapered waveguide, defined by a straight line through the origin of the optical parameter space (Figure 3.8c). Efficient power transfer is restricted to materials whose impedance is matched to the waveguide taper. We are therefore free to adjust the slope of the resonance line by selecting a different taper ratio. Figure 3.10 shows the tunneling efficiency through waveguides with a variety of taper ratios. In these simulations, the waveguide is too short to support Fabry-Perot resonances, leaving only the ZOR. As before, the resonance follows a line through the origin, where the slope is equal to the taper ratio $\frac{a_2}{a_1}$, which is indicated by a dashed line. Thus, the taper can be tuned to match an arbitrary impedance, maintaining high transmission even for variable index. This effect is well suited to zero-index metamaterials, which are highly dispersive, but maintain a constant impedance across a broad range of wavelengths. By tuning the taper ratio to match the intrinsic impedance of the metamaterial, we may achieve efficient broadband transmission through the zero-index waveguide.

Figure 3.11a shows the ZOR for a tapered waveguide that is matched to the metamaterial impedance, with a taper ratio of 10:6. The waveguide is 15.5-μm-long and 8.5-μm-wide, as shown in the inset. The ZOR follows a straight line through the origin when the index is near zero, which is determined by the taper ratio. For comparison, the dashed line indicates

[5]In practice, the optimum seems to occur when the total width between between the pillars is matched. For example, this design has a 6-pillar-wide input that couples to 2-pillar-wide outputs. This discrepancy may be due to the discrete nature of the metamaterial.

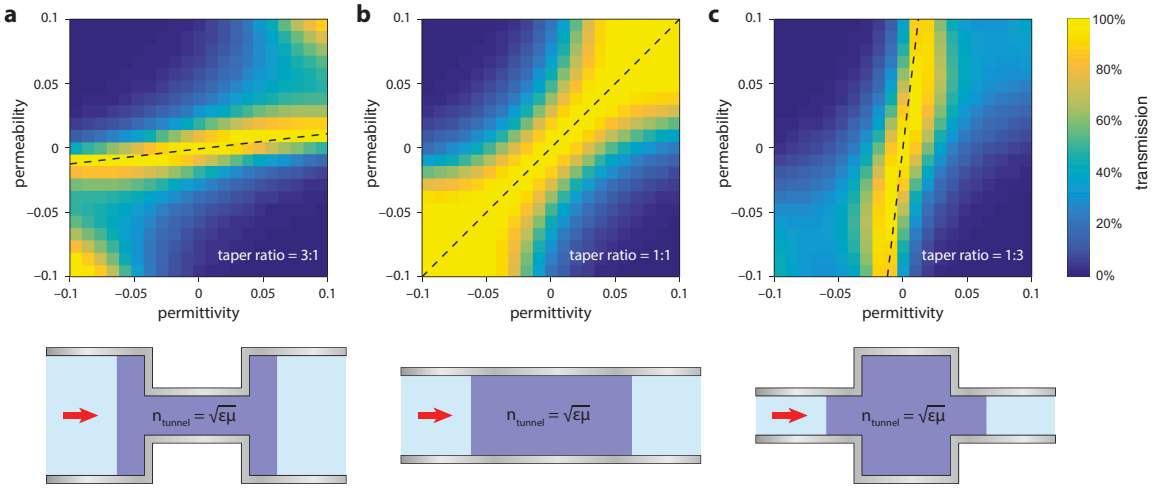

Figure 3.10: Tuning the zero-order resonance via waveguide geometry. a) Power transmission through a 6 μm tunnel filled with a homogeneous dielectric of varying permittivity and permeability. The input waveguide is 7.8-μm-wide, and the tunnel is 2.6-μm-wide, as in Figure 3.8. b) Power transmission through a 5-μm-wide straight waveguide. c) Power transmission through an inverse-tapered waveguide, where the input waveguide is 2.6-μm-wide, and the tunnel is 7.8-μm-wide. The impedance matching condition predicts efficient coupling for materials with an intrinsic impedance Z_{int} equal to the taper ratio, as indicated by the dashed line (a-c).

the effective permittivity and permeability of the zero-index metamaterial in the wavelength range $\lambda = 1525$ nm – 1575 nm. Since the dispersive optical properties of the metamaterial are aligned with the ZOR, we expect efficient power transmission across this wavelength range. We calculate the power transmission through the optimized tapered waveguide near the zero-index wavelength, which maintains an efficiency greater than 90% over a wavelength range of 30 nm (Figure 3.11b). The transmission through a non-tapered waveguide is plotted along side the optimized taper. The straight waveguide achieves perfect transmission at the zero-index wavelength, but the performance is diminished at longer and shorter wavelengths due to the impedance mismatch at the boundary of the metamaterial.

We compare the transmission spectrum of the optimized taper to waveguides with different taper ratios, as shown in Figure 3.11c. The transmission window achieves the highest bandwidth when the taper is matched to the impedance of the metamaterial, as indicated by the dashed line. Narrower tapers, corresponding to a lower slope of the zero-order resonance line, sample the ZOR over a narrow range of wavelengths. Similarly, wide tapers also exhibit high transmission over a narrow bandwidth, due to an excessively steep slope of the ZOR. Thus, we can optimize the operational bandwidth of a metamaterial waveguide by designing its dimensions in accordance with the intrinsic impedance.

The effective impedance is a fixed property of the ZIM design, determined by its constituent materials, and therefore represents a significant obstacle for zero-index devices. Since the impedance is greater than unity, it cannot be easily matched by embedding the metamaterial in a dielectric [55]. Instead, the impedance mismatch is eliminated by engineering the waveguide, allowing access to broadband applications of zero-index metamaterials such as phase-mismatch-free nonlinear optics [48].

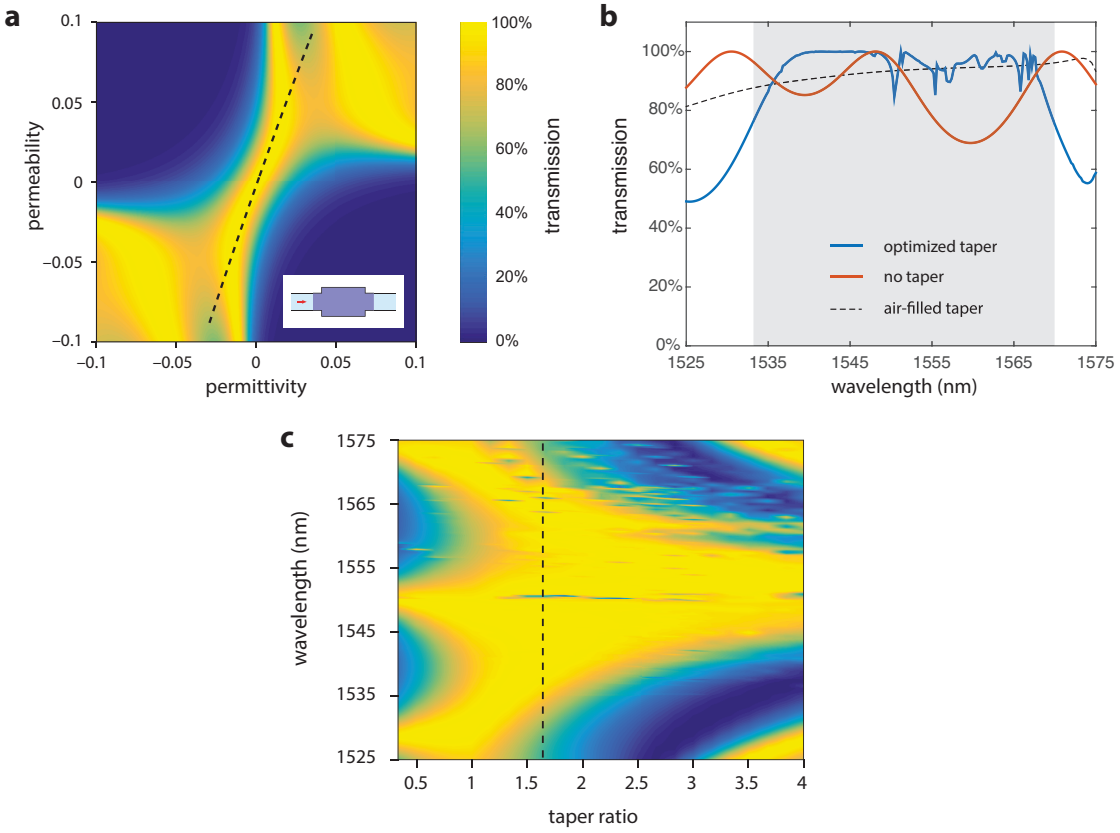

Figure 3.11: Broadband propagation in zero-index tapered waveguides. a) Power transmission through an inverse-tapered waveguide, whose dimensions are matched to the intrinsic impedance of the zero-index metamaterial. The waveguide profile is shown in the inset. The dashed line indicates the effective permittivity and permeability of the metamaterial in the wavelength range λ = 1525 nm – 1575 nm. b) Transmission spectrum for the optimized metamaterial waveguide, which maintains high efficiency across a wide bandwidth (grey region). We also show the transmission through an untapered waveguide (red), as well as a tapered waveguide filled with air. c) Transmission spectra for metamaterial waveguides with different taper ratios. The optimized ratio for impedance matching is indicated by the dashed line.

3.6 Limitations of Supercoupling

The remarkable properties of low-index waveguides are the result of single-mode operation, where the effective wavelength is much larger than the width of the waveguide. In this regime, the dynamics can be described entirely in terms of multiple reflections or impedance matching, which can be manipulated to achieve highly efficient transmission through a range of geometries. The scope of supercoupling phenomena is therefore restricted to the cases where this single-mode approximation is appropriate. By examining the conditions under which this condition is violated, we can establish design rules to ensure efficient operation of zero-index waveguides, and understand the limitations of supercoupling devices.

The single mode condition relies on three assumptions: first, only the TEM mode is allowed to propagate in the waveguide; second, only propagating modes may contribute to the transmitted signal; finally, the waveguide modes only couple to plane waves at the output. The performance of the supercoupler is compromised if any assumption is violated, so we may consider them individually to establish different limits on the potential waveguide geometries.

By operating near zero index, we ensure that all TE and TM modes are cut off in the waveguide, leaving only the TEM mode to propagate. The cutoff condition occurs when the effective wavelength in the metamaterial is more than twice the width of the waveguide. At zero index the wavelength is infinitely long, so that an arbitrarily large waveguide can maintain single-mode operation. More generally, the effective wavelength is large but finite for waveguides with a finite index. Therefore, the waveguide index establishes a maximum waveguide width, $a_{\max} = \frac{\pi}{\omega n}$, beyond which there can be multiple propagating modes.

Even when all high-order modes are cut off, they still exist as evanescent modes of the waveguide, and may influence the transmission via evanescent coupling. These evanescent

modes are necessary in order to satisfy the boundary conditions between waveguide junctions (e.g. tapers, bends), but they remain bound to the interface due to an imaginary propagation constant. However, an evanescent wave may couple to a nearby waveguide, provided the interface is not farther than the decay length of the bound mode. This decay length is determined by the imaginary propagation constant, and is non-zero even for zero-index waveguides. This provides an additional loss channel, which is not accounted for in the single-mode model of supercoupling. The effect of evanescent coupling depends on the strength of the excited evanescent mode, which varies depending on the waveguide junction. Generally, a more severe dislocation will require a greater proportion of evanescent modes in order to match the fields across the interface. Thus, evanescent coupling establishes limits on both the minimum distance between interfaces and the maximum taper ratio in supercouplers.

Finally, the coupling efficiency through metamaterial waveguides depends on the homogenization of the metamaterial at the interface with free space. For a homogeneous medium, the TEM mode in the input or output waveguide couples exclusively to the TEM mode within the zero-index medium. Due to the discrete nature of the metamaterial, however, this guided wave may couple to additional modes in the output via diffraction. This occurs when the effective wavelength in the output medium is larger than the periodicity of the metamaterial, which establishes an upper bound on the refractive index in waveguides that couple to zero-index metamaterials. For the pillar based ZIM, the maximum index is $n_{\max} = 1.8$.

Although these three criteria apply to any waveguide, regardless of the background index, but they illustrate the extent to which zero-index waveguides are useful. The maximum dimensions of the waveguide are inversely proportional to the refractive index, so we can achieve controlled power transfer through extremely large areas. This is also the regime

where zero-index phenomena are most useful— where the extreme spatial coherence gives rise to phase-free propagation over macroscopic distances [61, 62].

3.7 Conclusion

Optical waveguides provide a platform to control the flow of light, where the guided modes are determined by the waveguide geometry as well as the constituent materials. When propagating through zero-index media, these guided waves adopt an infinite wavelength, resulting in a single propagating mode that is independent of the waveguide geometry. Thus, zero-index waveguides exhibit remarkable robustness to arbitrary bends and tapers, which would otherwise cause strong reflections in positive index waveguides. Furthermore, the simplified propagation that occurs in low index waveguides ensures that they can be easily optimized for resonant tunneling, even when the index is non-zero. We have developed an accurate and intuitive model based on transfer matrix methods, which applies equally to homogeneous media and zero-index metamaterials. This model is used to design a range of devices for coupling, power splitting, impedance matching, and invisibilty.

Chapter 4

Integrated Zero-Index Metamaterials

4.1 Introduction

Metamaterials — composite materials whose electromagnetic properties are engineered by structuring their constituents [29,63]—make it possible to achieve a refractive index equal to zero [44]. When the index of refraction is zero, the phase velocity is infinite. In this extreme limit, the wavelength inside the material is infinite and the phase is uniform throughout, regardless of its overall size and shape. All fields within the material oscillate in unison, achieving electrostatic behavior at optical frequencies [49]. This regime allows access to a wealth of exciting physical phenomena and potential applications including super-coupling, cloaking, and new approaches for phase-matching in nonlinear optics [23, 44–48].

Experimental demonstrations of zero-index metamaterials typically involve metals operating around their plasma frequencies [64–66] or metallic resonators [1, 2, 67, 68], resulting in high loss and impedance mismatch. Recently, zero index was demonstrated by tuning the Mie resonances in a purely dielectric photonic crystal structure [69, 70]. This approach offers several important advantages. First, dielectric metamaterials avoid the losses associated with metals, especially in the optical regime. Second, tuning the Mie resonances allows for

the simultaneous control of the electric and magnetic response [71, 72]. In particular, when the effective relative permittivity ϵ_{eff} and permeability μ_{eff} approach zero simultaneously, the impedance $Z_{\text{eff}} = \sqrt{\frac{\mu_{\text{eff}}}{\epsilon_{\text{eff}}}}$ can be matched to that of other materials.

For integrated photonic applications, zero-index metamaterials require light to be confined on-chip and thus need to be realized in an in-plane geometry (that is, with the light propagating parallel to the substrate). This geometry would permit integrating these metamaterials with other optical elements, including waveguides, resonators, and interferometers. To date, zero-index metamaterials have been demonstrated only in an out-of-plane geometry, with functional layers of the metamaterials stacked on a substrate and where light propagates normal to the sample surface [2, 66, 70]. This geometry is not only impractical for integrated-photonics applications, but is also limited to short interaction lengths, and cannot be fabricated in arbitrary shapes.

In this chapter, we present an on-chip, in-plane metamaterial with zero index in the telecom wavelength range. Our design consists of a square array of low-aspect-ratio silicon pillars on a silicon-on-insulator (SOI) substrate. The array is embedded in an SU-8 slab waveguide, and clad above and below by gold films. We fabricate this metamaterial using conventional nanofabrication processes (Figure 4.1). First, we define an array of pillars in a 512-nm-thick silicon device layer using electron-beam lithography followed by inductively coupled plasma reactive ion etching (step I). Next, we use electron-beam evaporation to deposit a 50-nm-thick gold film (step II). We then embed the pillars within a 595-nm-thick SU-8 photoresist layer (step III). Finally, a second gold film is deposited to complete the fabrication process (step IV). We can produce arbitrarily shaped pillar arrays using such conventional planar fabrication techniques in order to realize a variety of metamaterial devices.

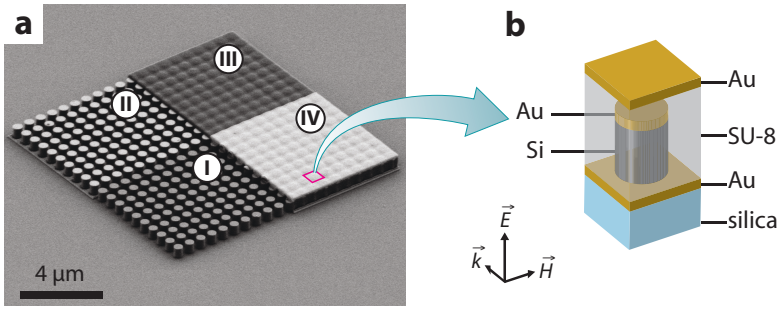

Figure 4.1: Metamaterial design and structure fabricated to demonstrate in-plane zero index. a) SEM image of the metamaterial in different fabrication stages: I. Silicon pillars etched from SOI substrate; II. With bottom gold film; III. Embedded in SU-8 matrix; IV. Completed structure with top gold film. b) Three-dimensional schematic of one unit-cell of the metamaterial. The pitch and radius of the silicon pillars are 690 nm and 211 nm, respectively.

4.2 Design

Previous designs for dielectric zero-index metamaterials are based on infinitely long silicon pillars [69, 70]. These designs are incompatible with integrated silicon photonic platforms, which are typically based on silicon device layers with thickness on the order of the wavelength. One can replicate the behavior of infinitely long pillars by placing short silicon pillars between parallel conductors [73]. This approach reduces the out-of-plane radiative loss and enforces transverse magnetic (TM) polarization of the guided mode, as tangential fields are damped at the surface of the conductor (Appendix D). The effect is analogous to the method of image charges, where the modes of the metal-clad pillar array approximate an infinite series of reflected pillars. Thus, we can emulate the impedance-matched zero-index modes found in infinite pillar arrays using a structure of finite height, allowing the metamaterial to be integrated with conventional nanophotonic components.

In order to ensure efficient propagation through the metamaterial, the effective permittivity and permeability must both be tuned to zero at the operating wavelength. These conditions are satisfied by adjusting the pitch and radius of the silicon pillar array, follow-

ing the procedure outlined in Section 5.2. The metamaterial is optimized for a zero-index wavelength of 1590 nm, near the middle of the tuning range of our laser. We use an analytical model for the effective constitutive parameters of a square array of 2D dielectric cylinders [74] to calculate the approximate dimensions of the pillar array. Based on this initial design and the height of the silicon pillars, the SU-8 layer thickness, and the gold layer thickness, we perturb the pitch (a) and radius (r) to achieve an effective index equal to zero for the 3D metamaterial design.

We evaluate the effective index n_{eff} using complex parameter retrieval combined with 3D FDTD simulations [34]. The metamaterial is modeled as an effective medium with complex index and impedance (Figure 4.2a). We simulate the reflection and transmission through a metamaterial slab of finite thickness, and use the measured complex scattering coefficients to determine the real and imaginary effective index of the metamaterial. This analysis is sensitive to both the sign and magnitude of the effective permittivity and permeability: when both permittivity and permeability are positive (or negative) the effective index is real, $n_{\text{eff}} = \sqrt{\epsilon_{\text{eff}}\mu_{\text{eff}}}$. Similarly, when permittivity and permeability have opposite sign, the effective index is imaginary. However, if the permittivity and/or permeability reaches zero, then both the real and imaginary components of the effective index will vanish. Therefore, the absolute value of the effective index is a suitable figure of merit for impedance-matched zero-index behavior. In the presence of dissipative materials, such as the gold layers, the imaginary index will never reach exactly zero due to residual absorption. In this case, the absolute index reaches a minimum when the real index equals zero and the propagation loss minimized. Figure 4.2b shows the retrieved value of the absolute index at 1590 nm for a range of metamaterial designs near the initial design from effective medium theory. The pitch and radius range from 640 nm - 760 nm and 190 nm - 230 nm, respectively, approximately $\pm 10\%$ for each. The absolute index is minimized for $a = 690$ nm

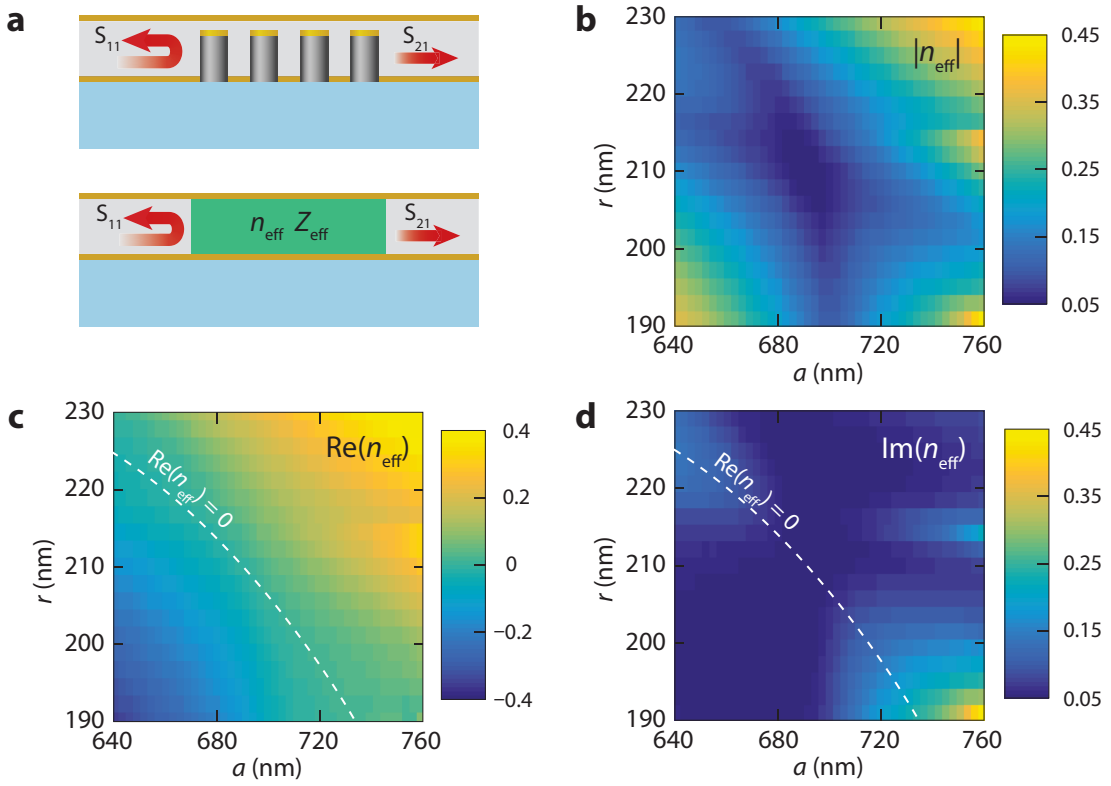

Figure 4.2: Effective index of the Dirac-cone metamaterial as a function of pitch and radius at the design wavelength $\lambda = 1590$. (a) The metamaterial is equivalent to an effective medium with complex index and impedance. We invert the simulated reflectance and transmittance spectra to retrieve these effective paramters. (b) Magnitude of the effective index for for metamaterials with various pitch and radius. The value is minimized at $a = 690$ nm, $r = 211$ nm. (c) Real part of the effective index. The dashed line indicates a set of designs with zero effective index. d) Imaginary part of the effective index. The dashed line follows the same contour as part (c).

and $r = 211$ nm near the center of the parameter space, where $n_{\text{eff}} = 0.002 + i0.046$. The real index (Figure 4.2c) is near zero across a wide region of the parameter space, roughly following the diagonal from low-radius/high-pitch to high-radius/low-pitch. However, this region corresponds to a non-zero imaginary index (Figure 4.2d). This behavior is similar to the complex index of infinite pillar arrays (Section 5.2), where regions of imaginary index correspond to photonic bandgaps. The optimized design therefore signals the formation of a photonic Dirac cone, where the index approaches zero without forming a bandgap.

4.3 Band structure and Homogenization

To characterize the optical modes of the designed metamaterial, we calculate its band structure in the plane of the array (Figure 4.3a). The pillar array supports two bands with linear dispersion, which intersect at the Γ-point. These bands form a Dirac-like cone (blue) intersecting a quadratic dispersion band (red) at the Dirac point at the center of the Brillouin zone [69]. The two linear-dispersion bands correspond to electric monopole and transverse magnetic dipole modes near the Dirac point (Figure 4.3b). At the Dirac point, the wavenumber approaches zero, indicating that the effective index of the metamaterial is also zero. Furthermore, the nearly circular isofrequency contours in a 55-nm bandwidth around the Dirac point (Figure 4.3c) suggest that the metamaterial is essentially isotropic, producing a refractive index of zero in all propagation directions. The effective wavelength λ_{eff} approaches infinity in the vicinity of the Γ-point, satisfying the homogenization criterion [37, 69, 70] and allowing us to treat the metamaterial as a homogeneous bulk medium with effective constitutive parameters in the vicinity of the Dirac point. We can retrieve the effective permittivity ϵ_{eff} and permeability μ_{eff} of the metamaterial from the simulated reflection and transmission coefficients (Figure 4.3d) [34]. The computed ϵ_{eff} and μ_{eff} cross

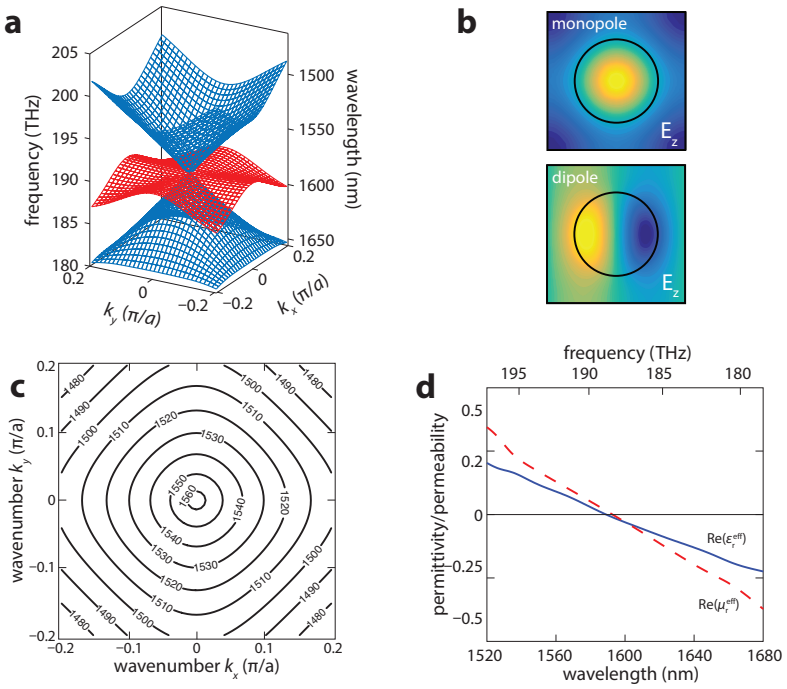

Figure 4.3: Optical properties of the zero-index metamaterial. a) Photonic band structure of the zero-index metamaterial for TM modes near the Γ-point. Two bands with linear dispersion (blue) intersect to form a Dirac-like cone. The quadratic band (red) is a quasi-longitudinal mode [cite]. We show only the three modes that form the cone to emphasize the Dirac-cone dispersion clearly. b) Electric fields at the Dirac point over a unit-cell cross-section in the plane of the array, corresponding to an electric monopole mode and a transverse magnetic dipole mode. The black circles indicate the boundary of the silicon pillar. c) Isofrequency contours of the zero-index metamaterial. The nearly circular contours indicate that this metamaterial is isotropic near the Γ-point. d) Effective permittivity and permeability of the metamaterial retrieved from simulated reflection and transmission coefficients. Both parameters cross zero simultaneously resulting in finite impedance.

zero simultaneously and linearly at the design wavelength of 1590 nm, with an effective impedance of 1.47. This simultaneous electric and magnetic response is characteristic of zero-index metamaterials corresponding to Dirac cones, and is essential to achieve a finite impedance [69]. The dispersion of ϵ_{eff} and μ_{eff} is linear in the vicinity of the Dirac-point wavelength [69], as required by causality for zero-index media (Appendix C).

4.4 Fabrication Considerations

Based on this process outlined in Figure 4.1, we can fabricate on-chip metamaterials with arbitrary size and shape. When coupled with integrated silicon photonics, these arrays allow access to zero-index phenomena including supercoupling [23] and phase-free nonlinear optics [48]. However, the performance of these devices will depend on the accuracy of fabrication, which is subject to statistical deviation from the optimized design.

Since the existence of a Dirac cone is sensitive to the geometric parameters of the structure, it is important to investigate the robustness of our design with regards to the effects induced by parameter variations. Here, we study the effects of variations in the pillar radius since this parameter represents the largest source of disorder among all the geometric parameters. We model the effect of disorder on the transmission through the structure assuming a Gaussian distribution with a mean radius $r = 211$ nm and standard deviation Δr (Figure 4.4). Using 3D FDTD simulations, we compute the transmission through a metamaterial slab with 8 unit cells in the direction of propagation. The transmission at the zero-index wavelength, 1590 nm, is greater than 10% at the design 1590 nm as long as the disorder $\Delta r/r$ is less than 6%, which is achievable using standard electron-beam lithography.

The zero-index behavior is also sensitive to the thickness of the SU-8 background, which controls the separation between the silicon pillars and the top gold layer. SU-8 is

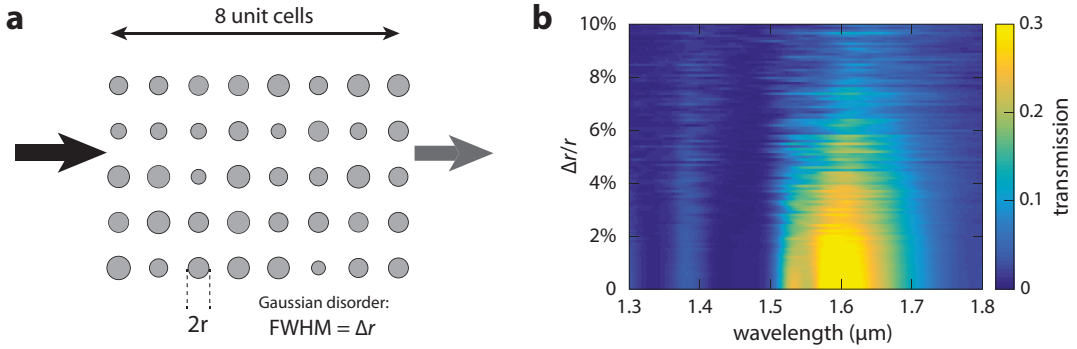

Figure 4.4: Effect of disorder in pillar radius on transmission through a metamaterial slab. a) We model the transmission through 8 unit cells where the radius is normally distributed with a mean of $r = 211$ nm and variance Δr. b) Transmission through the disordered metamaterial as a function of variance.

deposited via spin coating, which is highly repeatable, but is not optimized for non-planar substrates. As a result the viscous SU-8 may interact with the silicon pillar array and form a non-uniform coating (for example Figure 4.1a, section III). This effect can be mitigated by depositing thicker layers of SU-8, such that the thickness is much greater than the height of the pillars. In order to justify this design change, we use finite element analysis to examine the effect of SU-8 thickness on the photonic band structure. Figure 4.5a shows the modal wavelengths for the monopole and dipole modes at the Γ-point for a range of different SU-8 thicknesses. The eigenfrequencies show strong dependence on the SU-8 thickness, especially for the dipole mode. This is due to the symmetry of the dipole, which couples to a Fabry-Perot cavity created between the gold layers [75]. Despite their strong dispersion, the monopole and dipole modes are degenerate for a discrete set of SU-8 thicknesses: $t_{\text{SU-8}} =$ 550 nm, 975 nm, 1475 nm, 1975 nm. These intervals correspond to half-wavelengths in the SU-8, which match the resonances of the Fabry-Perot cavity. At these thicknesses, the degenerate monopole and dipole modes form a Dirac cone at the center of the Brillouin zone (Figure 4.5b), resulting in an effective index equal to zero. Thus, zero-index behavior can

be obtained even for significantly larger SU-8 layer thicknesses, providing more flexibility in the fabrication process. In order to avoid the film irregularities associated with thin SU-8, we use a 1.5-um-thick SU-8 layer in the experimental demonstration of integrated zero-index metamaterials.

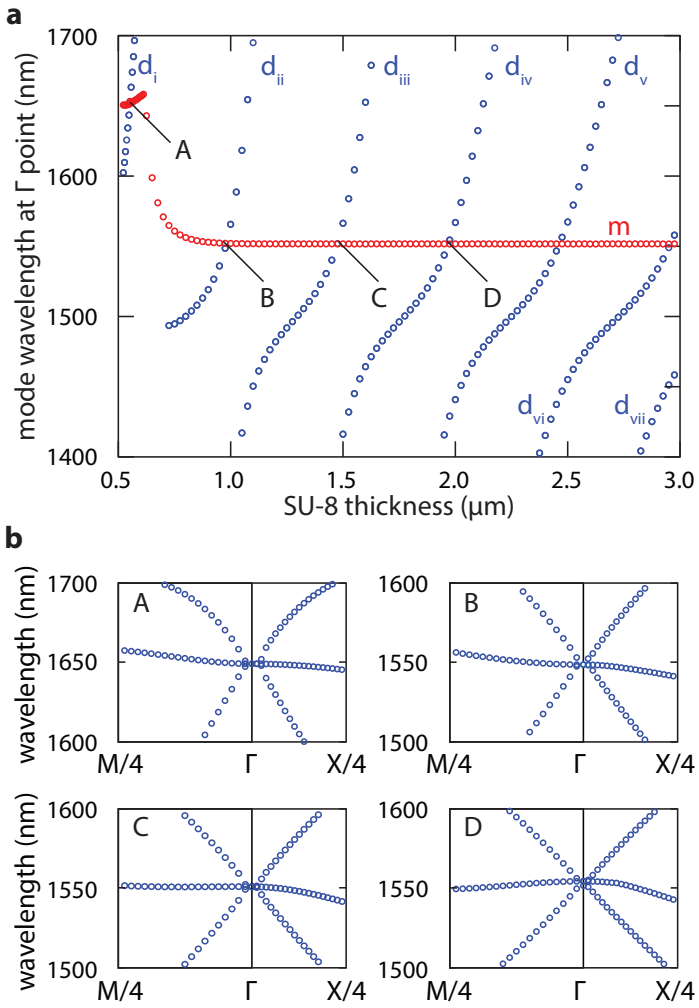

Figure 4.5: Effect of variation in SU-8 thickness on modes forming the Dirac cone. a) Wavelengths of the electric monopole mode (red) and the transverse magnetic dipole modes (blue) at the Γ-point for various SU-8 thicknesses. b) Band structures corresponding to the four intersections (A, B, C, D) of the electric monopole and magnetic dipole modes in (a).

Finally, the overall size of metamaterial devices is limited by the propagation loss in

the metamaterial, which is dominated by Ohmic loss in the gold films. We estimate both the coupling and propagation losses of the metamaterial using FDTD simulations. Figure 4.6a shows a metamaterial slab of finite width, adjacent to a pair of 500-nm-thick silicon slab waveguides. The metamaterial and waveguides are assumed to be infinite in the transverse direction. The fundamental TM mode is launched in the input slab waveguide and the transmission is monitored in the output waveguide. By measuring the transmission through the metamaterial as a function of its width, we are able to extract the propagation and coupling loss (Figure 4.6b). On a semi-logarithmic scale, the transmission (dB) closely follows a linear trend, which corresponds to a propagation loss of 0.9 dB/unit cell (1.3dB/um). The linear fit indicates a loss of –2.8 dB for when the metamaterial equals zero, which corresponds to the input and output coupling losses at the interface with the waveguides. The coupling loss at a single interface is 1.4 dB (28%). The coupling loss can be reduced by using a different input waveguide geometry, such as a photonic-crystal-waveguide taper [76].

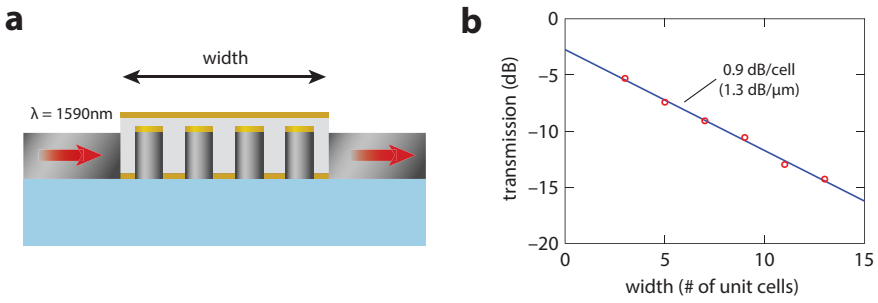

Figure 4.6: Coupling and propagation loss. a) Metamaterial slab of finite width illuminated by a 500-nm-tall silicon slab waveguide. b) Transmission through the metamaterial as function of propagation distance. The slope of the line corresponds to the propagation loss; the residual loss at zero propagation distance corresponds to twice the coupling loss between the metamaterial and the integrated silicon waveguide.

4.5 Experimental Results

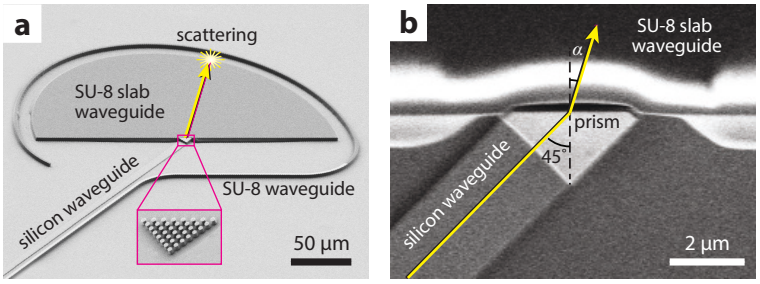

Figure 4.7: Integrated metamaterial prism. a) A silicon waveguide carries the incident beam toward the metamaterial prism, where the beam is refracted into the SU-8 slab waveguide. Inset shows the prism, which is a right triangular array of pillars measuring 8 unit cells across, without gold and SU-8 layers. b) Prism region showing the incident and refracted beams. The angle of refraction α is determined by measuring the position of the refracted beam at the curved output edge of SU-8 slab waveguide (yellow scattering spot in (a)).

We experimentally demonstrate zero index by measuring refraction through a prism made of this metamaterial (Figure 4.7). The prism consists of 36 silicon pillars (8×8) arranged to form a right-triangular array. We fabricate the prism along side an integrated silicon waveguide, oriented perpendicular to one of the prism facets, which illuminates the prism with TM-polarized light. Light propagates through the prism with an effective index n_{eff}, and reaches the interface between the prism and a SU-8 slab waveguide at an angle of incidence of 45°. The refracted beam then propagates as a guided mode of the SU-8 slab waveguide with known effective index $n_{\text{SU-8}} \approx 1.5$, until it is scattered at the semi-circular edge of SU-8 slab waveguide. The scattered light is imaged from above using an infrared camera to measure the refraction angle α. This refraction angle is used to determine n_{eff} using Snell's law:

$$n_{\text{eff}} = n_{\text{SU-8}} \frac{\sin \alpha}{\sin 45^\circ} \tag{4.1}$$

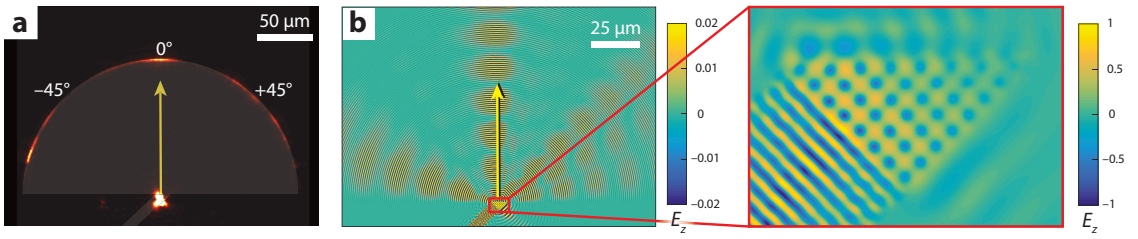

Figure 4.8: Simulation and experimental results. a) Near-infrared microscope image of the prism at 1570 nm showing the refracted beam, which propagates normal to the interface between prism and SU-8 slab waveguide. The gray area corresponds to the silicon waveguide and SU-8 slab waveguide. b) Left: simulated out-of-plane electric field (E_z) in the prism and SU-8 slab waveguide region. The refracted beam is visible at the curved output edge of SU-8 slab waveguide at 0°. Right: magnified view of electric field distribution in the prism, illustrating nearly constant spatial phase distribution.

Figure 4.8a shows the experimentally observed refraction in the prism and the SU-8 slab waveguide at $\lambda = 1570$ nm, where the metamaterial shows zero index. Because of fabrication imperfections, this wavelength is slightly different from the design wavelength of 1590 nm. The yellow arrow in Figure 4.8a indicates the direction of the refracted beam, which propagates perpendicular to the interface between the prism and SU-8 slab waveguide, corresponding to a prism with a refractive index of zero. The prism also generates several side beams at 1570 nm due to additional modes in the band structure.

Figure 4.8b shows the corresponding numerical calculation of the out-of-plane electromagnetic field distribution in the prism and the SU-8 slab waveguide region at $\lambda = 1570$ nm. As in the observed results, the refracted beam propagates perpendicular to the interface between the prism and SU-8 slab waveguide, with several side beams appearing on either side. As shown in the magnified view on the right in Figure 4.8, there is no spatial phase variation within the prism, as the effective wavelength is infinite inside the metamaterial.

We probe the dispersion of the metamaterial index by measuring the angle of refraction while varying the input wavelength from 1480 to 1680 nm. Figure 4.9a shows the

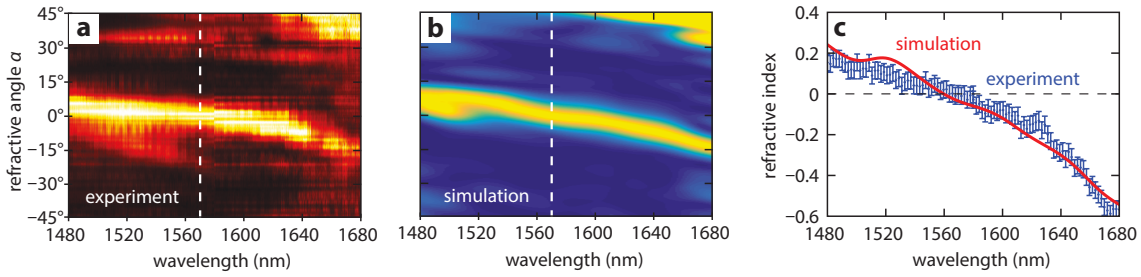

Figure 4.9: Extracted index spectrum. a) measured and b) simulated refraction at different wavelengths. The white dashed line indicates the wavelength, 1570 nm, at which the refracted beam crosses 0°. The image is normalized at each wavelength. d, Measured and simulated effective index of the zero-index metamaterial. The blue dots indicate measured refractive index, with error bars representing uncertainties in the measurement. The red line indicates the corresponding simulated index.

intensity measured along the curved output edge of the SU-8 slab waveguide as a function of wavelength and refraction angle. Figure 4.9b shows the corresponding simulated far-field pattern. We observe excellent agreement between the measured and simulated far-field patterns, with both patterns showing the refracted beam in the center, near 0°. The steady shift of the refracted beam with increasing wavelength indicates that the refractive index of the prism continuously changes from a positive value at shorter wavelengths to a negative value at longer wavelengths.

Using Snell's law, we extract the index of refraction of the metamaterial from the position of the refracted beam in the wavelength range of 1480-1680 nm (Appendix E). As shown in Figure 4.9c, the measured index varies from 0.15 ± 0.04 at 1480 nm to -0.57 ± 0.04 at 1680 nm, exhibiting linear dispersion near the zero crossing at 1570 nm. The error bars represent uncertainties in the measured index due to finite image resolution and fitting uncertainty. Using a similar extraction method, we calculate the index of refraction from the simulated far-field patterns, showing excellent agreement with measured values.

To verify that the measured zero index is due to the existence of a Dirac cone, we simulate and fabricate an additional prism with pillar radii that are larger than that of the ideal

design. Because the Dirac cone is characterized by accidental degeneracy of the monopole and dipole modes, it will only be observed for the optimized radius; otherwise, a bandgap appears monopole and dipole modes. From an effective medium perspective, changing the pillar radius breaks the degeneracy of the magnetic and electric plasma frequencies, resulting in a frequency range in which either the effective permittivity or effective permeability is negative, but not both. In this case, the real part of the index is fixed at zero over a range of wavelengths between the positive and negative index regimes, indicating a bandgap.

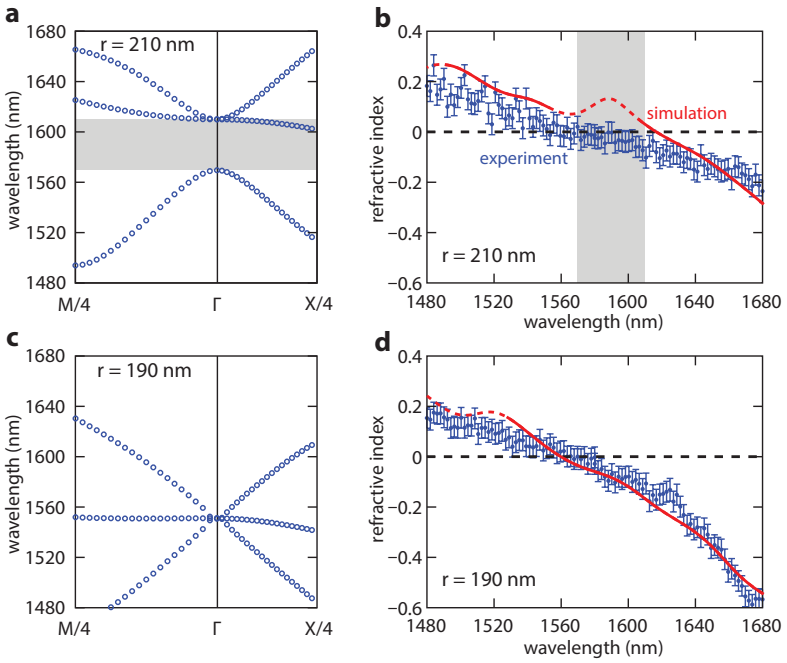

Figure 4.10: Effect of different pillar radii on photonic band (a, c): Band structures of metamaterials with pillar radii 210.5 nm and 190 nm, respectively. (b, d): Effective indices extracted from measured and simulated refraction through prisms with $r = 210.5$ nm and 190 nm, respectively. Simulations are shown by red curves, and measured results are shown by blue dots with error bars. The grey bar indicates the bandgap region, as predicted by the band structure.

Figure 4.10a shows the band structure for a metamaterial prism with $r = 210$ nm, approximately 10% larger than the optimized design. The dipole modes at the Γ-point that are redshifted away from the monopole, opening a bandgap in the wavelength range between

1570 nm and 1610 nm. This effect is verified by the measured and simulated n_{eff} shown in Figure 4.10b: the zero crossing of the index is redshifted, and the measured index remains at zero throughout the bandgap region. In simulations, the refracted beam is relatively weak for these wavelengths, resulting in relatively large fitting uncertainty within the bandgap. Here, we plot the simulated index with a dashed line when the uncertainty is larger than the average uncertainty over the entire bandwidth. For comparison, the optimized design (Figures 4.10c-d) supports degenerate dipole and monopole modes, and the measured index is characterized by linear dispersion through $n_{\text{eff}} = 0$. Given the measured uncertainty, the band gap is at most 50 nm wide, suggesting that the zero-index behavior is due to a Dirac cone at the Γ-point.

As a control, we also measured the refractive index in the absence of the metamaterial prism. In this control experiment, light from the input silicon waveguide propagates through free space before refracting into the SU-8 slab waveguide. The measured index of the void is $n = 0.94 \pm 0.04$ in the wavelength range 1480-1680 nm, in good agreement with the index of air (Appendix F). Therefore, the measured index shown in Figure 4.9c corresponds to the effective index of the metamaterial prism, rather than an artifact of the measurement setup.

4.6 Conclusion

We experimentally demonstrate the first on-chip integrated zero-index metamaterial in the optical regime and directly measure the effective index of a prism consisting of this material. The metamaterial is effectively two-dimensional (2D), as energy propagates in the plane of the array. This in-plane structure can efficiently couple to silicon waveguides to interface with standard integrated photonic components. Using standard planar processes, the metamaterial can be fabricated over a large area with high fidelity and in arbitrary shapes.

This design enables direct implementation of zero-index phenomena on a chip, including super-couplers, surface-emitting lasers, and new approaches for phase-matching in nonlinear optics [23, 44, 47, 48, 61]. It can also serve as an on-chip lab to explore fundamental quantum science such as photon entanglement and enhancement of spontaneous emission [49, 70].

Chapter 5

Lossless Zero-Index Metamaterials

All zero-index phenomena can be viewed through the lens of the effective wavelength: as the index approaches zero, waves stretch out toward infinity, and "spatial phase" loses its meaning as electric and magnetic fields fill the space uniformly. In this sense, the most dramatic applications of zero-index metamaterials will occur in large-area devices that take advantage of the extreme spatial coherence. However, existing demonstrations of integrated ZIM are only suitable for relatively small length scales, due to absorption during propagation. The absorption stems from ohmic loss in the integrated metal waveguides (Appendix D), which limits the size of metamaterial devices to tens of microns. Access to zero-index phenomena over macroscopic distances will therefore require a metamaterial design based entirely on lossless dielectrics.

We have recently demonstrated a variation on the original ZIM design that eliminates the need for metals [77]. This structure consists of a square array of silicon pillars on a silica substrate (Figure 5.1). Removing the metal waveguides causes a frequency shift in the monopole and dipole Mie resonances within the finite pillars, breaking their accidental degeneracy. However, we can restore the degeneracy by adjusting the unit cell dimensions

(radius and pitch) as before, creating an in-plane metamaterial that supports zero-index modes. Despite the lack of dissipative materials, however, this all-dielectric ZIM suffers from propagation loss comparable to the metal-based design. Here, the loss is due to out-of-plane radiation from the zero-index mode into free space.

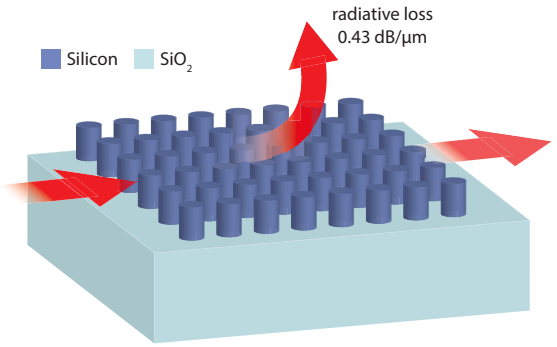

Figure 5.1: Zero-index modes are supported by finite silicon pillar arrays, even without the metal cladding. However, these modes suffer significant radiative loss during propagation.

The performance of all-dielectric ZIMs highlights a fundamental limitation for any low-index mode propagating in finite structures, especially modes with zero index. If the in-plane momentum is less than the momentum of plane waves in free space, then there exists a continuum mode that is momentum-matched to the guided mode, and light can couple out of the plane. In the context of the photonic bandstructure these "leaky" modes operate above the light line, and are always associated with radiative loss. This condition is equivalent to the critical angle for total internal reflection, such that modes above the light line are inherently unconfined to the substrate. In the case of zero-index modes, it is impossible to achieve confinement even when the surrounding medium (cladding) has an arbitrarily low index.

Rather than relying on momentum-based confinement, in this chapter we present a zero-index metamaterial design that eliminates radiative loss through destructive interfer-

ence of multiple loss channels, resulting in a bound state in the continuum [78, 79]. The design includes an in-plane reflector, creating a Fabry-Perot cavity parallel to the silicon pillar array. By adjusting the coupling between the cavity and the guided mode, we can completely quench the out-of-plane radiation, resulting in a lossless zero-index metamaterial.

5.1 Bound States in the Continuum

There are several mechanisms beyond total internal reflection that can confine electromagnetic modes to finite volumes. The simplest is to surround a guiding region with materials that do not support propagating modes, such a metals or photonic bandgap materials [51, 80, 81]. In this case, there are no continuum modes that can couple to the bound state. Alternatively, we may design structures whose resonant modes are unable to couple to continuum modes due to symmetry mismatch, such as dark state lasers [82, 83]. Finally, bound states can occur in structures which couple to multiple continuum modes, as long as the various loss channels interfere destructively [84]. Such bound states in the continuum (BiCs) were first observed in quantum mechanical systems [85], and have been extended to integrated photonics [78, 86–89]. Because the confinement does not rely on any specific modal symmetry, photonic BiCs can arise in Bloch modes operating above the light line.

In order to create a BiC in dielectric ZIM, we must identify the sources of radiative loss and arrange for them to interfere. The zero-index mode is the result of accidental degeneracy of monopole and dipole Mie resonances at the center of the Brillouin zone. The symmetry of the monopole mode prevents coupling to the continuum; however, the dipole mode is compatible with plane waves [90], which radiate from both sides of the pillar array (Figure 5.2a). Therefore we can achieve a BiC by adding a reflector above the plane of the array, which couples the two loss channels. Energy that escapes through the top surface is

reflected back toward the pillar array, where it couples back into the guided mode or into the space below.

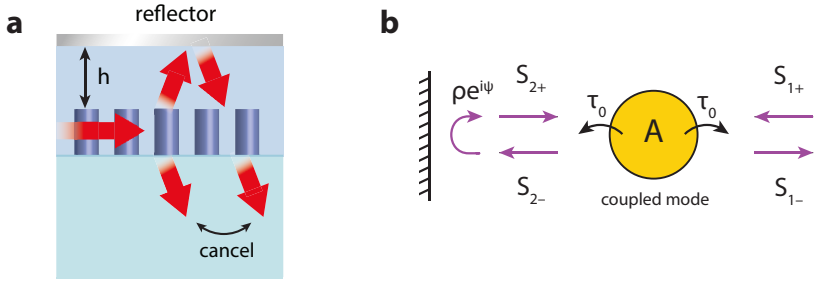

Figure 5.2: Design of lossless zero-index metamaterials. a) The all-dielectric pillar array is placed parallel to a reflective surface, at a distance h. Radiative loss is reflected back toward the array. b) This system is modeled as a damped harmonic oscillator A, with a resonant frequency ω_0 and lifetime τ_0. The bound mode is coupled to continuum modes $s_{n\pm}$. The reflector provides feedback, connecting s_{2+} and s_{2-} with an overall phase shift ψ and reflectivity ρ.

We can model this interaction using temporal coupled mode theory (tCMT) [51]. The leaky dipole mode is treated as a damped harmonic oscillator with an intrinsic decay rate τ_0, resonant frequency ω_0, and time-dependent amplitude $A(t)$ (Figure 5.2b). In the absence of the reflector, the energy stored within the dipole mode couples to the continuum, with time dependence $\frac{dA(t)}{dt} = (-i\omega_0 - \frac{1}{\tau_0})A$. By reciprocity, incoming plane waves may also couple into the dipole mode. Therefore, the time evolution of the guided mode amplitude may be modified if the pillar array is illuminated by plane waves s_{1+} and s_{2+}, and is generally described by a system of coupled equations:

$$\frac{dA(t)}{dt} = (-i\omega_0 - \frac{1}{\tau_0})A + \kappa_1 s_{1+} + \kappa_2 s_{2+} \tag{5.1}$$

$$s_{1-} = r s_{1+} + t s_{2+} + d_1 A \tag{5.2}$$

$$s_{2-} = t s_{1+} + r s_{2+} + d_2 A \tag{5.3}$$

where $s_{1\pm}$ and $s_{2\pm}$ are the continuum mode amplitudes below and above the pillar array,

respectively. The subscript sign ± denotes incoming or outgoing waves. Coefficients r and t are the direct reflection and transmission coefficients through the array, accounting for the coupling between plane waves on either side of the array. d_1 and d_2 represent the decay of the dipole mode into the continuum modes. This model assumes that the dipole and continuum modes are weakly coupled [51], such that the amplitude A decays exponentially and the contribution from continuum modes is frequency-independent (i.e., $\kappa_n \neq \kappa_n(\omega)$). The weak-coupling approximation is valid for resonators with high quality factor $Q = \frac{\omega_0 \tau_0}{2} \gg \pi$ (the dipole resonance has $Q \approx 12$). The model also ignores the presence of the monopole mode, which is decoupled from the dipole and the continuum modes by symmetry. Finally, the plane wave amplitudes above the pillar array are connected due to the presence of the reflector:

$$s_{2+} = \rho s_{2-} \mathrm{e}^{i\psi} \tag{5.4}$$

where $\psi = 2kh$ is the phase accumulated by a plane wave with wavevector k upon propagation to and from the reflector, which is placed at a distance h from the pillar array. ρ is the amplitude reflection coefficient of the reflector. For a perfect reflector, $\rho = 1$.

Equations 5.1-5.4 describe the time evolution of the bound mode in terms of the coupling coefficients with the continuum. Not all of these coefficients are independent, and can be related by time-reversal and mirror symmetries. The silicon pillars are symmetric across the plane of the array, so the out-coupling coefficients on either side must be equal or opposite, $d_1 = \pm d_2$, depending on whether the bound mode is symmetric or anti-symmetric. Because the metamaterial is constructed from non-dissipative materials, the system is also symmetric under time reversal. Therefore the incoupling and outcoupling coefficients are equal, $\kappa_n = d_n$. Without loss of generality we may normalize the amplitudes $|s_{n\pm}|^2$ to the intensity of plane waves. In this case, the various decay coefficients are all related to

the intrinsic decay of the bound mode [88, 89], $|d_n|^2 = \frac{1}{\tau_0}$, due to conservation of energy. Finally, the reflection and transmission coefficients of the pillar array are connected via Stokes relations, $r^*r + t^*t = 1$ and $r^*t + t^*r = 0$, as a consequence of time-reversal symmetry [91]. Thus, the time evolution depends on only two unknown parameters, r and $\arg(d_1)$, which can be calculated from numerical simulations of the silicon pillar array without the mirror (Appendix G).

Based on these parameters, we can use the coupled mode equations to predict the appearance of a bound state in the continuum. When there is no wave incident from below ($s_{1+} = 0$) the guided mode will form a bound state if the outgoing wave intensity disappears, such that $s_{1-} = 0$. In this case, the guided mode exchanges no energy with the continuum. Combining equations 5.1–5.4, we can show that the BiC condition is satisfied when $t + r = \rho^{-1}\mathrm{e}^{-i\psi}$. From Stokes relations, the quantity $(t + r)$ must have unit magnitude; therefore, the equality can only be satisfied by a perfect reflector $\rho = 1$. Otherwise, the loss channels cannot cancel exactly. Assuming perfect reflectivity, the BiC condition reduces to a phase-matching requirement for the round-trip propagation phase:

$$\psi = 2kh = \arg(t + r) + 2\pi n \qquad\qquad n = 0, \pm 1, \pm 2, \ldots \tag{5.5}$$

Since this phase is proportional to the separation between the pillar array and the reflector, we will always be able to design the metamaterial to support a bound state in the continuum by adjusting h. Furthermore there is an infinite series of such configurations, where the reflector separation is shifted in increments of one-half wavelength.

We demonstrate this effect by simulating the Bloch modes of the pillar array with an adjacent perfect reflector. The radiative loss is characterized by the quality factor $Q = \frac{\omega_0\tau_0}{2}$, which is proportional to the resonant lifetime. Figure 5.3a shows the Q factor for

both the monopole and dipole modes at various reflector separations h. The monopole mode maintains a high quality factor ($Q \approx 10^5$) regardless of the separation, because of its symmetry mismatch with continuum modes. The finite lifetime is due to a small amount of residual dissipation in the silicon material model, which is based on experimentally measured optical properties. By contrast, the Q factor of the dipole mode is strongly dependent on the reflector separation, indicating coupling with continuum modes between the pillar array and the reflector. The resonant lifetime is maximized for a separation of $h = 457$ nm, achieving confinement comparable to the monopole mode.

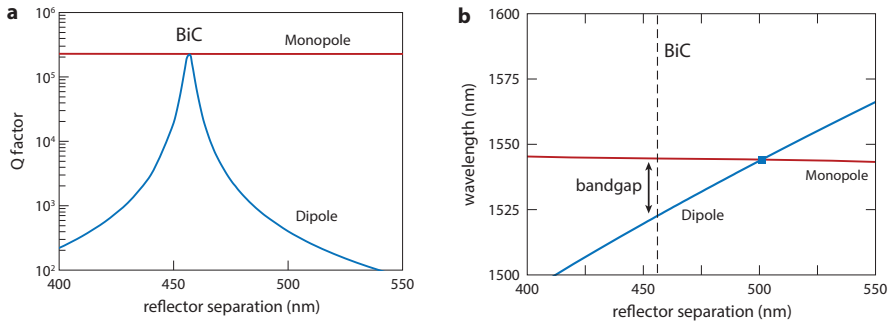

Figure 5.3: Radiative loss and degeneracy in BiC ZIM. a) Radiative Q factor of the dipole and monopole modes for different reflector separations. The monopole mode does not radiate due to symmetry protection [90], but exhibits a finite lifetime due to residual material absorption. The dipole mode achieves the same Q factor as the monopole for a separation $h = 457$ nm. b) Resonant wavelengths of the monopole and dipole modes at the Γ-point for the same range of reflector separations. The modes are degenerate when $h = 500$ nm, but not for the separation that generates a BiC (dashed line).

5.2 Bound States at the Dirac Point

By tuning the separation between the pillar array and reflector, we can achieve perfect confinement of the dipole mode. However, the reflector separation also affects the resonant frequency (Figure 5.3b), as predicted by tCMT. When the pillar array is not illuminated

from free space, the amplitude of the bound mode evolves according to

$$\frac{dA(t)}{dt} = (-i\omega_0 - \frac{1}{\tau_0})A - \frac{d_1^2}{r - \rho^{-1}\mathrm{e}^{i\psi}}A \tag{5.6}$$

$$\equiv (-i\omega_{\mathrm{eff}} - \frac{1}{\tau_{\mathrm{eff}}})A \tag{5.7}$$

where the coupled mode has an effective frequency ω_{eff} and effective decay rate τ_{eff}

$$\omega_{\mathrm{eff}} = \omega_0 + \mathrm{Im}\left[\frac{d_1^2}{r - \rho^{-1}\mathrm{e}^{i\psi}}\right] \tag{5.8}$$

$$\frac{1}{\tau_{\mathrm{eff}}} = \frac{1}{\tau_0} + \mathrm{Re}\left[\frac{d_1^2}{r - \rho^{-1}\mathrm{e}^{i\psi}}\right] \tag{5.9}$$

Therefore, the reflector separation simultaneously affects the confinement and frequency of the dipole mode. The monopole mode, which does not couple with the continuum, maintains a constant resonant frequency. In order to support zero-index propagation, the monopole and dipole modes must be degenerate, which can only be achieved for a particular separation. This may occur at a different separation than the bound state. Lossless zero-index propagation requires both degeneracy and confinement for the same reflector separation.

We may achieve accidental degeneracy of both conditions by adjusting the geometry of the pillar array (e.g. radius, pitch). Figure 5.4 shows the how the pillar radius affects the BiC and degeneracy conditions. For each radius, the dipole mode becomes a BiC for a particular separation, which increases along with the radius. This same set of structures support degenerate modes, where the degeneracy separation decreases with the pillar radius. We find that both conditions can be satisfied simultaneously for an intermediate pillar radius (Figure 5.4c). Finally, we shift the resonant frequency to the design wavelength at 1550 nm by scaling all dimensions of the structure proportionally. Maxwell's equations are scale-

invariant, which guarantees that the modes are unchanged by this operation.

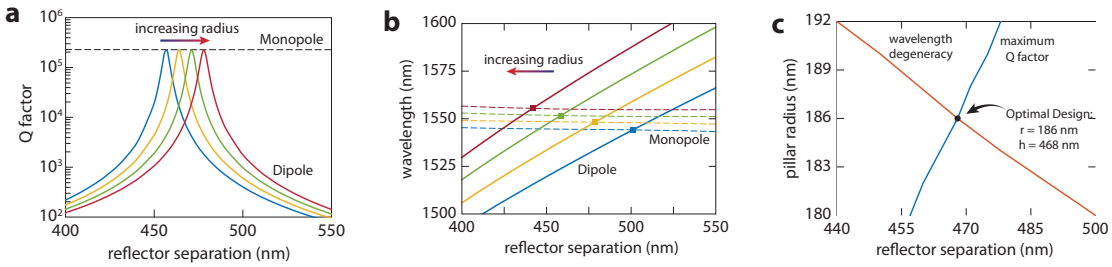

Figure 5.4: Engineering degenerate lossless modes. a) Radiative Q factor of the dipole mode in arrays with different pillar radii. The reflector separation h associated with the maximum Q factor increases with increasing radius. b) Resonant wavelengths of the monopole and dipole modes in arrays with the same range of pillar radii. The reflector separation h associated with modal degeneracy decreases with increasing radius. c) Dependence of BiC and degeneracy on the pillar radius and separation. The red curve indicates the reflector separation that leads to degenerate modes (a). The blue curve indicates the separation associated with a bound state (b). The intersection occurs for $r = 186$ nm and $h = 468$ nm.

The lossless ZIM design consists of a square array of 512-nm-tall silicon pillars, with a radius $r = 186$ nm and pitch $a = 839$ nm. The monopole and dipole modes become degenerate and lossless simultaneously at an operating wavelength of 1550 nm with a reflector separation $h = 468$ nm. This behavior is predicted by tCMT, and confirmed by finite element analysis (Figure 5.5a,b). As a result, the optimized metamaterial supports a zero-index mode at $\lambda = 1550$ nm, which propagates without phase advance or radiative loss. Figure 5.5e shows the field profile of the bound zero-index mode, which is confined to the plane of the pillar array.

We use parameter retrieval (Section) to characterize the effective index of the metamaterial across a range of wavelengths. The zero-index mode has linear dispersion near the design wavelength, supporting both positive and negative index modes (Figure 5.5c). However, the imaginary index is non-zero for all wavelengths except the zero-index point. The BiC condition (Eq.) depends on the free-space wavevector, and therefore can only

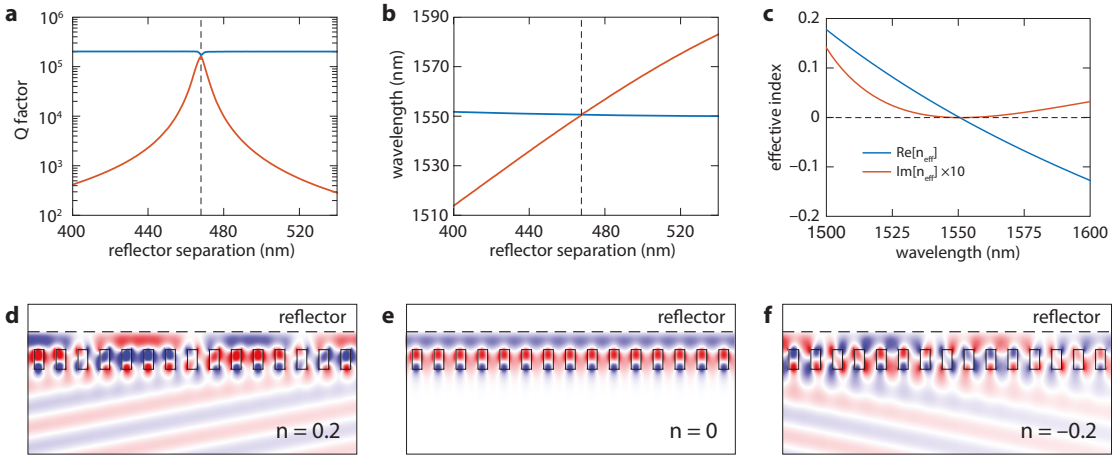

Figure 5.5: Optical properties of optimized BiC-ZIM. a) Radiative Q factor of the dipole mode for different reflector separations, forming bound state in the continuum at $h = 468$ nm. b) Resonant wavelengths of the monopole and dipole modes, which are degenerate at $\lambda = 1550$ nm for the same reflector separation as (b). c) Effective index of the optimized design: $r = 186$ nm, $r = 839$ nm, and $h = 468$ nm. The real index (blue) The imaginary index is shown at 10 $\times$ scale for clarity. d-f) Electric field distributions of the Bloch mode at different wavelengths corresponding to positive ($\lambda = 1503$ nm), zero ($\lambda = 1550$ nm), and negative index ($\lambda = 1626$ nm). The field profile shows the horizontal component of the electric field (E_x) through a vertical cross-section of the array in order to emphasize the lack of radiative loss at $n = 0$. The position of the reflector and the boundaries of the pillars are outlined in black. In all cases, electromagnetic energy propagates from left to right.

be satisfied for a single wavelength. As a result, the Q factor is finite and decreases as the operating frequency is detuned from zero index. The imaginary index signals the return of radiative loss for positive and negative index modes (Figure 5.5d-f).

Importantly, the zero-index mode is isotropic, and can be excited by incident waves from arbitrary directions. This is demonstrated by the band structure in the reduced Brillouin zone, which forms a Dirac cone at the Γ-point. Figure 5.6a shows the dispersion surfaces, and also indicates the Q factor at each point in k-space. The sharp cone at the operating wavelength indicates that the modes are simultaneously degenerate and lossless [92]. The isofrequency contours become circular in the vicinity of the Dirac point (Figure 5.6b). Similarly, the iso-Q contours (loci of equal quality factor) are also isotropic (Figure 5.6c). This feature is uncommon in BiCs, which have so far been restricted to individual points in the Brillouin zone [89, 93]. The isotropic BiC arises due to the rotational symmetry of the lattice, and is specific to the Γ-point. The zero-index mode must include contributions from two degenerate dipole modes with mutually orthogonal polarizations. Each dipole couples to continuum modes (vertically propagating plane waves) whose electric field is polarized perpendicular to the magnetic moment of the dipole mode. Thus, each dipole accounts for two of four possible radiative channels, corresponding to two orthogonal polarizations above and below the pillar array. Since the BiC ZIM design retains the two-fold rotational symmetry of the pillar array, the BiC condition is satisfied for both dipole modes automatically. Therefore, all four loss channels are eliminated. Furthermore, Bloch modes near the Γ-point can always be represented as a linear combination of the two orthogonal BiCs regardless of the propagation direction [69, 94]. Thus the zero-index mode is isotropically lossless, and the metamaterial can be described as a homogeneous effective medium [37].

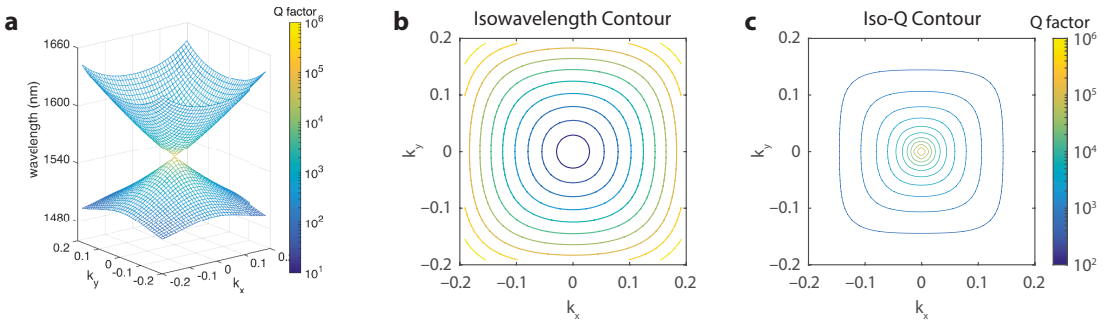

Figure 5.6: Band structure of lossless zero-index metamaterials. a) Dispersion surface of BiC-ZIM, which forms a Dirac cone at the center of the Brillouin zone. The colormap indicates the radiative Q factor. The flat band corresponding to the longitudinal dipole mode is omitted for clarity. b) Isofrequency contours of the top half of the Dirac cone, indicating isotropic modes near the Γ-point. c) Iso-Q contours of the top half of the Dirac cone. Each contour represents a locus of Bloch modes with the same radiative lifetime.

5.3 Lossless Propagation in BiC ZIM

Bound states at the Dirac-point propagate as lossless zero-index modes, which can exhibit exotic optical phenomena over large areas. These effects have so far been limited to hypothetical bulk media (Chapter 1) or infinitely tall metamaterial arrays (Chapter 2). Due to the finite extent of BiC ZIM, lossless propagation can now be implemented in planar devices and integrated with on-chip photonics. For example, we simulate a slab of BiC ZIM which is illuminated by a planar silicon waveguide (Figure 5.7a). As in the case of 2D metamaterials the input wave couples to the zero index mode, propagating through the slab without phase advance or radiative loss. The fields maintain uniform intensity throughout, and couple to an output waveguide at the far end. For comparison, we also simulate the propagation through bare pillar array without the reflector. The unit cell dimensions are altered to ensure degeneracy of monopole and dipole modes at the operating frequency. The "unbound" zero-index mode exhibits the same phase-free propagation as BiC ZIM, but the energy decays exponentially as the wave propagates due to radiative loss.

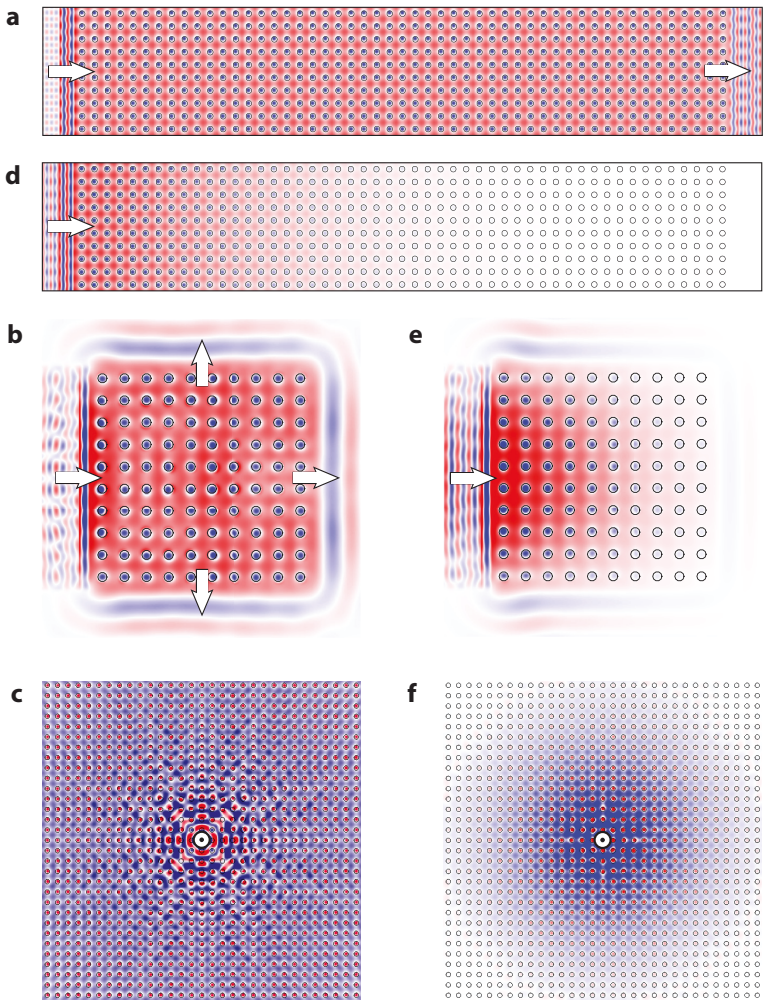

Figure 5.7: Wave propagation in lossless zero-index metamaterials. a) Plane waves in an integrated silicon slab waveguide couple into a semi-infinite slab of BiC-ZIM. The waves propagate through the zero-index region without phase advance or radiative decay, coupling into a silicon slab waveguide at opposite end. b) Plane waves excite a square BiC-ZIM array, producing refracted beams at the edges. c) A dipole emitter is placed at the center of a region of BiC-ZIM, radiating in all directions. Parts (d-f) show the same configuration as (a-c) for waves propagating though an unclad silicon pillar array as shown in Figure 5.1. All field profiles show the out-of-plane electric field on a cross-section through the plane of the array. The boundaries of the pillars are outlined in black.

The long propagation length in BiC ZIM allows access to large-area devices that were previously infeasible, including prisms, beam-shapers, and supercouplers (Figure 5.7b). Without radiative loss, the zero-index mode extends uniformly throughout the zero-index region, generating uniform plane waves at each output facet. Similarly, a point-like emitter embedded in BiC ZIM can efficiently couple to the whole array (Figure 5.7c), rather than being limited to a finite region. This effect may be critical for quantum optical applications of ZIM, where many-body effects are mediated by the zero-index mode [17, 18, 95]. The infinite spatial extent of zero-index modes allows coherent emission by multiple emitters, even when separated by macroscopic distances.

5.4 Towards Realistic Fabrication

The BiC condition can always be satisfied by a lossless reflector, but this idealization is inconsistent with the performance offered by realistic devices. Even optimized dielectric mirrors with reflectance >99% may noticeably degrade the BiC, resulting in finite propagation loss. The metamaterial design therefore must account the imperfect reflector and establish lower bounds on the reflectivity. We can predict the sensitivity of the BiC to reflector performance using tCMT. Figure 5.8a shows the Q factor of the dipole mode for a range of finite reflectances. As expected, perfectly bound modes are only attainable by ideal reflectors. The maximum Q factor drops rapidly as the reflectance decreases, scaling as $Q \propto (1-R)^{-1}$. This model does not include the residual dissipation in the silicon pillars, which is independent of the reflector separation and limits Q factor to approximately 10^5 in realistic devices. We may therefore tolerate a reflectivity $R \geq 99.95\%$ before the BiC is noticeably degraded relative to the ideal case. In addition, the Q factor of the BiC is strongly dependent on the reflector separation, particularly for the ideal reflector. The sensitivity is

reduced for mirrors with lower reflectivity, which can be attributed to a lower finesse in the Fabry-Perot cavity created between the reflector and the pillar array [96]. However, this effect is outweighed by the reduction in Q factor, and the BiC is always improved by a higher quality mirror, regardless of the reflector separation. This is summarized in Figure 5.8c, which identifies the range of reflector separations that are required to achieve a benchmark Q factor, depending on the mirror reflectance.

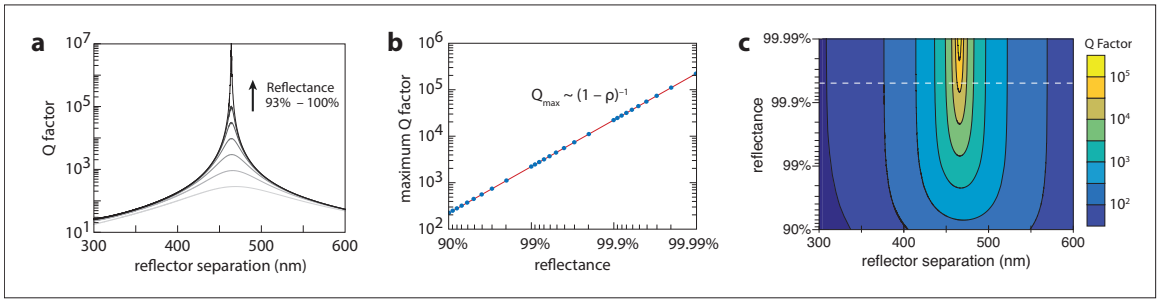

Figure 5.8: Effects of finite reflectance in BiC-ZIM. a) Radiative Q factor for the optimized BiC ZIM design (Figure 5.5) with an imperfect reflector. The contours correspond to logarithmically spaced reflectances between 92% and 99.999%. b) Maximum achievable Q factor using a finite reflectance $R = |\rho|^2$. c) Iso-Q contours, indicating the reflectance and separation necessary to achieve a given radiative lifetime. The contours are logarithmically spaced. The white line indicates the reflectance of the five-layer Bragg stack shown in Figure 5.9.

Based on these constraints, we can design a feasible BiC ZIM by incorporating a multilayer dielectric reflector. The Bragg reflector consists of five alternating layers of silicon and silica, each with an optical thickness of one-quarter wavelength (Figure 5.9a). This structure produces multiple coherent reflections, resulting in high overall reflectance without ohmic loss ($R \approx 99.95\%$). The high index contrast of the reflector creates an optical stopband over a wide range of frequencies, and makes the performance insensitive to fabrication defects [97,98]. This structure can be realized using standard lithographic processes, and integrated with silicon photonics. For example, we may use electron-beam lithography and reactive ion etching to define a silicon pillar array, as in previous ZIM designs [81]. This structure is then

conformally coated with silica using chemical vapor deposition. Finally, the Si/SiO_2 reflector can be grown using atomic layer deposition to precisely control the mirror separation and layer thickness. The dielectric mirror adds only 1.6 μm to the overall height of the structure, providing high reflectivity with a compact design.

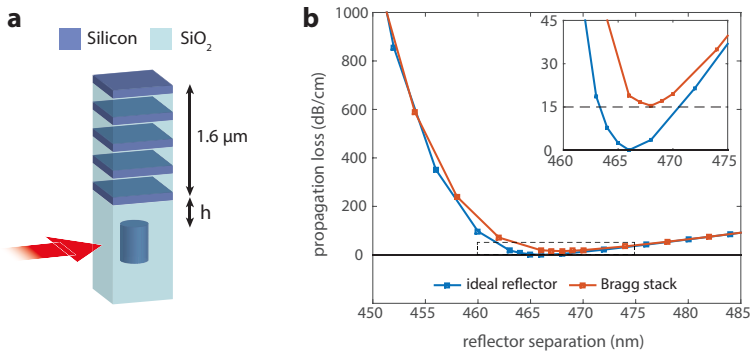

Figure 5.9: Realistic design of lossless integrated zero-index metamaterials. a) BiC-ZIM can be achieved using a dielectric reflector consisting of five alternating layers of Si/SiO_2. Each layer has a thickness of one-quarter wavelength, adding 1.6 μm to the overall height of the structure. b) Propagation loss of the zero-index mode for different reflector separations calculated using finite element simulations. The red curve indicates the loss associated with the Bragg-reflector-based BiC-ZIM, and the blue curve represents an ideal reflector ($\rho = 1$). The inset shows the propagation loss near the optimal separation, where the multilayer structure exhbits a minimum loss of 15 dB/cm.

We evaluate this realistic BiC ZIM using full-wave simulations to calculate the propagation loss of the zero-index mode (Figure 5.9b). The loss is minimized for a reflector separation $h = 468$ nm, reaching 15 dB/cm, including both radiative and intrinsic loss. While this loss is considerably poorer than silicon photonics, it corresponds to an improvement over conventional ZIM by three orders of magnitude, allowing zero-index propagation on the wafer scale.

5.5 Conclusion

The paradox of zero-index phenomena is that they are characterized by long-range coherence effects, yet restricted to short-range propagation. This restriction is not due to causality, but is an expression of confinement in waves that propagate without phase advance. Zero-index modes are necessarily compatible with continuum modes, resulting in strong radiative loss. Rather than eliminating these loss channels, we can achieve confinement through desructive interference of the radiated light, creating a bound state in the continuum. We model this system using temporal coupled mode theory, and design a metamaterial that combines a BiC with the degeneracy of dirac cones in order to create a lossless zero-index metamaterial. This design can be impemented as a silicon pillar array with a multilayer Bragg reflector, which is compatible with CMOS fabrication on a silicon-on-insulator platform. The all-dielectric approach allows for large-area implementation of integrated zero-index phenomena.

Appendix A

Complex Permittivity and Permeability

Here we demonstrate that a non-trivial magnetic response ($\mu \neq 1$) is a necessary condition to achieve a refractive index equal to zero.

The refractive index $n = n' + in'' = \sqrt{\epsilon\mu}$ is generally complex-valued, determined by the complex frequency-dependent permittivity $\epsilon(\omega)$ and permeability $\mu(\omega)$ of a material. It is therefore convenient to describe these optical parameters by their amplitudes and complex phase angles:

$$\epsilon = a\mathrm{e}^{i\theta} \tag{A.1}$$

$$\mu = b\mathrm{e}^{i\phi} \tag{A.2}$$

The amplitude (a, b) describes the strength of the induced polarization, and the phase angle (θ, ϕ) describes the phase lag between the induced polarization and the driving field. The complex nature of the optical parameters is most pronounced in materials associated with ohmic loss, such as metals and ferromagnetics [30]. Given the complex valued permit-

tivity and permeability, we then can solve for the refractive index. The complex square root has two roots:

$$n = \pm\sqrt{ab}\,\mathrm{e}^{j\frac{\theta+\phi}{2}} \tag{A.3}$$

In the complex plane, the refractive index lies along an angle bisecting the complex permittivity and permeability (Figure A.1). In this case, one root lies in the upper half-plane, corresponding to positive imaginary index, while the other lies in the lower half plane with a negative imaginary index.

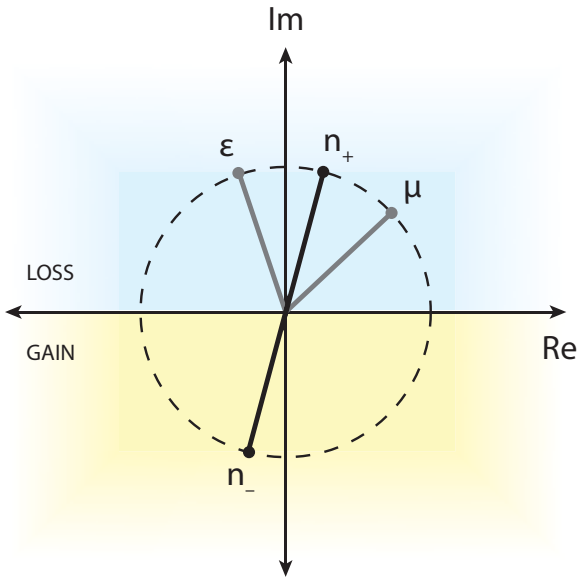

Figure A.1: Graphical representation of complex constitutive parameters. The complex permittivity and permeability are represented as phasors in the complex plane. The corresponding refractive index has two possible values, bisecting the permittivity and permeability in the upper- and lower-half plane. These solutions are associated with loss and gain, respectively.

By restricting the scope to passive materials, we will see that one of these solutions is simply a time-reversed image of the other. The real part of the refractive index (n') determines the rate of phase accumulation during propagation, while the imaginary index (n'') determines the propagation loss. For example, the electric field amplitude of a plane

wave traveling through a uniform medium is given by

$$\vec{E}(x,t) = \vec{E}_0 \mathrm{e}^{i(kx-\omega t)} \tag{A.4}$$

$$= \vec{E}_0 \mathrm{e}^{i(\frac{2\pi n}{\lambda} x\omega t)} \tag{A.5}$$

$$= \vec{E}_0 \mathrm{e}^{i(\frac{n\omega}{c} x-\omega t)} \tag{A.6}$$

$$= \vec{E}_0 \mathrm{e}^{-\frac{\omega n''}{c} x} \mathrm{e}^{i\omega(\frac{n'x}{c}-t)} \tag{A.7}$$

$$\tag{A.8}$$

Thus, the phase velocity is $\nu_p = \frac{c}{n'}$ and the attenuation constant is $\alpha = \frac{\omega n''}{c}$. Time reversal in this context is equivalent to inverting both the phase velocity and the attenuation, which can be accomplished by negating the complex index. In a passive material (i.e. no gain) the attenuation constant must be positive, so we must select the root lying in the upper half-plane. From the graphical representation in Figure A.1, we can immediately identify combinations of permittivity and permeability that yield a real index ranging from positive to negative values. Zero index phenomena ($n' = 0$) are defined by one of three conditions: $a = 0$; $b = 0$; or $\theta + \phi = \pi$. These first two scenarios can be ruled out due to causality constraints, as Kramers-Kronig relations between the real and imaginary permittivity/permeability require that any non-unity response is associated with a resonance in-quadrature [30]. Therefore, there can be no purely real permittivity or permeability equal to zero. Similarly, there can be no purely negative permittivity (e.g. $\epsilon \neq -1$). The third condition for zero index can be satisfied by causal materials, but only if both the permittivity and permeability are complex valued, with equal and opposite phase angles with respect to the complex axis. In particular, the magnetic response may not be trivial. This analysis reveals a range of non-trivial configurations that give rise to zero index, specifically $\epsilon = -\mu^*$. The majority of these combinations are associated with imaginary impedance (*e.g.* $\mathrm{Re}[\epsilon] > 0$

and $\mathrm{Re}[\mu] < 0$) creating a bandgap. The impedance is purely real only when the permittivity and permeability are purely imaginary, in which case the impedance is $Z = \frac{b}{a}$ and the attenuation constant within the material is $\alpha = \frac{\omega a b}{c}$.

Appendix B

Transformation Optics in Zero-Index Media

Here we show a rigorous coordinate transformation corresponding to a spherical region filled with a uniform refractive index equal to zero. This mapping serves as a geometric interpretation of zero-index phenomena, viewed in context of transformation optics.

Consider a region of empty, flat space with spherical coordinates $[R, \theta, \phi]$. We define a mapping from this "physical" space to a "virtual" space with distorted coordinates $[r(R), \theta, \phi]$, where the radial coordinate is scaled by some function $r(R)$. Due to the invariance of Maxwell's equations under arbitrary coordinate transformations, the behavior of electromagnetic waves in this distorted space will be identical to waves in a flat space that is filled with a spatially-varying anisotropic permittivity and permeability [60, 99]. These material properties are determined by the underlying coordinate transformation. In the case of purely radial transformations [14]:

$$\bar{\epsilon} = \bar{\mu} = \text{diag}\left[\frac{r^2}{R^2}, \frac{dR}{dr}, \frac{dr}{dR}\right] \tag{B.1}$$

where the matrix elements represent components of the (anisotropic) permittivity/permeability tensor. Consider the mapping between physical and virtual coordinates,

$$\frac{r}{b} = \left(\frac{R}{b}\right)^m \qquad \text{for } R < b \tag{B.2}$$

$$r = R \qquad \text{for } R \geq b \tag{B.3}$$

where m is a dimensionless scaling parameter and b represents the radius of the transformed region. The corresponding material properties B.1 for this transformation are given by

$$\bar{\epsilon} = \bar{\mu} = \text{diag}\left[\frac{1}{m}\left(\frac{R}{b}\right)^{m-1}, m\left(\frac{R}{b}\right)^{m-1}, m\left(\frac{R}{b}\right)^{m-1}\right] \tag{B.4}$$

In the limit $m \to \infty$, the permittivity and permeability approach zero uniformly within the transformed region. Note that the impedance is anisotropic at the boundary, but remains impedance-matched with the un-transformed space (i.e. $Z = 1$) for transverse polarization. Meanwhile, the impedance diverges for longitudinal polarizations, as expected at the boundary of a zero-index medium. In order to preserve the isotropic impedance of physical space, we may embed a corrective anisotropic impedance in the virtual space. The result is a correspondence between the isotropic index of the zero-index medium in physical space and an infinitely scaled virtual space, which has uniform index but anisotropic impedance.

Similar arguments can be made for the related transformation

$$\frac{r}{b} = (1-\alpha)\left(\frac{R}{b}\right)^m + \alpha\left(\frac{R}{b}\right) \tag{B.5}$$

As $m \to \infty$, the coordinate transformation asymptotically approaches the simple scaling transformation presented in Section 1.3, where α is the effective index within the transform region. This provides insight into nature of the discontinuity, and the treatment of fields at

the boundary of a discontinuous finite embedded coordinate transformation [15]. A uniform region of low index can be seen to uniformly stretch the fields in a flat virtual space, with an additional shear at the boundary due to the anisotropic impedance.

Appendix C

Causality in Zero Index Media

Zero-index materials support waves with infinite phase velocity, raising interesting questions about the causal nature of these waves. Here we establish some restrictions on the kinds of dispersion that give rise zero index if causality constraints are imposed. The construction makes no assumptions about the frequency dependence of the complex index, except that the index is zero at some frequency. Using Kramers-Kronig relations, we can show that 1) the zero index is associated with absorption, 2) the absorption is dispersive if the index extends across a finite bandwidth, and 3) the dispersion of the real index may be linear if and only if there is only one zero-index frequency.

C.1 Kramers-Kronig Relations

The complex refractive index $n(\omega) = \sqrt{\epsilon(\omega)\mu(\omega)}$ is defined in terms of causal response functions via the electric and magnetic susceptibility, χ_E and χ_H. These describe the polarization induced in a material by an incident field. Therefore, they are bound by causality in the time domain: $\chi(t < 0) = 0$. When expressed in the frequency domain, this causality constraint manifests as a connection between the real and imaginary compenents of $\chi(\omega)$.

By extension, the refractive index obeys a similar condition relating the real and imaginary index. The square of the index can be shown to obey Kramers-Kronig relations [22, 100]:

$$Re\left[n^2(\omega)\right] = 1 + \frac{2}{\pi} P \int_0^\infty \frac{Im\left[n^2(\omega_1)\right]}{\omega_1^2 - \omega^2} \omega_1 d\omega_1 \tag{C.1}$$

Suppose that the real index is zero at some frequency ω. Since $n^2 = \left(n'^2 - n''^2\right) + 2in'n''$, the imaginary part of n^2 also vanishes at ω (i.e. $Im\left[n^2(\omega)\right] = 0$, and $Re\left[n^2(\omega)\right] = -\left(n''(\omega)\right)^2 \leq 0$). In that case, the integral doesn't diverge at the pole $\omega_1 = \omega$, and we can ignore the principle value. Then subtract 1, multiply both sides by ω^2, and differentiate with respect to ω. We're allowed to differentiate under the integral since ω is just a parameter.

$$\begin{aligned}
\frac{d}{d\omega}\left[\omega^2\left(Re\left[n^2(\omega)\right] - 1\right)\right] &= \frac{2}{\pi}\int_0^\infty \frac{d}{d\omega}\left[\frac{\omega^2}{\omega_1^2 - \omega^2}\right] \omega_1 Im\left[n^2(\omega_1)\right] d\omega_1 && \text{(C.2)}\\
&= \frac{4}{\pi}\int_0^\infty \left(\frac{\omega^3}{\left(\omega_1^2 - \omega^2\right)^2} + \frac{\omega}{\omega_1^2 - \omega^2}\right) \omega_1 Im\left[n^2(\omega_1)\right] d\omega_1 && \text{(C.3)}\\
&= \frac{4\omega^3}{\pi}\int_0^\infty \frac{Im\left[n^2(\omega_1)\right]}{\left(\omega_1^2 - \omega^2\right)^2} \omega_1 d\omega_1 + \frac{4\omega}{\pi}\int_0^\infty \frac{Im\left[n^2(\omega_1)\right]}{\omega_1^2 - \omega^2} \omega_1 d\omega_1 && \text{(C.4)}\\
&= \frac{4\omega^3}{\pi}\int_0^\infty \frac{Im\left[n^2(\omega_1)\right]}{\left(\omega_1^2 - \omega^2\right)^2} \omega_1 d\omega_1 + 2\omega\left[Re\left[n^2(\omega)\right] - 1\right] && \text{(C.5)}
\end{aligned}$$

We can further simplify this expression by evaluating the derivative on the lefthand side:

$$\frac{d}{d\omega}\left[\omega^2\left(Re\left[n^2(\omega)\right] - 1\right)\right] = \omega^2 \frac{d}{d\omega}\left[Re\left[n^2(\omega)\right]\right] + 2\omega\left[Re\left[n^2(\omega)\right] - 1\right] \tag{C.6}$$

Cancelling like terms, we are left with the following expression:

$$\frac{d}{d\omega}\left[Re\left[n^2(\omega)\right]\right] = \frac{4\omega}{\pi}\int_0^\infty \frac{Im\left[n^2(\omega_1)\right]}{\left(\omega_1^2 - \omega^2\right)^2} \omega_1 d\omega_1 \tag{C.7}$$

Recall that $Re\left[n^2\right] = n'^2 - n''^2$, such that

$$\frac{d}{d\omega}\left[Re\left[n^2(\omega)\right]\right] = \frac{d}{d\omega}\left(n'^2 - n''^2\right) \tag{C.8}$$

$$= 2\left(n'\frac{dn'}{d\omega} - n''\frac{dn''}{d\omega}\right) \tag{C.9}$$

$$= -2n''\frac{dn''}{d\omega} \tag{C.10}$$

Combining equations C.7 and C.10,

$$n''\frac{dn''}{d\omega} = \frac{-2\omega}{\pi}\int_0^\infty \frac{Im\left[n^2(\omega_1)\right]}{\left(\omega_1^2 - \omega^2\right)^2}\omega_1 d\omega_1 = \frac{-4\omega}{\pi}\int_0^\infty \frac{n'(\omega_1)\, n''(\omega_1)}{\left(\omega_1^2 - \omega^2\right)^2}\omega_1 d\omega_1 \tag{C.11}$$

Thus far, all we have assumed is that the index is zero at a single frequency ω. This establishes a relationship between the absorption n'', the dispersion of the absorption $\frac{dn''}{d\omega}$, and the spectra of both the real and imaginary index $n'(\omega_1)\, n''(\omega_1)$. From here we can start to make claims about the possible causal relationships at the zero crossing. For example, suppose that the absorption is nearly dispersionless, $\frac{dn''}{d\omega} \approx 0$.

$$n''\frac{dn''}{d\omega}(\omega) = 0 = \int_0^\infty \frac{n'(\omega_1)\, n''(\omega_1)}{\left(\omega_1^2 - \omega^2\right)^2}\omega_1 d\omega_1 \tag{C.12}$$

The denominator is always positive, so the numerator must span both positive and negative values in order to cancel to zero. In passive materials, the imaginary index is non-negative, which implies there will be substantial regions where the real index is negative and the loss is non-zero. These negative index regions must be sufficiently close to the pole at $\omega = \omega_1$ to provide a strong negative contribution, and the loss also can't be zero in the negative index range. Note that this condition links negative index phenomena with absorption, where the integrated product $n'(\omega_1)\, n''(\omega_1)$ must be sufficiently negative. Therefore, the absorption may be suppressed by enhancing the magnitude of the negative index in regions near the resonance. In the limit of lossless zero-index propagation (e.g.

magnetic-electric-lorentz model), the negative index becomes singular at the resonant frequency so that no further loss is required at other frequencies. This same mechanism allows BiC metamaterials to support lossless propagation with negative index, as the "sharpness" of the resonance scales with the quality factor.

C.2 Photonic Band Gaps

What if the real index is zero for some extended range? This would seem to break causality, unless the loss is also strongly dispersive. Suppose that $n'(\omega) = 0$ in the frequency range $\omega_{low} < \omega < \omega_{high}$. Note that this is equivalent to a photonic bandgap, which is associated with strong dispersive loss. The dispersionless zero index clears the integral for a range of frequencies.

$$n'' \frac{dn''}{d\omega}(\omega) = \int_0^{\omega_{low}} \frac{n'(\omega_1)\, n''(\omega_1)}{\left(\omega_1^2 - \omega^2\right)^2} \omega_1 d\omega_1 + \int_{\omega_{high}}^{\infty} \frac{n'(\omega_1)\, n''(\omega_1)}{\left(\omega_1^2 - \omega^2\right)^2} \omega_1 d\omega_1 \tag{C.13}$$

This represents the wavelength dependence of the loss within the "bandgap". We are interested in what happens to this integral (and therefore the loss), as we vary the frequency. For frequencies within the bandgap ($\omega_{low} < \omega < \omega_{high}$), we don't encounter the pole at $\omega = \omega_1$, and the integral is exptected to converge (otherwise the real index would have diverged too). However, the loss value cannot be independent of the frequency across the entire range, and will generally be dispersive. The frequency ω can be interpreted as the center of an infinite potential $\left(\omega_1^2 - \omega^2\right)^{-2}$, which samples the real and imaginary index on either side of the bandgap. As the frequency shifts across the bandgap, the potential samples each side with differing strengths. In order for the loss to be dispersionless (i.e. $n'' \frac{dn''}{d\omega}(\omega) = 0$), the index must be positive on one side of the bandgap and negative on the other, such that the two halves of the integral cancel for the frequency ω. In that case, simply

shifting the wavelength toward the negative index side will upset the balance, resulting in a non-zero dispersive absorption. In the context of photonic bandgaps, this is why we see a maximum absorption at the center of the gap, where $\frac{dn''}{d\omega} = 0$. Therefore, while it is possible to arrange for the index to be zero within a finite bandwidth (e.g. a bandgap), that range can neither be lossless nor have constant loss.

C.3 Dispersion at the Band Edge

The presence of a bandgap also dictates the dispersion of the real index at the bandedge. By breaking the integral into two halves, we may no longer guarantee that the Cauchy principle value will converge for frequencies near either end of the bandgap. The behavior will depend on the real and imaginary index just outside of the bandgap. To demonstrate, we can consider an arbirtary dispersive index, expanded as a power series near ω_{low}:

$$n'(\omega) = a_0 + a_1(\omega - \omega_{low}) + a_2(\omega - \omega_{low})^2 + \dots \tag{C.14}$$

$$n''(\omega) = b_0 + b_1(\omega - \omega_{low}) + b_2(\omega - \omega_{low})^2 + \dots \tag{C.15}$$

We may assume that the index is continuous at the bandedge, so $a_0 = 0$, while still allowing for non-zero loss b_0. We then evaluate the first half integral at the lower bandedge:

$$
\begin{aligned}
n''\frac{dn''}{d\omega}\left(\omega_{low}\right) &= \int_0^{\omega_{low}} \frac{n'\left(\omega_1\right) n''\left(\omega_1\right)}{\left(\omega_1^2-\omega_{low}^2\right)^2}\omega_1 d\omega_1 \\
&= \int_0^{\omega_{low}} \frac{\omega_1}{\left(\omega_1^2-\omega_{low}^2\right)^2}\left[a_1 b_0\left(\omega_1-\omega_{low}\right)+\left(a_2 b_0+a_1 b_1\right)\left(\omega_1-\omega_{low}\right)^2+...\right] d\omega_1 \\
&= \sum_{j=1}^{\infty} c_j \int_0^{\omega_{low}} \frac{\omega_1\left(\omega_1-\omega_{low}\right)^j}{\left(\omega_1^2-\omega_{low}^2\right)^2} d\omega_1 \\
&= \sum_{j=1}^{\infty} c_j \int_0^{\omega_{low}} \frac{\omega_1}{\left(\omega_1+\omega_{low}\right)^2}\left(\omega_1-\omega_{low}\right)^{j-2} d\omega_1
\end{aligned}
$$

Here, the coefficients for the real and imaginary index are combined in c_j. We can evaluate each component integral individually to determine the dispersive absorption at the band edge. For orders $j \geq 2$, the integrand is finite across the entire range, so the integral can be evaluated (it ends up proportional to ω_{low}^{j-2}). However, the first term $j = 1$ retains a pole at $\omega_1 = \omega_{low}$, and it does not converge. A diverging integral corresponds to a discontuity in the absorption at the bandedge, which is unphysical. Instead, we may conclude that the coefficient $c_1 = a_1 b_0 = 0$, and that the dispersion at the bandedge must be of quadratic order or higher.

Conclusions

Using Kramers-Kronig relations, we can make several general statements about the kinds of zero-index phenomena that are allowed by causality. If the real index is zero for some continuous range of frequencies, then those frequencies must be associated with dissipation (*i.e.* non-zero imaginary index). Furthermore, this loss must be frequency-dependent. Such a photonic bandgap cannot support linear dispersion at the band edge. Instead, the real index must have quadratic dispersion or higher. Linear dispersion is only allowed when the index is zero for exactly one frequency. In this case, the real index is positive on for high frequencies and negative for low frequencies. The negative index frequencies are necessarily

associated with loss unless the Q-factor of the resonance is infinite, as in the case of bound states in the continuum (Chapter 5).

Appendix D

Role of Metals in Integrated ZIM

The zero-index effect that is demonstrated in Chapter 4 is due to Mie resonances of a purely dielectric photonic crystal [69]. Though we incorporate gold structures into our design, these metal layers only contribute to the enforcement of the fundamental TM mode, simulating the modes of infinitely tall pillars. In addition, the matal layers facilitate light confinement within the metamaterial structure; they do not make any plasmonic resonance-based contribution to the metamaterial. In this section, we show that there exist Dirac cones without any metal and that the metal only contributes to the overall performance of the metamaterial. The different contributions of the gold mirrors and the gold caps above the pillars are investigated separately below.

D.1 Gold Mirrors

We simulate the modes at the Γ-point for our integrated ZIM structure without the gold mirrors. By tuning the thickness of the SU-8 polymer, as discussed in section 4.4, we obtain an additional degree of freedom by which we can engineer a degeneracy at the Γ-point, even without the gold mirrors. By tuning the thickness of the SU-8 polymer layer, we obtain

multiple geometries that exhibit the degeneracy between the monopole and dipole modes that is necessary to obtain a Dirac cone. These correspond to SU-8 thicknesses of 687.5 nm, 1125 nm, 1575 nm, and 1725 nm.

We calculate the band structures for these geometries to verify their degeneracies (Figure D.1). In the absence of the gold mirrors, the resulting band structures are less linear and more quadratic near the degeneracy point. This is a result of radiative loss from the dipole mode but not the monopole mode, which breaks the degeneracy of the imaginary eigenfrequency [92]. However, we still observe a conical shape and a degeneracy at a single wavelength, indicative of a Dirac-cone dispersion.

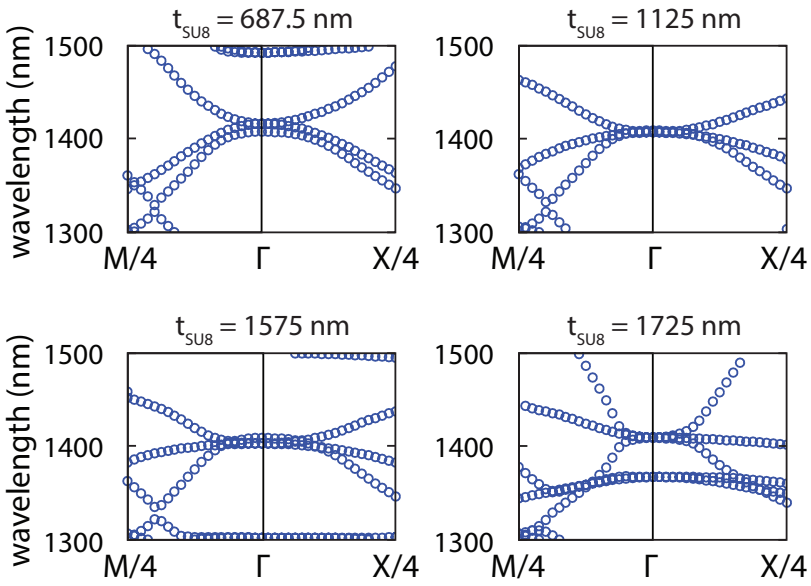

Figure D.1: Band structure of integrated ZIM without metal layers, for various SU-8 thicknesses. The SU-8 thicknesses were selected to achieve triply degenerate states at the Γ-point, forming blunted Dirac cones.

We estimate the propagation loss for the structures with the modal degeneracies using finite-difference time-domain (FDTD) simulations and the method described in section 4.4. The resulting propagation loss are plotted in Figure D.2. We also plot the propagation loss for the corresponding gold-mirror Dirac-cone structures for comparison. We obtain lower

propagation loss when using the gold mirrors. Given the shape of the Dirac cones and the propagation loss that are obtained using the structures that are clad with gold, it is clear that the performance of the metamaterial is enhanced by the gold mirrors. This is due to the additional confinement provided by the mirrors as well as due to the enforcement of a "clean" TM mode by constraining the orientation of electric field to be normal to the parallel plates.

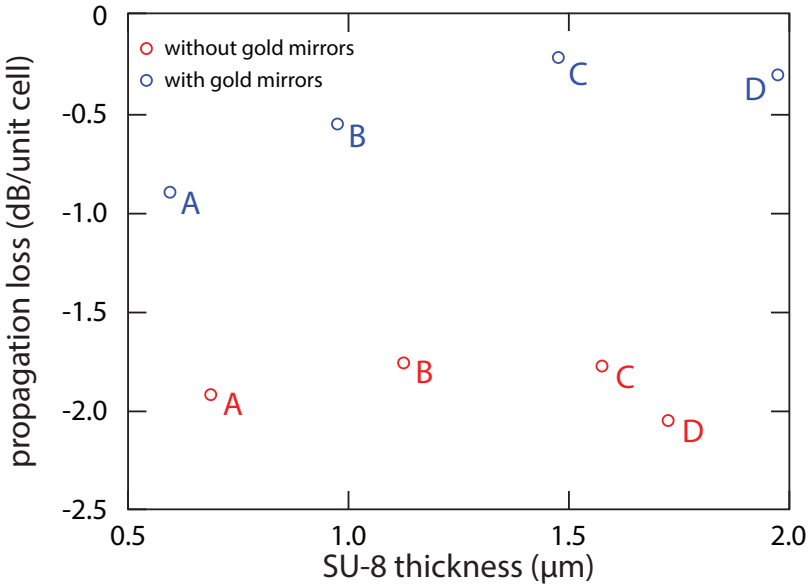

Figure D.2: Comparison of loss in integrated ZIM with and without metals. In each case, the SU-8 thickness is selected to achieve triply degenerate states at the Γ-point, corresponding to Figures 4.5 and D.1

D.2 Gold Caps

Due to the fabrication procedure, the lower gold mirror in the structure creates a cap on top of the silicon pillars upon deposition. This cap is only a consequence of the fabrication procedure, and not a necessary component of the metamaterial. We demonstrate this by simulating the band structure of the proposed structure without these gold caps and also producing Dirac-cone dispersion. Removing the gold cap causes effects analogous to a devi-

ation from the ideal radius described in section 4.4. Optimize the cap-free design using the process described in section 4.2 to obtain new dimensions for the smallest possible $|n_{\text{eff}}|$, with a radius of 189 nm and a pitch of 727 nm. We simulate the band structure for this geometry (Figure D.3), which also achieves degeneracy between the monopole mode and the dipole modes at the Γ-point. Additionally, because this design still possesses the gold mirrors, the Dirac cone exhibits linear dispersion similar to the band structure of the fabricated design. Thus, the gold caps do not play an important role in the demonstrated zero-index behavior.

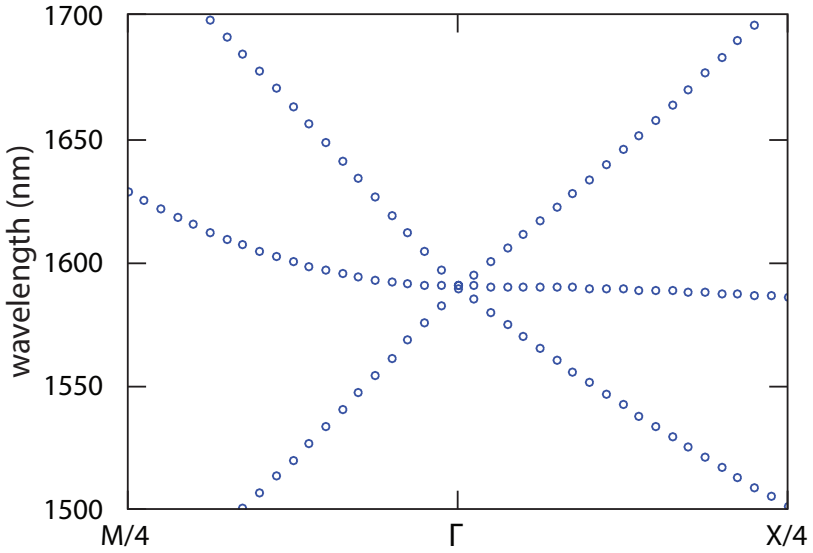

Figure D.3: Band structure of integrated ZIM without metal caps on the pillars.

Appendix E

Extracting the Effective Index from a Prism

We extract the prism index from images of refraction through a zero-index metamaterial prism. Figure E.1a shows a silicon waveguide feeding into a triangular prism, which couples to a large SU-8 slab waveguide with a radius of 125 μm. Light enters through the silicon waveguide and refracts through the prism into the SU-8 slab waveguide. This beam scatters at the edge of the SU-8 slab waveguide, and is imaged from above using an InGaAs camera (Figure E.1b). Images are taken for a range of input wavelengths between 1480 nm and 1680 nm. In addition to refraction images, we use reference images to identify alignment marks, which are used to locate and orient the prism.

We first determine the position of the alignment marks in the microscope images using a 2D Gaussian fit. This allows us to orient the prism and map pixels near the edge to polar coordinates. The refracted beam is then located using a polar 2D Gaussian fit to extract the refracted angle. This refracted angle is used to calculate the prism index using Snell's law and the effective index of the SU-8 slab waveguide. The measurement error is propagated

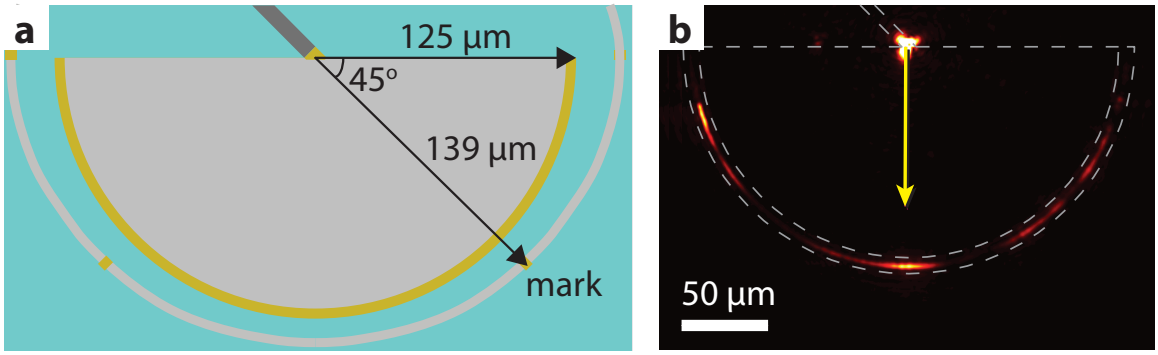

Figure E.1: Prism-based measurement configuration. a) Schematic and b) microscope image of the measurement configuration. In (a), a silicon waveguide directs light into a metamaterial prism, which couples to an SU-8 slab waveguide. A separate SU-8 waveguide, outside of the SU-8 slab waveguide, is used to illuminate alignment marks. In (b), white dashed lines indicate the position of the silicon waveguide and the SU-8 slab waveguide.

throughout the calculation and includes the effects of camera pixel size, resolution, and fit uncertainty due to variance in the data.

E.1 Alignment Marks

There are two alignment marks placed at $\pm 45^\circ$ relative to the surface normal of the prism output, and 139.2 µm from the center of the prism (Figure E.1a). They are both 3 µm wide, and show up brightly in the images as shown in Figure E.2a. By identifying the locations of each alignment mark we can determine the SU-8 slab waveguide's radius r, rotation offset α_0, and prism location from which we define the origin $\{x_0, y_0\}$:

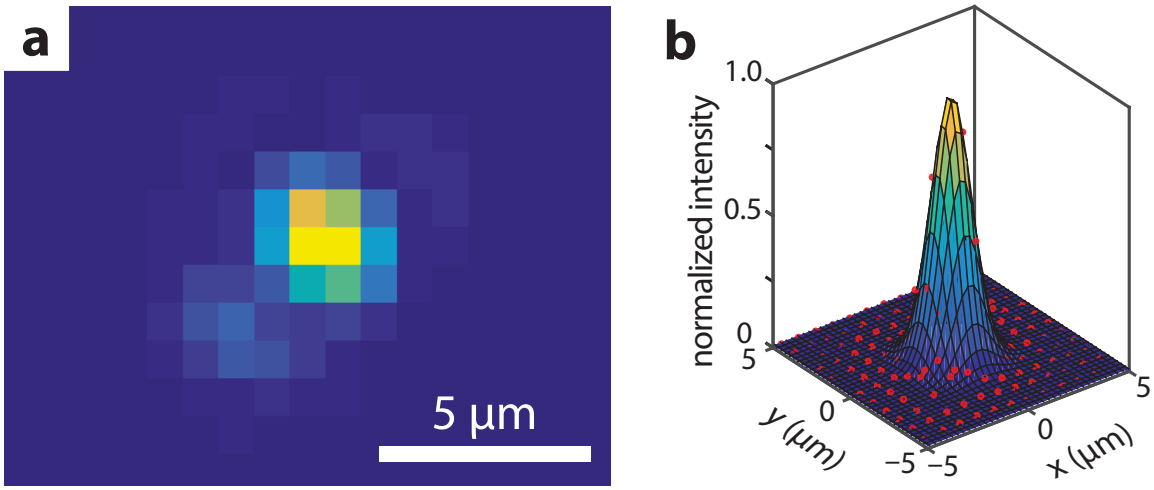

Figure E.2: Location of illuminated alignment marks. a) Infrared image of an alignment mark. b) 2D Gaussian fit of the measured intensity. Red dots: measured intensities; colored surface: Gaussian surface fit. In (b), we fit the measured intensity values to a 2D Gaussian model using a nonlinear least-squares algorithm.

$$r = \frac{125\mu\text{m}}{139.2\mu\text{m}}\sqrt{\frac{(x_{\text{AM1}} - x_{\text{AM2}})^2 + (y_{\text{AM1}} - y_{\text{AM2}})^2}{2}}$$

$$\alpha_0 = \tan^{-1}\left(\frac{y_{\text{AM1}} - y_{\text{AM2}}}{x_{\text{AM1}} - x_{\text{AM2}}}\right)$$

$$x_0 = x_{\text{AM1}} + \frac{125\mu\text{m}}{139.2\mu\text{m}} r\cos\frac{\pi}{4} + \alpha_0$$

$$y_0 = y_{\text{AM1}} + \frac{125\mu\text{m}}{139.2\mu\text{m}} r\sin\frac{\pi}{4} + \alpha_0$$

where the measured values $\{x_{\text{AM1}}, y_{\text{AM1}}\}$ and $\{x_{\text{AM2}}, y_{\text{AM2}}\}$ are the coordinates of the two alignment marks.

To determine the center of the alignment marks, we fit the intensity profile of each mark to a 2D Gaussian function:

$$I\left(x, y; a, b_x, b_y, c, d\right) = a\,\mathrm{e}^{-\left(\frac{(x-b_x)^2}{2c^2} - \frac{(x-b_x)^2}{2c^2}\right)} + d$$

The fitting parameters are amplitude a, x-center position b_x, y-center position b_y, width c, and intensity offset d. We use a nonlinear least-squares optimization method to minimize the

residuals of the data (Figure E.2b). This solution also includes an estimate of the covariance of the fitting parameters.

To ensure accurate fits for the data, we consider only the pixels in the vicinity of the alignment marks. Too narrow a window would reduce the fit quality, and too wide a window would include other peaks. We use a 20-pixel-wide window, which is significantly wider than the alignment mark ($c = 1.38$ px), but small enough to exclude extraneous features. The window is centered at the maximum intensity for each alignment mark. From the fit, we calculate the SU-8 slab waveguide radius r, offset angle α_0, and the origin position $\{x_0, y_0\}$.

E.2 Refraction Angle

From the measured positions of the alignment marks, we can define the edge of the SU-8 slab waveguide. The refracted beam propagating within the SU-8 slab waveguide will be scattered from this edge, appearing as a bright band. Since the edge is curved, it is convenient to map the positions of the pixels to polar coordinates centered at the prism (Figure E.3). We can then locate the center of the refracted beam using the same method as for the alignment marks.

Pixels are mapped to polar coordinates $\{x, y\} \rightarrow \{r, \alpha\}$ according to the alignment mark measurements:

$$r = \sqrt{(x - x_0)^2 + (y - y_0)^2}$$
$$\alpha = \tan^{-1}\left(\frac{y - y_0}{x - x_0}\right) + \alpha_0$$

In polar coordinates, we fit the beam intensity profile to another 2D Gaussian, this time allowing for two peaks to account for the sometimes-irregular beam profile:

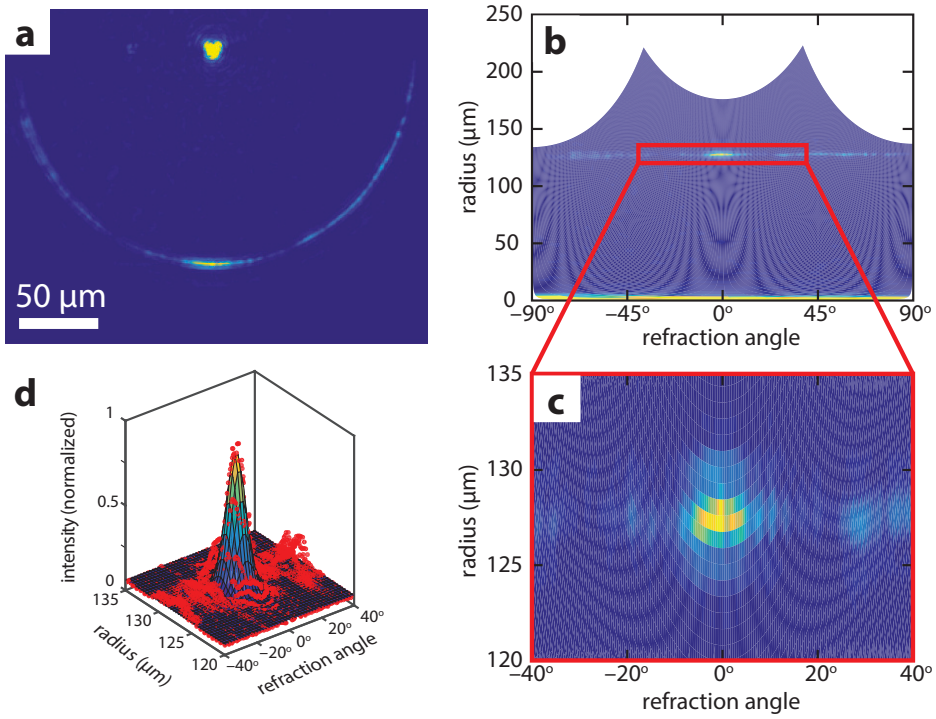

Figure E.3: Extracting refraction angle from infrared images. a) Measured intensity values in the Cartesian coordinates. b) Measured intensity values mapped to the polar coordinates. From (a) to (b), the curved edge of the SU-8 slab waveguide is transformed into a horizontal line. c) Magnified view of the refracted beam region. d) 2D Gaussian fit of the measured intensity in (c). Red dots: measured intensities; colored surface: Gaussian surface fit. In (d), we fit the measured intensity values to a 2D Gaussian model to extract the refracted angle.

$$I\left(r,\alpha;a_1,a_2,b_r,b_{1\alpha},b_{2\alpha},c_r,c_{1\alpha},c_{2\alpha},d\right)=a_1\,\mathrm{e}^{-\left(\frac{(r-b_r)^2}{2c_r^2}-\frac{(\alpha-b_{1\alpha})^2}{2c_{1\alpha}^2}\right)}+a_2\,\mathrm{e}^{-\left(\frac{(r-b_r)^2}{2c_r^2}-\frac{(\alpha-b_{2\alpha})^2}{2c_{2\alpha}^2}\right)}+d$$

The refracted angle is measured using the stronger of the two peaks. Figure E.3d shows an example of the 2D Gaussian fit for an excitation wavelength of 1590 nm. We repeat this measurement for several wavelengths to track the refracted beam.

E.3 Prism Index

The prism index is calculated using the measured refraction angle. Light enters the prism normal to the input surface, and refracts into the SU-8 slab waveguide at an incident angle of 45°. From Snell's law:

$$n_{\text{prism}}=n_{\text{slab}}\frac{\sin(\alpha_c)}{\sin(45^\circ)}=1.54\sqrt{2}\sin(\alpha_c)$$

The extracted index shows a continuous transition from positive to negative index with increasing wavelength (Figure 4.9d). The zero crossing is centered at 1570 nm, where the index dispersion is linear. The error bars in this plot represent the uncertainty in the measured index, assuming a confidence level of 95% [101]. They include the effects of the image size, pixel size, resolution, and propagated errors from each measurement stage. Given the calculated uncertainty in the measurement, the observed zero index "bandgap", in which the real index is equal to zero with 95% confidence, is at most 49 nm wide.

Appendix F

Prism Measurement Contol Experiment

To validate the results of the metamaterial prism index measurement, we perform a control measurement on the same measurement setup (Figure 4.7) without the prism. In this control device, light from the input silicon waveguide couples directly into free space ($n_{\text{air}} = 1$) before entering the SU-8 slab waveguide at an incident angle of 45° (Figure F.1a). Using the same experimental and simulation methods as the prism measurement, we observe a refracted beam in the far field at an angle of $25.6° \pm 1.3°$ (Figure F.1b). Based on the Snell's law, this angle corresponds to refraction from a material with index $n = 0.94 \pm 0.04$, which is very close to the index of air. Figure F.1c shows the measured and simulated indices of the control experiment, which agree with each other well throughout the measurement wavelength range. These results confirm that the measured index shown in Figure 4.9 corresponds to the effective index of the metamaterial prism, instead of the artifact of the measurement setup.

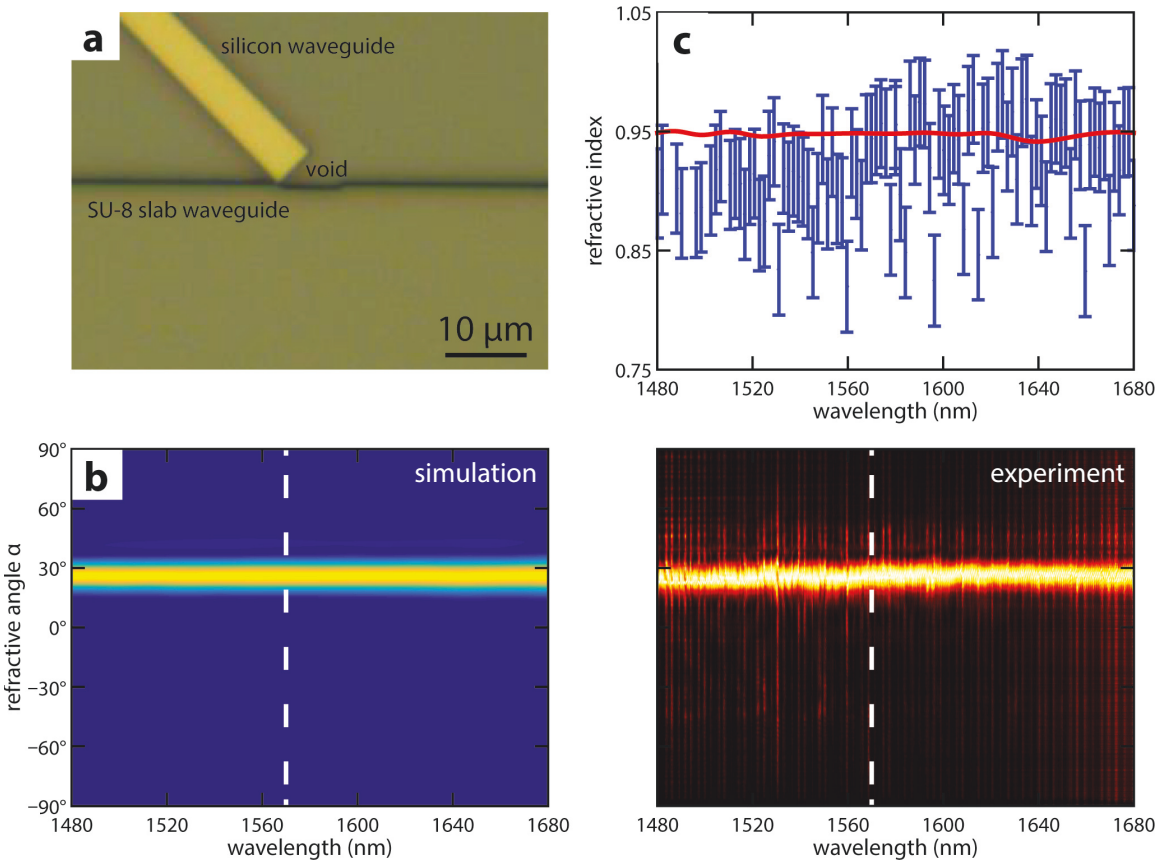

Figure F.1: Optical image, simulation and experimental results of the control experiment. a) Optical image of the control device. This device is the same as the measurement setup in Figure 4.7 except for the absence of the metamaterial prism. b) Simulated (left) and measured (right) far-field patterns. c) Measured and simulated effective index of the control experiment. The blue dots indicate the measured refractive index, with error bars representing the uncertainties in the measurement. The measurement agrees well with the simulated effective index (red line).

Appendix G

Temporal Coupled Mode Theory

Temporal coupled mode theory (tCMT) can be used to model the interaction of a pair of weakly coupled oscillators with the radiation continuum [51]. In Chapter 5, we used tCMT to describe the time evolution of the dipole mode within an integrated ZIM slab adjacent to a reflective plane. The effective decay rate of the dipole mode can be modulated by adjusting the separation between the pillar array and the reflector, causing the radiative loss to vanish for specific separations. In this appendix, we derive the tCMT equations for effective decay rate and effective wavelength, and describe the process for calculating the coupling coefficients.

G.1 Deriving Coupled Mode Equations

The time-dependent amplitude of the propagating mode is described by equations 5.1-5.3 in Chapter 5, where there is no incident wave from free space ($s_{1+} = 0$). This mode is anti-symmetric under reflection across the plane of the array, so the coupling coefficients have opposite phase on either side of the array, $d_1 = d_2$.

$$\frac{dA(t)}{dt} = \left(-i\omega_0 - \frac{1}{\tau_0}\right) A - d_1 s_{2+} \tag{G.1}$$

$$s_{1-} = t s_{2+} + d_1 A \tag{G.2}$$

$$s_{2-} = r s2 + d_1 A \tag{G.3}$$

$$s_{2+} = \rho \mathrm{e}^{i\psi} s_{2-} \tag{G.4}$$

We solve these equations simultaneously to determine the time evolution of the bound mode. Combining equations G.3 and G.4:

$$\begin{aligned} s_{2+} = \rho \mathrm{e}^{i\psi} s_{2-} &= \rho \mathrm{e}^{i\psi} \left(r s_{2+} - d_1 A\right) \\ &\rightarrow s_{2+} = \frac{d_1 A}{r \rho^{-1} \mathrm{e}^{i\psi}} \end{aligned} \tag{G.5}$$

This is used to eliminate the plane wave amplitude in equation G.1,

$$\begin{aligned} \frac{dA(t)}{dt} &= \left(-i\omega_0 - \frac{1}{\tau_0}\right) A - d_1 \left(\frac{d_1 A}{r - \rho^{-1} \mathrm{e}^{i\psi}}\right) \\ &\equiv \left(-i\omega_{\text{eff}} - \frac{1}{\tau_{\text{eff}}}\right) A \end{aligned} \tag{G.6}$$

where the coupled mode has an effective frequency ω_{eff} and effective decay rate τ_{eff},

$$\omega_{\text{eff}} = \omega_0 + \mathrm{Im}\left[\frac{d_1^2}{r - \rho^{-1} \mathrm{e}^{i\psi}}\right] \tag{G.7}$$

$$\frac{1}{\tau_{\text{eff}}} = \frac{1}{\tau_0} + \mathrm{Re}\left[\frac{d_1^2}{r - \rho^{-1} \mathrm{e}^{i\psi}}\right] \tag{G.8}$$

These effective parameters depend on the separation h between the pillar array, via the propagation phase $\psi = 2kh$, which can be tuned to achieve a bound state in the continuum.

The BiC occurs when the radiated wave disappears (*i.e.* $s_{1-} = 0$). Combining equations G.2–G.4,

$$\begin{aligned} s_{1-} + s_{2-} &= (t + r)s_{2+} \\ &= (t + r)\rho e^{i\psi} s_{2-} \\ &\rightarrow t + r = \rho^{-1} e^{-i\psi} \end{aligned} \tag{G.9}$$

The reflection and transmission coefficients are connected via Stokes relations, $r^*r + t^*t = 1$ and $r^*t + t^*r = 0$, as a consequence of time-reversal symmetry [91]. Therefore, the quantity $(t + r)$ must have unit magnitude. Assuming a perfectly reflective mirror ($\rho = 1$), the BiC condition is satisfied when the propagation phase $\psi = \arg(t + r) + 2\pi n$. The propagation phase is proportional to the separation between the pillar array and the reflector, so we are guaranteed to find bound states for some separation h. Furthermore there is an infinite series of such configurations, where the reflector separation is shifted in increments of one half wavelength.

G.2 Parameter Estimation

The solution is parameterized by four properties of the bare silicon pillar array: intrinsic decay rate τ_0, intrinsic resonant frequency ω_0, reflection coefficient r, and decay coefficient d_1. We calculate these model parameters for the metamaterial design using finite element simulations. The first two parameters can be solved directly using eigenfrequency analysis of the Bloch modes at the center of the Brillouin zone, whereas the reflection and decay coefficients must be calculated indirectly from frequency-dependent reflectance analysis. Note that the parameter r corresponds to a direct reflection process, where an incident plane wave reflects from the surface of the pillar array into a counter-propagating plane wave. There is

also an indirect reflection process, where incident waves couple intermediately to the guided mode before being radiated back toward the source. In general both of these processes occur simultaneously, leading to a Fano resonance in the reflection spectrum where the two pathways interfere [102]. Therefore, the direct reflection coefficient must be extracted from the simulated reflection spectrum, accounting for the indirect path.

We model this process using the same tCMT formalism as before, this time assuming steady-state plane wave illumination from one side ($s_{1+} \neq 0$, $s_{2+} = 0$)

$$\begin{aligned} \frac{dA}{dt} = -i\omega A = -i\omega_0 A\frac{1}{\tau_0} + d_1 s_{1+} \\ \rightarrow A = \underbrace{\frac{d_1}{i(\omega_0 - \omega) + \frac{1}{\tau_0}}}_{\gamma(\omega)} s_{1+} \end{aligned} \tag{G.10}$$

where $\gamma(\omega) = i(\omega_0 - \omega) + \frac{1}{\tau_0}$ determines the strength of the frequency-dependent coupling between the bound mode A and an incident plane wave with frequency ω. This additional coupling term accounts for the indirect path, allowing us to connect the direct reflection and transmission coefficients to the measured reflection and transmission spectra:

$$\begin{aligned} s_{1-} = r s_{1+} + d_1 A = \left(r + \frac{d_1^2}{\gamma}\right) s_{1+} \\ \rightarrow r_{\text{measured}} \equiv \frac{s_{1-}}{s_{1+}} = r + \frac{d_1^2}{\gamma} \end{aligned} \tag{G.11}$$

$$\begin{aligned} s_{2-} = t s_{1+} - d_1 A = \left(t - \frac{d_1^2}{\gamma}\right) s_{1+} \\ \rightarrow t_{\text{measured}} \equiv \frac{s_{2-}}{s_{1+}} = t - \frac{d_1^2}{\gamma} \end{aligned} \tag{G.12}$$

Thus, the measured transmission and reflection coefficents are augmented by the same frequency dependent function $\frac{d_1^2}{\gamma(\omega)}$. The modulus of d_1 is fixed by the decay rate of the bound

state, $|d_n|^2 = \frac{1}{\tau_0}$, so the value is determined up to a complex phase factor. We calculate this unknown phase by enforcing conservation of energy, as the reflectance and transmittance sum to 100%. Figure G.1a shows the power mismatch (defined as $1 - |r|^2 - |t|^2$) for all possible values of d_1, which vanishes for a single value. With d_1 fixed, the direct reflection and transmission coefficients can be evaluated from equations G.11 and G.12.

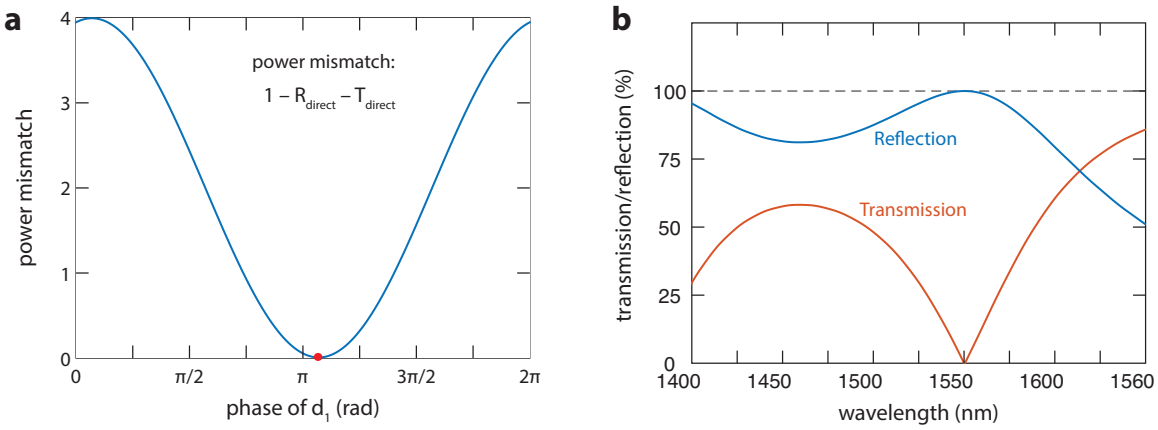

Figure G.1: a) Estimating the phase of d_1 via conservation of energy. The blue curve indicates the energy defecit $(1 - R - T)$ for all possible values of d_1. The devicit is zero for a single value, indicated by the red dot. b) Reflection and transmission spectra for a single array of pillars. These curves represent the overall reflection/transmission, including direct and indirect paths. The BiC condition is satisfied at $\lambda = 1550$ nm, where the reflectance equals 100%.

The direct reflection/transmission coefficients can be used in conjunction with the BiC condition G.9 to determine the reflector spacing necessary to create a bound state. We note that the solution is unchanged by substituting the measured reflection and transmission coefficients:

$$t_{\text{measured}} + r_{\text{measured}} = t - \frac{d_1^2}{\gamma} + r + \frac{d_1^2}{\gamma} = t + r \tag{G.13}$$

Therefore, it is sufficient to use the more accessible measured values to evaluate the BiC condition. Moreover, the measured reflection spectrum is strongly peaked at the BiC wavelength (Figure G.1b). This is a consequence of interference between the direct and

indirect pathways, creating a Fano resonance [79, 103]. Such resonant reflection will always occur in structures supporting bound modes that are coupled to a single radiative channel. Based on this rule, it is straightforward to design a bound state based on the measured reflection spectrum: the BiC will occur at the wavelength where the reflectance equals 100%, and the separation between the pillar array and the reflector must be an integer multiple of the wavelength. By following this process we can quickly evaluate the characteristics of the bound state for different metamaterial geometries, allowing optimization of the array pitch and pillar radius.

Bibliography

[1] R A Shelby, D R Smith, and S Schultz. Experimental verification of a negative index of refraction. *Science*, 292(5514):77–79, 2001.

[2] Jason Valentine, Shuang Zhang, Thomas Zentgraf, Erick Ulin-Avila, Dentcho A. Genov, Guy Bartal, and Xiang Zhang. Three-dimensional optical metamaterial with a negative refractive index. *Nature*, 455(7211):376–379, 2008.

[3] M. Born and E. Wolf. *Principles of Optics*. Pergamon Press, New York, 1999.

[4] Leon Brillouin. *Wave Propagation and Group Velocity*. Academic Press, New York, 1960.

[5] J B Pendry. Controlling Electromagnetic Fields. *Science*, 1780(2006):1780–1782, 2011.

[6] U Leonhardt. Optical conformal mapping. *Science*, 312(5781):1777–1780, 2006.

[7] Dentcho A. Genov, Shuang Zhang, and Xiang Zhang. Mimicking celestial mechanics in metamaterials. *Nature Physics*, 5(9):687–692, 2009.

[8] D Schurig, J J Mock, B J Justice, S a Cummer, J B Pendry, a F Starr, and D R Smith. Metamaterial electromagnetic cloak at microwave frequencies. *Science*, 314(5801):977–980, 2006.

[9] Wenshan Cai, UK Chettiar, AV Kildishev, and VM Shalaev. Optical cloaking with metamaterials. *Nature photonics*, 1:224, 2007.

[10] Zubin Jacob, Leonid V Alekseyev, and Evgenii Narimanov. Optical Hyperlens: Far-field imaging beyond the diffraction limit. *Optics express*, 14(18):8247–56, 2006.

[11] Zhaowei Liu, Hyesog Lee, Yi Xiong, Cheng Sun, and Xiang Zhang. Far-Field Optical Hyperlens Magnifying Sub-Diffraction-Limited Objects. *Science*, 315(5819):1686, 2007.

[12] Evgenii E. Narimanov and Alexander V. Kildishev. Optical black hole: Broadband omnidirectional light absorber. *Applied Physics Letters*, 95(4):2009–2011, 2009.

[13] D Roberts, N Kundtz, and D R Smith. Optical lens compression via transformation optics. *Optics Express*, 17(19):16535–42, 2009.

[14] Aaron J. Danner, Tomáš Tyc, and Ulf Leonhardt. Controlling birefringence in dielectrics. *Nature Photonics*, 5(6):357–359, 2011.

[15] Marco Rahm, Steven A. Cummer, David Schurig, John B. Pendry, and David R. Smith. Optical design of reflectionless complex media by finite embedded coordinate transformations. *Physical Review Letters*, 100(6), 2008.

[16] M Rahm, D a Roberts, J B Pendry, and D R Smith. Transformation-optical design of adaptive beam bends and beam expanders. *Optics express*, 16(15):11555–11567, 2008.

[17] Romain Fleury and Andrea Alu. Enhanced superradiance in epsilon-near-zero plasmonic channels. *Physical Review B*, 87(20), 2013.

[18] Ahmed M Mahmoud and Nader Engheta. Wave-matter interactions in epsilon-and-mu-near-zero structures. *Nature Communications*, 5:5638, 2014.

[19] Yun Lai, Jack Ng, Huanyang Chen, Dezhuan Han, Junjun Xiao, Zhao Qing Zhang, and C. T. Chan. Illusion optics: The optical transformation of an object into another object. *Physical Review Letters*, 102(25), 2009.

[20] G. D'Aguanno, M. Centini, M. Scalora, C. Sibilia, M. Bertolotti, M. J. Bloemer, C. M. Bowden, and J. W. Haus. Group velocity, energy velocity, and superluminal propagation in finite photonic band gap structures. In *Technical Digest - Summaries of Papers Presented at the Quantum Electronics and Laser Science Conference, QELS 2001*, page 124, 2001.

[21] D R Solli, C F Mccormick, R Y Chiao, and J M Hickmann. Experimental Observation of Superluminal Group Velocities in Bulk Two-Dimensional Photonic Bandgap Crystals. *IEEE Journal on Selected Topics in Quantum Electronics*, 9(1):40–42, 2003.

[22] L.D. Landau, L.P. Pitaevskii, and E.M. Lifshitz. *Electrodynamics of Continuous Media, 2nd Ed.*, volume 29. 1984.

[23] Mário Silveirinha and N Engheta. Tunneling of electromagnetic energy through subwavelength channels and bends using ϵ-near-zero materials. *Physical Review Letters*, 97:157403, 2006.

[24] Mário G. Silveirinha and Nader Engheta. Theory of supercoupling, squeezing wave energy, and field confinement in narrow channels and tight bends using ϵ near-zero metamaterials. *Physical Review B - Condensed Matter and Materials Physics*, 76(24):1–17, 2007.

[25] G Dolling, C Enkrich, M Wegener, J F Zhou, C M Soukoulis, and S Linden. Cut-wire pairs and plate pairs as magnetic atoms for optical metamaterials. *Optics letters*, 30(23):3198–3200, 2005.

[26] C. Enkrich, M. Wegener, S. Linden, S. Burger, L. Zschiedrich, F. Schmidt, J. F. Zhou, Th Koschny, and C. M. Soukoulis. Magnetic metamaterials at telecommunication and visible frequencies. *Physical Review Letters*, 95(20):5–8, 2005.

[27] Qian Zhao, Ji Zhou, Fuli Zhang, and Didier Lippens. Mie resonance-based dielectric metamaterials. *Materials Today*, 12(12):60–69, dec 2009.

[28] Saman Jahani and Zubin Jacob. All-dielectric metamaterials. *Nature Nanotechnology*, 11(1):23–36, 2016.

[29] Costas M Soukoulis and Martin Wegener. Past achievements and future challenges in the development of three-dimensional photonic metamaterials. *Nature Photonics*, 5(SEPTEMBER):1–8, 2011.

[30] John David Jackson. *Classical Electrodynamics*. Wiley, New York, 3rd edition, 1999.

[31] J. C. M. Garnett. Colours in Metal Glasses, in Metallic Films, and in Metallic Solutions. II. *Philosophical Transactions of the Royal Society A: Mathematical, Physical and Engineering Sciences*, 205(387-401):237–288, 1906.

[32] DAG Bruggeman. Calculation of various physics constants in heterogenous substances I Dielectricity constants and conductivity of mixed bodies from isotropic substances. *Annalen der Physik*, 24(7):636–664, 1935.

[33] Ying Wu, Jensen Li, Zhao Qing Zhang, and C. T. Chan. Effective medium theory for magnetodielectric composites: Beyond the long-wavelength limit. *Physical Review B - Condensed Matter and Materials Physics*, 74(8):1–9, 2006.

[34] D. R. Smith, D. C. Vier, Th Koschny, and C. M. Soukoulis. Electromagnetic parameter retrieval from inhomogeneous metamaterials. *Physical Review E - Statistical, Nonlinear, and Soft Matter Physics*, 71(3):1–11, 2005.

[35] Milka Jakovljevic, Borislav Vasic, Goran Isic, Rados Gajic, Tom Oates, Karsten Hinrichs, Iris Bergmair, and Kurt Hingerl. Oblique incidence reflectometry and spectroscopic ellipsometry of split-ring resonators in infrared. *Journal of Nanophotonics*, 5(1):051815, 2011.

[36] J. B. Pendry. Negative refraction makes a perfect lens. *Physical Review Letters*, 85(18):3966–3969, 2000.

[37] Constantin R. Simovski and Sergei A. Tretyakov. Local constitutive parameters of metamaterials from an effective-medium perspective. *Physical Review B - Condensed Matter and Materials Physics*, 75(19):1–10, 2007.

[38] C R Simovski. On electromagnetic characterization and homogenization of nanostructured metamaterials. *Journal of Optics*, 13:013001, 2010.

[39] Hideo Kosaka, Takayuki Kawashima, Akihisa Tomita, Masaya Notomi, Toshiaki Tamamura, Takashi Sato, and Shojiro Kawakami. Superprism phenomena in photonic crystals. *Physical Review B*, 58(16):R10096–R10099, 1998.

[40] Salvatore Savo, B. D F Casse, Wentao Lu, and Srinivas Sridhar. Observation of slow-light in a metamaterials waveguide at microwave frequencies. *Applied Physics Letters*, 98(17), 2011.

[41] Albert Polman and Harry a. Atwater. Photonic design principles for ultrahigh-efficiency photovoltaics. *Nature Materials*, 11:174–177, 2012.

[42] Vijay Kris Narasimhan and Yi Cui. Nanostructures for photon management in solar cells. *Nanophotonics*, 2:187–210, 2013.

[43] Chen Sun, Mark T. Wade, Yunsup Lee, Jason S. Orcutt, Luca Alloatti, Michael S. Georgas, Andrew S. Waterman, Jeffrey M. Shainline, Rimas R. Avizienis, Sen Lin, Benjamin R. Moss, Rajesh Kumar, Fabio Pavanello, Amir H. Atabaki, Henry M. Cook, Albert J. Ou, Jonathan C. Leu, Yu-Hsin Chen, Krste Asanović, Rajeev J. Ram, Miloš A. Popović, and Vladimir M. Stojanović. Single-chip microprocessor that communicates directly using light. *Nature*, 528(7583):534–538, 2015.

[44] Nader Engheta. Pursuing Near-Zero Response. *Science*, 340:286, 2013.

[45] Jiaming Hao, Wei Yan, and Min Qiu. Super-reflection and cloaking based on zero index metamaterial. *Applied Physics Letters*, 96:101109, 2010.

[46] Viet Cuong Nguyen, Lang Chen, and Klaus Halterman. Total Transmission and Total Reflection by Zero Index Metamaterials with Defects. *Physical Review Letters*, 105(23):233908, dec 2010.

[47] Alec Rose and David R. Smith. Overcoming phase mismatch in nonlinear metamaterials [Invited]. *Optical Materials Express*, 1(7):1232, 2011.

[48] Haim Suchowski, Kevin O'Brien, Zi Jing Wong, Alessandro Salandrino, Xiaobo Yin, and Xiang Zhang. Phase mismatch-free nonlinear propagation in optical zero-index materials. *Science*, 342(6163):1223–1226, 2013.

[49] Ahmed M Mahmoud and Nader Engheta. Wave-matter interactions in epsilon-and-mu-near-zero structures. *Nature Communications*, 5:5638, 2014.

[50] Alan Snyder and John Love. *Optical Waveguide Theory*. Chapman and Hall, New York, 2nd edition, 1983.

[51] Jd John D Joannopoulos, Steven Johnson, Joshua N Jn Winn, and Rd Robert D Meade. *Photonic crystals: molding the flow of light*. Princeton University Press, Princeton NJ, 2nd edition, 2008.

[52] Ying Zhang, Jürgen Von Hagen, Marwan Younis, Christian Fischer, and Werner Wiesbeck. Planar Artificial Magnetic Conductors and Patch Antennas. *IEEE Transactions on Antennas and Propagation*, 51(10):2704–2712, 2003.

[53] Ranjith Rajasekharan and Ann Roberts. Optical 'magnetic mirror' metasurfaces using interference between Fabry-Pérot cavity resonances in coaxial apertures. *Scientific reports*, 5(April):10297, 2015.

[54] You Zhou, Xin-Tao He, Fu-Li Zhao, and Jian-Wen Dong. Proposal for achieving in-plane magnetic mirrors by silicon photonic crystals. *Optics Letters*, 41(10), 2016.

[55] Rong Sun, Mark Beals, Andrew Pomerene, Jing Cheng, Ching-Yin Hong, Lionel Kimerling, and Jurgen Michel. Impedance matching vertical optical waveguide couplers for dense high index contrast circuits. *Optics express*, 16(16):11682–11690, 2008.

[56] Steven G. Johnson, Peter Bienstman, M. A. Skorobogatiy, Mihai Ibanescu, Elefterios Lidorikis, and J. D. Joannopoulos. Adiabatic theorem and continuous coupled-mode theory for efficient taper transitions in photonic crystals. *Physical Review E - Statistical, Nonlinear, and Soft Matter Physics*, 66(6):1–15, 2002.

[57] M Claudia Troparevsky, Adrian S Sabau, Andrew R Lupini, and Zhenyu Zhang. Transfer-matrix formalism for the calculation of optical response in multilayer systems: from coherent to incoherent interference. *Optics express*, 18(24):24715–24721, 2010.

[58] L. V. Iogansen. Resonant tunneling of light in optical waveguides. *Journal of the Optical Society of America*, 66(9):972, sep 1976.

[59] Brian Edwards, Andrea Alù, Mário G Silveirinha, and Nader Engheta. Comparison beween Epsilon-Near-Zero and Fabry-Perot Resonant Transmission through Waveguide Bends and Chanels. *XIXX General Assembly of the International Union of Radio Science (URSI-GA 2008)*, pages 2–4, 2008.

[60] J B Pendry, D Schurig, and D R Smith. Controlling electromagnetic fields. *Science*, 312(5781):1780–2, jun 2006.

[61] Song-liang Chua, Ling Lu, Jorge Bravo-abad, John D Joannopoulos, and Marin Soljacic. Larger-area single-mode photonic crystal surface-emitting lasers enabled by an accidental Dirac point. *Optics Letters*, 39(7):2072–2075, 2014.

[62] Haim Suchowski, Kevin O'Brien, Zi Jing Wong, Alessandro Salandrino, Xiaobo Yin, and Xiang Zhang. Phase Mismatch-Free Nonlinear Propagation in Optical Zero-Index Materials. *Science (New York, N.Y.)*, 342(December):1223–1226, 2013.

[63] Nader Engheta and Richard W. Ziolkowski. *Metamaterials: Physics and Engineering Explorations*. Wiley, New York, 2006.

[64] JB Pendry, JB Pendry, AJ Holden, AJ Holden, WJ Stewart, WJ Stewart, I. Youngs, and I. Youngs. Extremely low frequency plasmons in metallic mesostructures. *Physical Review Letters*, 76(25):4773–4776, 1996.

[65] Alexandra Boltasseva and Harry a Atwater. Low-Loss Plasmonic Metamaterials. *Science*, 331(6015):290–291, 2011.

[66] Ruben Maas, James Parsons, Nader Engheta, and Albert Polman. Experimental realization of an epsilon-near-zero metamaterial at visible wavelengths. *Nature Photonics*, 7(11):907–912, 2013.

[67] J. B. Pendry, A. J. Holden, D. J. Robbins, and W. J. Stewart. Magnetism from conductors and enhanced nonlinear phenomena. *IEEE Transactions on Microwave Theory and Techniques*, 47(11):2075–2084, 1999.

[68] Ruopeng Liu, Qiang Cheng, Thomas Hand, Jack J. Mock, Tie Jun Cui, Steven A. Cummer, and David R. Smith. Experimental demonstration of electromagnetic tunneling through an epsilon-near-zero metamaterial at microwave frequencies. *Physical Review Letters*, 100(2), 2008.

[69] Xueqin Huang, Yun Lai, Zhi Hong Hang, Huihuo Zheng, and C T Chan. Dirac cones induced by accidental degeneracy in photonic crystals and zero-refractive-index materials. *Nature Materials*, 10:582–586, 2011.

[70] Parikshit Moitra, Yuanmu Yang, Zachary Anderson, Ivan I. Kravchenko, Dayrl P. Briggs, and Jason Valentine. Realization of an all-dielectric zero-index optical metamaterial. *Nature Photonics*, 7(10):1–5, 2013.

[71] Isabelle Staude, Andrey E. Miroshnichenko, Manuel Decker, Nche T. Fofang, Sheng Liu, Edward Gonzales, Jason Dominguez, Ting Shan Luk, Dragomir N. Neshev, Igal Brener, and Yuri Kivshar. Tailoring directional scattering through magnetic and electric resonances in subwavelength silicon nanodisks. *ACS Nano*, 7(9):7824–7832, 2013.

[72] Andrey B Evlyukhin, René L Eriksen, Wei Cheng, Jonas Beermann, Carsten Reinhardt, Alexander Petrov, Stefan Prorok, Manfred Eich, Boris N Chichkov, and Sergey I Bozhevolnyi. Optical spectroscopy of single Si nanocylinders with magnetic and electric resonances. *Scientific Reports*, 4:4126, 2014.

[73] C. A. Balanis. *Engineering Electromagnetics*. Wiley, New York, 1989.

[74] Ying Wu, Jensen Li, Zhao-Qing Zhang, and C. Chan. Effective medium theory for magnetodielectric composites: Beyond the long-wavelength limit. *Physical Review B*, 74(8):085111, aug 2006.

[75] Chia Wei Hsu, Bo Zhen, Song-Liang Chua, Steven G Johnson, John D Joannopoulos, and Marin Soljačić. Bloch surface eigenstates within the radiation continuum. *Light: Science & Applications*, 2(7):e84, 2013.

[76] Amir Hosseini, Xiaochuan Xu, David N. Kwong, Harish Subbaraman, Wei Jiang, and Ray T. Chen. On the role of evanescent modes and group index tapering in slow light photonic crystal waveguide coupling efficiency. *Applied Physics Letters*, 98(3):3–5, 2011.

[77] Shota Kita, Yang Li, Philip Muñoz, Orad Reshef, Daryl I. Vulis, Robert W. Day, Eric Mazur, and Marko Lončar. On-chip all-dielectric fabrication-tolerant zero-index metamaterials. aug 2016.

[78] D. C. Marinica, A. G. Borisov, and S. V. Shabanov. Bound states in the continuum in photonics. *Physical Review Letters*, 100(18), 2008.

[79] Chia Wei Hsu, Bo Zhen, A Douglas Stone, John D Joannopoulos, and Marin Soljačić. Bound states in the continuum. *Nature Reviews Materials*, 1:16048, jul 2016.

[80] Attila Mekis, Shanhui Fan, and J. Joannopoulos. Bound states in photonic crystal waveguides and waveguide bends. *Physical Review B*, 58(8):4809–4817, 1998.

[81] Authors Yang Li, Shota Kita, Philip Muñoz, Orad Reshef, Daryl I Vulis, and Mei Yin. On-chip zero-index metamaterials. *Nature Photonics*, 9(October):1–6, oct 2015.

[82] Cale M. Gentry and Miloš a. Popović. Dark state lasers. *Optics Letters*, 39(14):4136, 2014.

[83] Aditya Jain, Parikshit Moitra, Thomas Koschny, Jason Valentine, and Costas M. Soukoulis. Electric and Magnetic Response in Dielectric Dark States for Low Loss Subwavelength Optical Meta Atoms. *Advanced Optical Materials*, 3:1431–1438, 2015.

[84] Yi Yang, Chao Peng, Yong Liang, Zhengbin Li, and Susumu Noda. Analytical perspective for bound states in the continuum in photonic crystal slabs. *Physical Review Letters*, 113(3):1–5, 2014.

[85] John von Neumann and Eugene Wigner. Über merkwürdige diskrete Eigenwerte. *Physik Z*, 30:465–467, 1929.

[86] Yonatan Plotnik, Or Peleg, Felix Dreisow, Matthias Heinrich, Stefan Nolte, Alexander Szameit, and Mordechai Segev. Experimental observation of optical bound states in the continuum. *Physical Review Letters*, 107(18):28–31, 2011.

[87] Thomas Lepetit and Boubacar Kante. Controlling multipolar radiation with symmetries for electromagnetic bound states in the continuum. *Physical Review B - Condensed Matter and Materials Physics*, 90(24):1–4, 2014.

[88] Chia Wei Hsu, Bo Zhen, Song-Liang Chua, Steven G Johnson, John D Joannopoulos, and Marin Soljačić. Bloch surface eigenstates within the radiation continuum. *Light: Science & Applications*, 2(7):e84, 2013.

[89] Chia Wei Hsu, Bo Zhen, Jeongwon Lee, Song-liang Chua, Steven G Johnson, John D Joannopoulos, and Marin Soljačić. Observation of trapped light within the radiation continuum. *Nature*, 499(7457):188–91, 2013.

[90] Jeongwon Lee, Bo Zhen, Song Liang Chua, Wenjun Qiu, John D Joannopoulos, Marin Soljačić, and Ofer Shapira. Observation and differentiation of unique high-Q optical resonances near zero wave vector in macroscopic photonic crystal slabs. *Physical Review Letters*, 109(6):1–5, 2012.

[91] Eugene Hecht. *Optics*. Addison Wesley, Reading, MA, 2001.

[92] Shotaro Nagai and Atsushi Sanada. Gamma-point group velocity of lossy Dirac cone composite right / left- handed metamaterials. *IEICE Electronics Express*, 13(10):1–6, 2016.

[93] Bo Zhen, Chia Wei Hsu, Ling Lu, A. Douglas Stone, and Marin Soljačić. Topological nature of optical bound states in the continuum. *Physical Review Letters*, 113(25), 2014.

[94] Kazuaki Sakoda. Proof of the universality of mode symmetries in creating photonic Dirac cones. *Optics Express*, 20(22):25181, 2012.

[95] J S Douglas, H Habibian, C.-L. Hung, A V Gorshkov, H J Kimble, and D E Chang. Quantum many-body models with cold atoms coupled to photonic crystals. *Nature Photonics*, 9(5):326–331, 2015.

[96] Wonjoo Suh, M. F. Yanik, Olav Solgaard, and Shanhui Fan. Displacement-sensitive photonic crystal structures based on guided resonance in photonic crystal slabs. *Applied Physics Letters*, 82(13):1999–2001, 2003.

[97] Vladislav Yakovlev and Gabriel Tempea. Optimization of chirped mirrors. *Applied optics*, 41(30):6514–6520, 2002.

[98] Omid Nohadani, Jonathan R Birge, Franz X Kärtner, and Dimitris J Bertsimas. Robust chirped mirrors. *Applied optics*, 47(14):2630–2636, 2008.

[99] Huanyang Chen, C T Chan, and Ping Sheng. Transformation optics and metamaterials, 2010.

[100] Mark I Stockman. Does Nature Allow Negative Refraction with Low Losses in Optical Region? *ARXIV*, 2:4, 2006.

[101] Evaluation of measurement data - Guide to the expression of uncertainty in measurement. *International Organization for Standardization Geneva ISBN*, 50(September):134, 2008.

[102] Shanhui Fan and J. Joannopoulos. Analysis of guided resonances in photonic crystal slabs. *Physical Review B*, 65(23):1–8, 2002.

[103] Shanhui Fan, Wonjoo Suh, and J D Joannopoulos. Temporal coupled-mode theory for the Fano resonance in optical resonators. *Journal of the Optical Society of America. A, Optics, image science, and vision*, 20(3):569–572, 2003.